© Copyright 2020

Shane Colburn

# Design of computational imaging systems using wavefront-coded dielectric metasurfaces

Shane Colburn

A dissertation

submitted in partial fulfillment of the

requirements for the degree of

Doctor of Philosophy

University of Washington

2020

Reading Committee:

Arka Majumdar, Chair

Lih Lin

Karl Böhringer

Program Authorized to Offer Degree:

Electrical and Computer Engineering

University of Washington

## Abstract

Design of computational imaging systems using wavefront-coded dielectric metasurfaces

Shane Colburn

Chair of the Supervisory Committee:
Professor Arka Majumdar
Electrical and Computer Engineering

High-quality cameras are widely accessible today owing to the ubiquity of smartphones and the miniaturization of sensors driven by improvements in manufacturing. These cameras, however, still rely on assemblies of aberration-correcting, refractive elements that are fundamentally the same technology in use for optical systems for centuries. While for smartphones these assemblies can be made sufficiently small, these lenses present a bulky form factor for the most stringent size and weight-constrained applications. One candidate for enabling further miniaturization is metasurfaces, which are ultrathin surfaces comprising arrays of subwavelength-spaced, spatially varying scatterers. By locally tailoring the response of each scatterer, metasurfaces can manipulate the phase, amplitude, and polarization of wavefronts at subwavelength resolution with only a wavelength-scale thickness. While promising for next-generation miniaturized optics, in an

imaging context, metasurfaces exhibit significant aberrations. Most metasurface research has also focused on producing static elements, which pose a challenge for systems that require varifocal control. While there has been significant work towards circumventing these challenges through innovations in scatterer design, such approaches often entail tradeoffs in terms of system complexity, polarization dependence, efficiency, and limitations on scaling to large area apertures. In this dissertation, we instead examine the utility of computational imaging in conjunction with metasurfaces so that we can simultaneously enhance performance while maintaining the size benefits offered by metasurfaces. In a computational imaging system, software is treated as a component in the image formation process. Here, we examine this approach by exploring several different imaging modalities supported by metasurfaces combined with computation so that we can simultaneously deliver a compact form factor and high-quality images. These modalities include imaging in full color, varifocal zoom capability, and acquiring depth information from a scene. Through a combination of wavefront coding, deconvolution, and Alvarez lens-inspired conjugate metasurfaces, we demonstrate a set of separate metasurface systems that image over the full visible spectrum, can achieve more than 200% change in focal length with a 1 cm aperture, and can discriminate depths with fractional ranging error of 1.7%. The demonstrated approach may find applications in microscopy, planar cameras, machine vision, and augmented reality.

# TABLE OF CONTENTS

# LIST OF FIGURES

# LIST OF TABLES

# ACKNOWLEDGEMENTS

A lot has happened in the past few years during my time in graduate school at the University of Washington and there have been a range of challenges along the way, both school-related and personal. I want to thank all who have been of help to me during these past few years and as well as those that have been supportive of me throughout my entire education.

During my PhD, I received significant help and training from the phenomenal staff at the Washington Nanofabrication Facility. In addition to numerous users and staff that were extremely patient and answered my many basic questions while working in the cleanroom, I'd like to specifically thank several staff members for their assistance. Duane Irish worked with me on the stepper during my fabrication of large area metasurfaces and with all other photolithography-related questions. Darick Baker was an enormous help with all thin film and general questions about the cleanroom, especially with helping me develop a process for sputtering films of Germanium Antimony Telluride (GST) phase-change material for tunable metasurface applications. Shane Patrick was super knowledgeable and helpful with training and advice on electron-beam lithography. Mark Morgan helped with process development for the silicon nitride etch that we use for our metasurfaces.

My colleagues in lab also played a big role in my research and learning during graduate school. Taylor Fryett was always a reliable source of knowledge for almost any experimental and fabrication questions and helped point me in the right direction while I was developing a process for thick SU8 films for multilayer metasurfaces. Jiajiu Zheng was a good officemate and helped develop a GST COMSOL model when we were studying the coupling between tunable metasurface scatterers. I want to thank Zhuoran Fang for taking over on part of where I left off on the GST project. James Whitehead and Luocheng Huang did a great job taking over on some of

the metasurface imaging projects. Elyas Bayati was a great colleague to bounce ideas off of and always provided enthusiasm and a good perspective on how to make one's research impactful. Albert Ryou, our postdoc, was another great officemate who was fun to talk with about both science and non-science topics. Albert's broad base of knowledge in physics and optics was helpful on multiple projects, especially on design-related tasks for cavity simulation, modeling diffraction, and neural networks. Yueyang Chen also was a great person to talk with and helped give another perspective on my work. I'd also like to thank Shreyas Shah and Chang-Hua Liu, both postdocs for part of my time in Arka's group, for their insights and feedback on my research. Lastly and most significantly of my lab colleagues, Alan Zhan was a great mentor who I cannot thank enough for all his help teaching me basic experimental optics, introducing me to the simulation tools we use, and bringing me up to speed on fabrication processes when I started out. Alan was also super helpful throughout my PhD as a person to discuss research with and to get constructive feedback from on manuscripts and presentations.

I also want to thank all the professors that have provided mentorship, served on committees, and provided insights on my work or career advice, including Lih Lin, Karl Böhringer, Kai-Mei Fu, Scott Dunham, Matt Reynolds, Brian Curless, Felix Heide, and James Peckol.

I want to especially thank my adviser, Arka Majumdar. Arka has been a great adviser. One of the great things about having him as an adviser is how hands-on and involved he is with projects. He's always been available for help and doesn't shy away from the nitty gritty details when you're stuck on something. At the same time, however, he's been able to leave me to my own devices and figure things out independently when I want or it's necessary for my learning, which has been crucial to my growth and skills acquisition in graduate school. I also really appreciate his willingness and encouragement for me to intern during my PhD, not just once, but on three

different occasions. This openness to letting me do multiple internships is rare among PhD advisers. Arka's passion and stream of new ideas fostered a great environment for trying new things and expanding in different research directions. I have greatly appreciated his mentorship during my PhD and am very thankful I chose to join his lab.

Graduate school would not have been nearly as enjoyable if I didn't have an outlet outside of school. For that, I thank my friends for our cabin trips and camping, brewery hangouts, making beer, games of poker, cooking, hiking, bouldering, skydiving, and all the other fun and often random things we did. I also want to thank Conner Ballew specifically for all the fun times and chats when we were still master's students struggling with the load of too many classes, long TA hours, and research simultaneously, especially during that first quarter of graduate school.

I especially want to thank my family for their unconditional support and encouragement throughout my education. My mom has always been supportive of no matter what path I have taken, and my dad has always loved to hear about my work. My grandparents have always encouraged and inspired me to do more. I particularly want to thank my brother, Zach, for his determination and focus that always pushed me to do more and challenge myself. This has been the case not just in graduate school but throughout my life. I want to give an enormous thanks to my fiancé, Linda, for her love and support throughout the past few years of doing long distance with her in medical school and me in graduate school. Whenever I was vexed by something, stressed, or perplexed by decisions to make, she was a great listener and always gave good advice. And of course, Max, Lexi, Ollie, and Colby were the best of friends from my time as an undergraduate at UW through my PhD.

# DEDICATION

To my friends and family

# Chapter 1. INTRODUCTION

## 1.1 MOTIVATION

Cameras and imaging systems today are ubiquitous. Over the last few decades, these systems have decreased in size significantly because of the downscaling of CMOS sensors via Moore's law. Currently, however, most imaging systems are no longer size-limited by their sensors but rather by the optical elements themselves. To achieve high-quality images, it is often necessary to utilize a complex assembly of refractive elements that work together to mitigate aberrations and achieve an aesthetically pleasing image. The necessity of using these elements incurs heavy costs and limits size reduction, limiting their utility in size and weight-constrained applications such as planar cameras, implantable microscopy, miniaturized machine vision sensors for the Internet of Things (IoT), and mixed reality systems.

To meet the growing demand for miniaturized optics for next-generation sensors, replacing these systems with simpler and more compact optical elements is an active area of research being explored through several different perspectives. In the computational imaging community, for example, rather than only relying on the optics to produce an image, post-processing software plays an integral role in the image formation process [1–3]. This paradigm enables a significant portion of the aberration-correction to be shifted to the software realm, facilitating the replacement of bulky optical assemblies with fewer and simpler lenses or other components [4]. Often, however, many of the optical computational imaging systems still use relatively large elements that would be unsuitable for the most size-constrained imaging tasks. Taken to the extreme, there are implementations without any optics, namely lensless imagers [5] that reconstruct a scene based on diffraction kernels and priors based on the scene. While such lensless imaging systems have

garnered significant interest and can demonstrate reasonable image quality, they require significant computation that can incur substantial latency and power consumption in the image formation process.

As such, a more optimal approach for a system requiring miniaturization might be one that strikes a balance between software and hardware, more equally splitting the burden of image formation between the two. In the nanophotonics community, metasurface optics present a unique platform for achieving this. Metasurfaces are ultrathin arrays of subwavelength-spaced optical scatterers patterned into the surface of a material that can abruptly modify properties of incident optical wavefronts [6–9]. By adjusting the geometry or orientation of scatterers in a spatially varying manner across a substrate, metasurfaces can modify the phase, amplitude, and polarization of lightfields in a compact form factor. Recently, these devices have enabled ultrathin and flat implementations of a variety of optical elements, including lenses [10–16], vortex beam generators [11,17–21], holographic plates [22,23], and freeform surfaces [24–26]. With their capability for implementing compact optical components, metasurfaces offer a compelling methodology for downscaling optical hardware for next-generation sensors.

While metasurfaces have garnered significant interest in recent years, there has been little work examining their use in conjunction with computational imaging. Furthermore, metasurfaces must contend with a strong wavelength sensitivity that induces severe chromatic aberrations in images compared to existing refractive lenses commonly used in modern imaging systems. While there are existing approaches to mitigating these aberrations, which will be discussed in the succeeding sections, they are limited in scope. Furthermore, while many modern cameras are capable of high-quality optical zoom, requiring a tunable focal length lens, the subwavelength nature of metasurface scatterers and their wavelength sensitivity make this a very challenging task

for metasurface systems. As such, while metasurfaces offer a competitive platform for miniaturizing optical systems in conjunction with computational imaging, any metasurface-based imaging modality must contend with a host of constraints that currently would limit its scope and the resultant image quality.

In this thesis, we will detail our research addressing these challenges, including background information and literature context, our work building and testing metasurface-based computational imaging systems, and the future directions we will pursue to help realize a more effective metasurface imaging platform.

## 1.2 Computational Imaging

Conventional imaging systems consist of a lens that forms an image of a scene and a camera sensor that converts the incident light projected by the lens into electrical signals. In this paradigm, while the sensor can affect the resultant image quality, potentially dictating the resolution and adding noise, the lens is the component that forms the image itself. Often, the captured image is filtered or modified using image processing algorithms, but these techniques are applied independently of the optics used to capture the image. In computational imaging, however, the software applied after data is captured by the sensor plays an integral in the image formation process as the optics and software depend on one another [1]. While adding software to the imaging pipeline incurs added power consumption and latency relative to the passive image formation offered by optics, in some cases, a computational imaging approach can reduce the complexity of the required optical elements. Recent works have demonstrated high-quality images by combing simple lenses with post-processing algorithms to correct aberrations without requiring additional bulky elements in the optical path [4].

Computational imaging can also potentially enhance system performance. One prominent example of this is in wavefront coding [27,28]. By inserting an additional phase mask in an optical imaging path, information can be encoded onto the wavefront, potentially enabling a more efficient transfer of spatial frequency content or other desirable scene information that can then be decoded in software, information which might otherwise be lost by directly capturing the image with a traditional system. In wavefront coding systems, the point spread function (PSF) of the optical system is typically engineered to behave differently from a standard clear aperture lens. A PSF is just an optical system's response to a point source of light, the image it produces of a point, and for linear, shift-invariant systems, it fully characterizes the behavior of the system, capturing the essence of any aberrations or blurring arising from diffraction.

One prominent example of wavefront coding systems is the use of cubic phase masks [27]. A cubic phase mask is an optical element whose phase is characterized by a cubic polynomial as a function of position (x, y). When such an element is inserted into the path of a lens, it has the effect of extending the depth of focus, such that rather than focusing to a point, the lens focuses to an elongated line. This has the effect of extending the depth of field of the system by making images insensitive to the object being defocused over a wide depth range. Images captured with this system, however, are blurry because the PSF no longer resembles a tightly focused spot like that of a regular lens. If the system's PSF is measured prior, however, a simple deconvolution operation can recover the focused image but with a much wider range of depths in focus as compared to a standard lens without a cubic element [28]. Such systems are also less susceptible to chromatic aberrations as a change in wavelength often changes the focal length of a system [29]. When chromatic aberrations cause defocus in a cubic-modulated system, however, the insensitivity to misfocus limits the reduction in image quality.

At the opposite extreme of cubic phase masks, which enable all depths to be treated the same, there are wavefront coding elements that enable very precise depth discrimination, such as double-helix PSF surfaces that produce PSFs that rotate as the point source is brought in and out of focus [30–33]. In conjunction with deconvolution software, these elements have enabled calculation of the depth at which an object is located. In our research, we exploit wavefront coding and metasurface versions of both cubic phase masks and double-helix PSFs to realize computational imaging systems.

## 1.3 METASURFACES

### 1.3.1 *Overview*

Metasurfaces are diffractive elements that consist of quasiperiodic arrays of subwavelength-spaced optical scatters that can modify the phase, amplitude, and polarization of incident electromagnetic radiation [6–8]. Unlike multi-level diffractive optics that achieve phase shifts via gradual phase accumulation by propagation through the material [6], metasurfaces have scatterers that are of the same thickness throughout the device. Instead, by changing either the geometry or orientation of a scatterer, the amplitude and phase of the transmission or reflection coefficient of incident light can be tuned. By adjusting scatterer geometries in a spatially-varying manner across a substrate, spatial transfer functions can be implemented in a compact form factor, enabling flat implementations of lenses [10–16], vortex beam generators [11,17–21], holographic plates [22,23], and freeform surfaces [24–26]. Additionally, owing to the subwavelength spacing of the scatterers in a metasurface, these devices only transmit light into the zeroth diffraction order, unlike conventional diffractive elements that generate and lose light to multiple orders. Furthermore, due to the uniform thickness of the scatterers, metasurfaces can be fabricated with only a single lithography stage.

While many of the initial metasurface works utilized plasmonic effects based on metallic scatterers [6,8,16,34–38], the high absorption losses of the metals limited the efficiencies of these devices and constrained them primarily to reflection mode. Due to these losses, dielectric metasurfaces have become more common as the transparency of these materials enables more efficient transformations of incident light and are more amenable to transmissive optics [13–15,18,24,25,39–51]. Silicon nitride is a material well suited to metasurface design, due to its CMOS-compatibility enabling accommodation for mass manufacturing, and its lossless nature from the near-ultraviolet into the infrared, enabling high-efficiency optical elements [52]. For these reasons, in our research we use silicon nitride to make our metasurfaces as we are working at visible wavelengths.

### 1.3.2 *Operation*

There are various scatterer designs that can be used to induce phase shifts for metasurfaces, but in our research we use a nanopost structure, which is a cylinder of silicon nitride positioned on top of a substrate [49]. This structure is primarily selected due to its polarization insensitivity, enabling operation with arbitrary polarization states of incident light. These nanoposts can be understood as operating as truncated waveguides that support several oscillating modes that couple amongst themselves at the top and bottom interfaces of the posts [53–55]. Incident light couples into these modes and then the modes couple back into free space with a net change in phase and amplitude that constitute the transmission or reflection coefficient. The imparted phase and amplitude depend on the incident wavelength and for a given metasurface structure, deviating from the design value typically causes strong chromatic aberrations, which in the case of lenses result in color blur and ringing in subsequent images formed using metasurface lenses.

To design metasurfaces, the procedure begins with identification of a phase profile to be imparted. Then, for a given operating wavelength, cylindrical nanoposts are designed such that in varying their diameter over a fixed range, phase shifts in the 0 to $2\pi$ range are achievable with near-unity amplitude. These nanoposts are typically simulated using rigorous coupled-wave analysis [56], a simulation technique capable of calculating transmission or reflection coefficient of periodic layered structures. Once a nanopost design is determined, the simulated transmission coefficient is used as a lookup table, mapping phases to diameters, and for each pixel in the desired phase profile, the phase is mapped to the diameter corresponding to desired phase value. In this manner, a 2-D distribution of diameters is determined that can then be simulated via finite-difference time-domain simulation, or via wave optics simulators when treating each pixel as a complex amplitude.

## 1.4 Thesis Outline

To address the limitations of existing metasurface-based imaging systems and develop a platform to potentially address the scaling demands for next-generation miniaturized image sensors, we propose to explore several pertinent imaging modalities using metasurfaces in conjunction with computation. This dissertation will detail our work in this direction through a series of projects that extend the imaging capabilities of existing metasurface platforms. Chapter 2 will first provide background information on metasurfaces to aid understanding of the subsequent sections. Chapter 3 will then detail our work building a full-color imaging system by combining an extended depth of focus metalens with deconvolution software. Chapter 4 discusses a metasurface design for enabling varifocal zoom imaging and Chapter 5 expands on this design by modifying the phase profile design and combining it with deconvolution to provide simultaneous achromatic and varifocal behavior. Chapter 6 then details our work using a system of two metasurfaces in

conjunction with post-capture software for simultaneously reconstructing scenes as well as acquiring depth information with only a single camera snapshot. Finally, Chapter 7 provides concluding remarks on the work discussed in this dissertation.

# Chapter 2. METASURFACES BACKGROUND

## 2.1 DIFFRACTIVE OPTICS

### 2.1.1 *Modeling Diffraction*

Metasurfaces are diffractive optical elements that typically require a combination of different modeling techniques for their design and analysis. Central to many of the modelling techniques, however, is treating the light propagation as a diffractive phenomenon. As metasurfaces are essentially subwavelength diffractive optical elements, in this section we give a brief overview of some of the standard techniques used for performing diffraction calculations that are subsequently applied when we design and simulate metasurfaces.

Various techniques exist for modelling light propagation, the selection of which depends on the scale of the system and the approximations that can be made. At one extreme, Maxwell's equations can be solved directly using a method based on finite differences (e.g., finite-difference time-domain or finite-difference frequency-domain), in which the full vector nature of the electric and magnetic fields and their interplay are considered. Such an approach, however, is impractical for most optical systems as it requires fine discretization in space as well as time or frequency, depending on which technique, necessitating significant computational resources and often prohibitively long simulation times. At the other extreme, light is modelled via geometrical optics by tracing rays through a sequence of surfaces. These rays account for the direction and position of a planar wavefront. In a homogenous medium, a ray maintains its direction and is only deflected at an interface between two materials, the angle of which is dictated by Snell's law. While geometrical optics is incredibly powerful and is the design basis for most existing optical systems (e.g., lens assemblies in cameras, microscopes, telescopes, etc.), it provides an incomplete picture

of how light propagates through a system, which breaks down when one must consider diffraction effects arising from small apertures.

Fourier optics strikes a balance between these two regimes, enabling simulations with significantly less memory and computation time than finite-difference simulations but which account for diffraction effects neglected in geometrical optics. Underpinning much of Fourier optics is the assumption of scalar diffraction, an approximation that asserts that the vector components of an electromagnetic field can be treated independently of one another, which holds true in homogenous, isotropic, source-free media. A standard formulation of diffraction in a system is given by the Rayleigh-Sommerfeld [57], which is equivalent to the angular spectrum formulation [57], making no assumptions about the light to be modelled except that it is a scalar. For an electric field distribution in a plane, the angular spectrum relates the electric field in another, parallel plane by a convolution operation (i.e., multiplication in the Fourier domain) with a function that defines the transfer function of free space, as below

$$\tilde{E}_z = \tilde{E}_0 \times e^{jk_z z}, \quad (1)$$

where $\tilde{E}_z$ and $\tilde{E}_0$ denote the Fourier space electric fields at distance $z$ and at an initial plane with $z = 0$ respectively, and $k_z$ is the longitudinal wavevector given by

$$k_z = \sqrt{k^2 - k_x^2 - k_y^2}, \quad (2)$$

in which $k$ is the wavenumber, and $k_x$ and $k_y$ give the transverse wavevector components. The second term on the right-hand side of the equation for $\tilde{E}_z$ is the transfer function of free space. When the sum of the squares of the transverse components are larger than the square of the wavenumber, the longitudinal component of the wavevector becomes imaginary, turning the transfer function into an attenuating term that corresponds to high spatial frequencies in an electric field distribution that decay with propagation distance. These high spatial frequencies are

evanescent as they decay rapidly and are not resolvable more than a few wavelengths away from the initial plane. This formulation of scalar diffraction theory compactly summarizes light propagation in a system between two parallel planes and gives intuition into why there is a resolution limit arising related to the wavelength (i.e., as the wavelength decreases, higher spatial frequencies are resolvable because the longitudinal wavevector is larger). Another way to understand the angular spectrum is to think of the Fourier space electric field as decomposing the light into a summation of different planewave components that are propagating in different directions. When considering the angular spectrum in such a way, the transfer function determines the change in phase for a given planewave component based on its propagation direction and distance from the final plane.

While the angular spectrum is a general technique, often additional approximations can be made beyond just the assumption of scalar diffraction, such as the paraxiality of a wavefront. When the system is assumed to be paraxial, the planewave components in the angular spectrum of a wavefront are assumed to propagate at angle that is small with respect to the optical axis. This assumption gives rise to the well-known Fresnel diffraction integral [57], the effect of which can also be described by a convolution operation. In this case, the transfer function of free space can be simplified by performing a Taylor expansion with respect to the transverse wavevectors and neglecting higher order terms (i.e., since the transverse components must be small since we are making a paraxial approximation), yielding a Fourier domain transfer function

$$H = e^{jk\left(1-\frac{k_x^2+k_y^2}{2k^2}\right)}, \quad (3)$$

such that

$$\tilde{E}_z = \tilde{E}_0 \times H, \quad (4)$$

While the Fresnel approximation is simpler in that it does not require any square root term in the transfer function, the angular spectrum formulation is just as simple to implement in any standard programming language well-suited to scientific computing (e.g., MATLAB or Python) and as such, in our work we apply the angular spectrum method directly without making any approximations regarding the paraxiality of our wavefronts when simulating and designing metasurfaces.

When applying these propagation methods, there are a few additional details that must be considered. Firstly, as the convolution is applied using Fourier domain multiplication, we must zero pad the transfer function to prevent any wraparound effects since Fourier domain multiplication is equivalent to circular convolution in the spatial domain. This is circumvented by padding zeros onto the aperture such that if the electric field to be propagated is of shape $N \times N$, it is padded to be of shape $(2N-1) \times (2N-1)$ and after the filter is applied the result is cropped back to the original aperture size. Another complication occurs when light incident off-axis couples back into the simulation region at far propagation distances, which can be understood as an aliasing effect and is not solved by the zero padding as just described. To eliminate this artifact, we can simply apply an antialiasing filter that will zero out the high frequency (i.e., large propagation angle) components that should not be present within the aperture region after propagating some distance [58] (i.e., planewave components propagating at some angle with respect to the optical axis will eventually exit the finite aperture region after a certain distance). While this filter is not making any additional approximations, it removes the frequency components that should not be present at the output plane.

### 2.1.2 *Diffractive Optical Elements*

Conventional optical elements function based on refraction. For a lens, for example, its operation can be described in terms of rays bending at an interface such that they converge at a designed focal length some distance away from the lens surface. Alternatively, the operation of such a lens can be understood by treating the lens' sag profile as inducing different phase shifts at different positions (modelled via a split-step simulation through the lens' full thickness, or a single layer phase shift if the lens is considered thin), such that the light exiting the lens will all constructively interfere with itself at the focal spot. In this manner, if a lens is thin, the effect of the lens can be fully modelled by treating it as a phase mask and since phase is modulo $2\pi$, the lens' thickness function can be collapsed into zones of $2\pi$ phase, forming an analog Fresnel profile, also known as a kinoform [57]. In practice, kinoforms can be challenging to fabricate so it is common to approximate their phase with binary optics, which are essentially digitized versions based on discrete phase levels by adjusting the thickness of the constituent material.

## 2.2 METASURFACES

### 2.2.1 *Materials Considerations*

*This section is adapted with permission from* [52] © *The Optical Society.*

Metasurfaces have generated substantial research interest and attention in recent years. These ultrathin elements comprising arrays of subwavelength-spaced scattering elements can achieve a broad class of functionalities in a flat form factor, transforming the phase, amplitude, and polarization of incident electromagnetic radiation [6–8]. At optical frequencies, the promise of creating miniaturized imaging systems and multiplexing several functionalities into a single device has driven research in both academic and industrial labs [15,59,60]. While much of the initial

research investigated silicon and metal-based metasurfaces [6,13–15,18,34,39,40] for use in transformation optics and integrated optics, lower index materials became appealing because of their transparency at visible wavelengths where there are numerous applications in imaging, display, and spectroscopy. This initiated an exploration into low-loss dielectric platforms that could support high efficiency operation at visible wavelengths, producing a wide array of flat and visible wavelength metasurface elements and optical systems [24,25,42–49,51,61–63].

Many of the earlier works on optical metasurfaces were based on metallic scatterers [34–38]. The high plasma frequency of metals prevented these devices form working in transmission mode and the losses limited efficiency even for reflective devices. Silicon-based metasurfaces [13–15,18,39,40] enabled much lower loss devices that could operate efficiently both in reflection and transmission at infrared wavelengths. Recently, however, a wide range of lower refractive index materials have gained popularity as choices for scattering elements in optical metasurfaces due to their reduced optical absorption at visible wavelengths. Semiconductors generally obey the empirical Moss relation [64], where $n^4 \sim 1/E_{gap}$, motivating the selection of lower refractive index materials to increase the band gap and limit absorption. Such materials include include titanium dioxide [42–46,61], gallium nitride [47,48], indium tin oxide [65], and silicon nitride [24,49,62].

Titanium dioxide has gained popularity as a metasurface material because of its relatively high index (n ~ 2.6) while being transparent across the visible regime. While this material was previously used a couple decades back to make subwavelength blazed gratings [42,61], the platform was only recently popularized for metasurfaces after it enabled the first demonstration of imaging at visible wavelengths using a metasurface [43]. It has since allowed for a variety of metasurfaces [44,45], including a lens designed to be achromatic across the whole visible spectrum [46]. While the optical properties of titanium dioxide make it a great choice for

metasurface scatterers as its absorption is low, yet the refractive index is high enough to provide strong optical confinement, from a practical viewpoint this material has several limitations. These limitations primarily arise from scalable manufacturing concerns as titanium dioxide is deposited slowly via atomic layer deposition, limiting manufacturing throughput. As such, the material cannot leverage current CMOS-compatible foundry infrastructure for mass production, potentially hindering widespread adoption of the platform.

Gallium nitride (n ~ 2.4) has also found use in scatterer design in visible wavelength metasurfaces. It shares the relatively high refractive index and visible frequency transparency found in titanium dioxide. A metasurface full-color router for a Bayer pattern pixel used gallium nitride nanoposts [48] to discriminate red, green, and blue wavelengths and focus them to different positions. Separately, a gallium nitride-based achromatic lens was recently realized [47], providing broadband imaging at visible frequencies. While this material is promising in terms of optical properties, gallium nitride would also be difficult to adopt in existing CMOS foundries, like titanium dioxide.

Another existing material with index less than that of silicon used for metasurfaces is indium tin oxide (ITO) (n ~ 2). This material is not only transparent at visible wavelengths but is also conductive. The conductive properties of ITO are already being exploited to realize reconfigurable metasurfaces, using field-effect modulation of the refractive index to control the modes and resonances within adjacent scatterers. This index modulation enabled dynamic beam deflection by applying a spatially varying voltage to a gold grating with the change in the ITO's refractive index inducing a change in the scattering properties of the gold structures [65]. With the widespread use of ITO in displays, photovoltaics, and light-emitting diodes, ITO can be readily manufactured in existing foundries. Although currently there is little existing work on ITO-based metasurfaces, and

none to our knowledge using ITO as the scattering material itself, its optical and electrical properties, along with its established use in microfabrication, position ITO as a strong choice for future metasurface designs.

Of all the materials with refractive index less than that of silicon, the earliest reported visible wavelength metasurface lenses utilized silicon nitride (SiN) (n ~ 2) nanoposts as scatterers [49]. SiN is also the lowest refractive index material experimentally demonstrated in use for a metasurface to date and thus provides the widest band gap, with a transparency window extending from the infrared down to the near-ultraviolet regime. This broadband transparency makes SiN a versatile metasurface material, allowing a designer to use the same material and processing techniques for devices at different wavelengths across the transparent region. Furthermore, SiN is a CMOS-compatible material, enabling more streamlined integration with foundry infrastructure already in use for semiconductor microfabrication [66].

There are also other potential transparent metasurface materials, perhaps most notably silicon dioxide. Like SiN, this material not only exhibits a wide band gap but is a material that is widely used and is CMOS-compatible. While lossless, the lower refractive index (n ~ 1.5) of this material translates to lower beam deflection efficiency at high angles and reduced focusing efficiency for high NA lenses [55,67]. This reduced performance arises from the decrease in diffraction efficiency that, while minimal at low angles, becomes evident in lower index materials at moderate to high deflection angles [55,67]. While silicon dioxide is preferable compared to a variety of other dielectrics considering its CMOS-compatibility, its manufacturing advantages are matched by those of SiN, but it is inferior in terms of performance. This degraded performance is likely the reason there is an absence of experimentally realized silicon dioxide metasurfaces.

### 2.2.2 *Operation and Design*

*This section is adapted with permission from* [52] © *The Optical Society.*

Metasurface design requires specifying a spatial distribution of scatterers with varying geometric parameters to induce a transfer function for some desired near- or far-field optical response. For traditional diffractive optics relying on gradual phase accumulation, local phase shifts are proportional to the thickness of the element's material, but for metasurfaces the phase shift mechanism operates differently. There are different classes of scattering elements used, but for most dielectric metasurfaces, the phase response arises from either Pancharatnam-Berry phase elements [68,69] and the in-plane anisotropy of the scatterer, or from a cavity-like effect in which the scatterer behaves as a truncated waveguide supporting a mixture of Fabry-Perot resonances. In any case, the distinguishing feature of a metasurface is its subwavelength spatial resolution at the design wavelength, which for normal incidence (or any incidence for lattice spacing less than $\lambda/2$) eliminates higher diffraction orders [54]. This is a powerful feature of metasurfaces compared to multi-level diffractive optics with their super-wavelength spacing, as these elements produce nonzero diffraction orders and correspondingly achieve lower efficiency.

Designing metasurfaces entails selecting a simulation method to compute and test the optical response of the device. The design process can consist of either solving a forward problem, where the structure is designed using some analytical description or intuition to achieve the desired behavior, or an inverse problem in which the desired output is known, and the necessary structure is found via computational optimization. The forward technique has successfully been used to enable a class of flat optics including lenses [10–16], hologram generators [22,23], polarization elements [70,71], and vortex beam generators [17–21,71]. There are certain classes of devices,

however, with non-intuitive phase masks, such as multifunctional elements or multiplexers, which may require inverse design to achieve the desired performance.

#### 2.2.2.1 Forward Design

Forward design of a metasurface begins with identifying a desired behavior and specifying its transfer function in terms of a continuous phase mask. For many common elements, analytical forms for these masks exist and it is only required to select certain parameters (e.g., focal length, axicon angle, wavelength) based on the desired application. The continuous phase distribution is then converted to a spatially discrete profile, with the period equal to the scatterer lattice spacing. The phase at each position is then mapped to the scatterer design which most closely reproduces the desired phase. The phase response of the scatterers are stored in a library generated by electromagnetic simulations of scatterers using a periodic boundary condition, either by finite-difference time-domain (FDTD) or via rigorous coupled-wave analysis (RCWA) [56]. Once the geometric parameters of the metasurface are known, the whole structure may be simulated via FDTD if computational resources permit. Due to the memory intensive nature of FDTD simulation, often only a portion of the whole metasurface can be simulated. If simulating the whole structure is necessary, a less accurate method based on scalar diffraction theory can be used, treating the metasurface as a complex amplitude mask and evaluating light propagation and performance using a diffraction integral [57].

In the RCWA simulation, the periodic boundary condition ensures all the scatterers in the lattice have identical geometric parameters. When the metasurface is designed, however, the geometric parameters are varied from pixel to pixel, which is inconsistent with the assumptions made for RCWA. If the geometric parameters of neighboring pixels are varied slowly enough, then this discrepancy can be negligible. This assumption is referred to as the unit cell

approximation and when it is not valid it can pose significant limitations for the design process. While this approximation holds well for metasurfaces based on high index materials such as metals or silicon [13], optical confinement worsens with decreasing refractive index, as for SiN. This approximation is of less concern when designing devices that are slowly-varying, such as long focal length lenses, but for rapidly varying profiles such as those for holograms, it is necessary to assess the robustness of this approximation. A standard method for doing this is to examine a scatterer's behavior as a function of the lattice constant [13]. As the strength of coupling between adjacent elements is related to the gap between them, if the optical response varies rapidly with spacing, it is an indication that coupling is significant, and that the unit cell approximation is invalid. If, however, the phase and amplitude response of a scatterer remains invariant over a wide range of lattice spacings, then the scatterers are weakly-coupled to one another and it is reasonable to use the scattering response calculated assuming a periodic boundary condition. In this case, the nanoposts can be treated as pixels which behave locally and are unperturbed by their neighbors.

#### 2.2.2.2 Inverse Design

For the inverse design method, while the desired response is known, the exact metasurface structure to realize that behavior can be challenging to determine by forward methods. To circumvent this, a figure of merit is defined to quantify the performance of the device and upon successive iterations of solving the forward problem and updating the design parameters of the structure, the figure of merit can be optimized until the desired behavior is attained.

There are various existing algorithms for such optimization problems. One promising route is to use topology optimization combined with a finite-difference solver, which has already been applied in the context of designing multi-layer metasurfaces for angular aberration correction of a metalens as well as focusing of incident light to the focal length over a range of incidence

angles [72]. This approach requires definition of a desired phase profile which is included in the figure of merit and the method modifies the spatial permittivity distribution in a binary manner across a set of pre-defined layers. The layer thicknesses in this method are on the order of the wavelength and it inherently accounts for interactions and coupling between the layers. This work used silicon and alumina as the materials of choice but could be extended to lower index material platforms such as SiN as well. Topology optimization has also been used for designing high efficiency single layer beam deflection metasurfaces and free-space wavelength splitters, using a wide span of refractive indices (~1.5-3.5), including that of SiN [55]. In this case, RCWA was used to simulate periodic structures and the deflection angle of the unit cell was optimized. Significantly, higher refractive index materials performed better in general, achieving higher efficiencies; however, for low to moderate deflection angles the differences were not as appreciable. For a specified period, the optimized grating structure was similar in shape over a wide range of indices for achieving the same deflection angle, with similar modal structure, yet the difference in efficiency was attributed to greater intra- and inter-mode coupling.

Separately, a work [73] demonstrating inverse design of arrays of dielectric spheres successfully generated single and double layer metalenses using the adjoint method and generalized multi-sphere Mie theory (GMMT). While this work used spheres with a refractive index of 1.52, the index for polymers used in state-of-the-art two-photon polymerization 3-D printers, the algorithm was recently used in a separate study [67] for indices from 1.2-3.5, which includes the index for SiN. GMMT is a method based on the T-matrix formalism and can calculate the electromagnetic scattering off an ensemble of spheres [74–76]. Compared to the FDTD method, which requires extensive computational resources for meshing large structures, the GMMT technique leverages analytical expressions for scattering off spheres to reduce the

computational load. As GMMT does not require meshing individual scatterers, the required memory does not scale with system size, but rather the number of spheres and their density and the order to which the field is expanded [76]. By updating the radii of the spheres in the array each iteration, the figure of merit can be optimized by examining the gradient of the figure of merit with respect to the sphere radii using the adjoint method. Leveraging this, successful inverse design and simulation of focusing lenses was shown, in strong agreement with results computed via FDTD for comparison [73]. The technique was extended to multiple layers of metasurfaces, enabling possible future inverse design of volumetric optical elements with subwavelength sphere-based voxels.

# Chapter 3. FULL-COLOR IMAGING

Excerpts and figures in this section are from *Colburn, Shane, Alan Zhan, and Arka Majumdar. "Metasurface optics for full-color computational imaging." Science Advances 4.2 (2018): eaar2114.* Reprinted with permission from AAAS.

## 3.1 INTRODUCTION

Due to the wavelength sensitivity of metasurfaces, designing general-purpose achromatic metasurface lenses (metalenses) remains a challenging problem. As the focal length of a metalens depends on the illumination wavelength, as the wavelength deviates from the designed value, the metalens exhibits a chromatic axial focal shift that arises from the phase-wrapping discontinuities in the structure's profile [77]. Such chromatic focal shifts are common to other diffractive optical elements as well, such as multi-level Fresnel optics. As such, in an imaging scenario, broadband illumination manifests as severe color blur or ringing in captured images.

Some works examined this challenge from the perspective of achieving multiwavelength operation at several discrete wavelengths. In these designs, scatterers or the aperture are optimized to provide the required phase for each of the discrete wavelengths being designed for but are left unoptimized for intermediate wavelengths [77–81]. As such, while these designs may work for systems in which the wavelengths are fixed and known a priori, in an imaging scenario with ambient lighting or a broad wavelength range, these lenses would exhibit strong chromatic aberrations for intermediate wavelengths.

There are also several works that have recently demonstrated broadband achromatic lensing [45–47,82–84] and imaging at both visible and infrared wavelengths. Common to these designs are the idea of modifying the phase function of a traditional metalens to incorporate a

phase compensation or dispersion term that effectively imparts higher order terms in the Taylor expansion of a metalens' phase as a function of illumination frequency. If all the higher order terms of the expansion could be imparted, then a lens would not exhibit any chromatic aberration. In practice, however, only expanding to the first or second order is necessary to achieve achromatic focusing with metasurfaces. While this method has demonstrated impressive imaging and broadband capability, it is, unfortunately, quite limited in scope as it is only feasible for small area lenses [83]. As the first order term (the dispersion, or change in required phase as a function of frequency) changes approximately quadratically with aperture radius, the phase compensation required increases drastically as the required area of the device increases. If appropriate scatterers could be designed to meet these dispersion requirements this would not pose an issue, but such high dispersion would necessitate exceedingly high-quality factor resonators or high aspect ratio elements beyond the capabilities of state-of-the-art nanofabrication [85]. As such, dispersion-engineered broadband achromatic metalenses are constrained to small areas, which limits their light collection and contributes to reduced signal-to-noise-ratio in captured images. Furthermore, to achieve such high operating bandwidths, these designs typically utilize specialized scatterer designs that rely on circularly polarized illumination, requiring additional polarizers and waveplates that increase system size and complexity while reducing efficiency.

## 3.2 DESIGN

To circumvent these scaling limitations and realize a broadband (full visible spectrum) metalens-based imager, we leveraged the cubic phase modulation from wavefront coding [27] to enable a hybrid optical-digital metalens system for full-color imaging [25]. Unlike counterpart broadband achromatic metasurface systems, this design required no specialized scatterer design but utilized a simple and polarization-insensitive cylindrical nanopost. Also, unlike existing

wavefront coded systems for extending the depth of field or mitigating the chromatic focal shift of refractive lenses [29], our design does not require a separate phase mask or 4f relay optics to impart the desired phase modulation. Instead, we designed a single metasurface that simultaneously implements the focusing and wavefront coding functionality coupled with deconvolution software that together yield in-focus images for the full visible spectrum (400-700 nm).

Our device design consisted of a metasurface with silicon nitride nanoposts in a square lattice with diameters assigned such that the device imparted the phase function

$$\varphi = \frac{2\pi}{\lambda}\left(\sqrt{x^2 + y^2 + f^2} - f\right) + \frac{\alpha}{L^3}(x^3 + y^3), \quad (5)$$

where x and y are the in-plane coordinates, λ the operating wavelength, f the focal length, L the aperture radius, and α the cubic phase strength (number of 2π cycles from the cubic term that are traversed in going from the origin to the aperture edge in the positive x or y direction). When α = 0, we get a regular metasurface lens but when it is nonzero, the cubic phase modulation extends the depth of focus of the system and modifies its point spread function (PSF). We designed two lenses, one with α = 0 (singlet metalens) as a baseline for comparison, and another with α = 55π (extended depth of focus, EDOF, metalens). Figure 3.1A-C [25] show a schematic of the nanopost design and the corresponding transmission coefficient simulation that were used to design these metasurfaces. In Figure 3.1D-E, simulated intensity cross sections along the optical axis of the two metasurface designs are shown. While the singlet metalens only focuses on the sensor plane (the dashed line) for one wavelength (the 550 nm design wavelength), the EDOF metalens, even with an evident chromatic shift, still produces focusing at the desired plane for all tested wavelengths, demonstrating the power of extending the depth of focus of the lens to ensure information is transferred to the sensor plane for a broad wavelength range. Figure 3.1F-G shows optical images of fabricated versions of these two simulated designs.

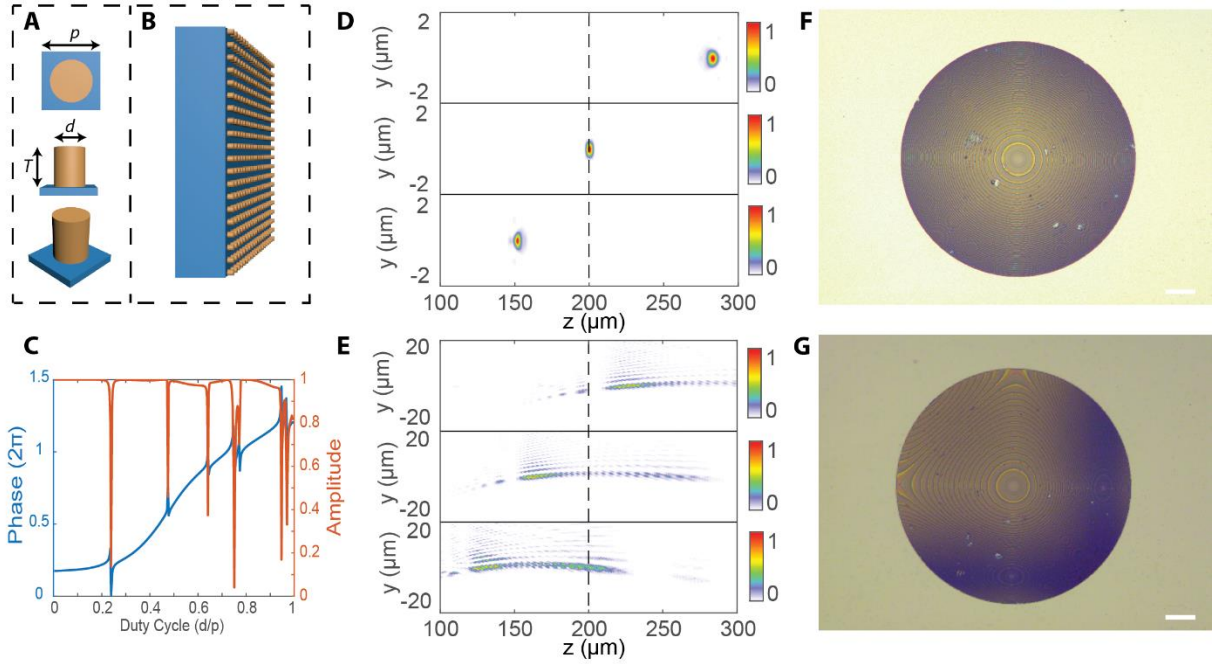


Figure 3.1. Design, simulation, and fabrication of imaging metasurfaces. (A) The metasurfaces are made up of silicon nitride nanoposts, where the thickness T, lattice constant p, and diameter d are the design parameters. (B) Schematic of a metasurface comprising an array of nanoposts. (C) Simulation of the nanoposts' transmission amplitude and phase via rigorous coupled-wave analysis. Simulated intensity along the optical axis of the conventional metasurface lens (D) and extended depth of focus metasurface (E) where going from top to bottom in each panel 400, 550, and 700 nm wavelengths are used. The dashed lines indicate the desired focal plane, where the sensor will be placed. Optical images of the conventional metasurface lens (F) and the extended depth of focus device (G).

## 3.3 Fabrication and Characterization

To characterize the experimental performance of these metasurfaces, we measured their point spread functions and then calculated their MTFs (data presented in Figure 3.2 [25]). While the singlet metalens exhibits a tightly focused spot for its PSF at the design wavelength, it produces large diffraction blurs for blue and red illumination (Figure 3.2A-C). Likewise, the corresponding MTFs exhibit large variation in performance between wavelengths with zeros in the spectra for blue and red (Figure 3.2D), presenting an unrecoverable loss of spatial frequency content when imaging as these wavelengths due to the diffraction blurs reducing the resolving power. Unlike the singlet metalens, however, the EDOF metalens exhibits near spectrally invariant PSFs and MTFs (Figure 3.2E-H). While the PSFs are not point-like and as such will produce blurry images, the near uniformity of their response enables us to use a single PSF calibration measurement to deconvolve all colors simultaneously in captured images. Furthermore, while the singlet metalens exhibits zeros in the MTFs for blue and red illumination, the EDOF metalens only has an attenuated frequency response for all wavelengths and as such these frequencies are still recoverable (Figure 3.2H).

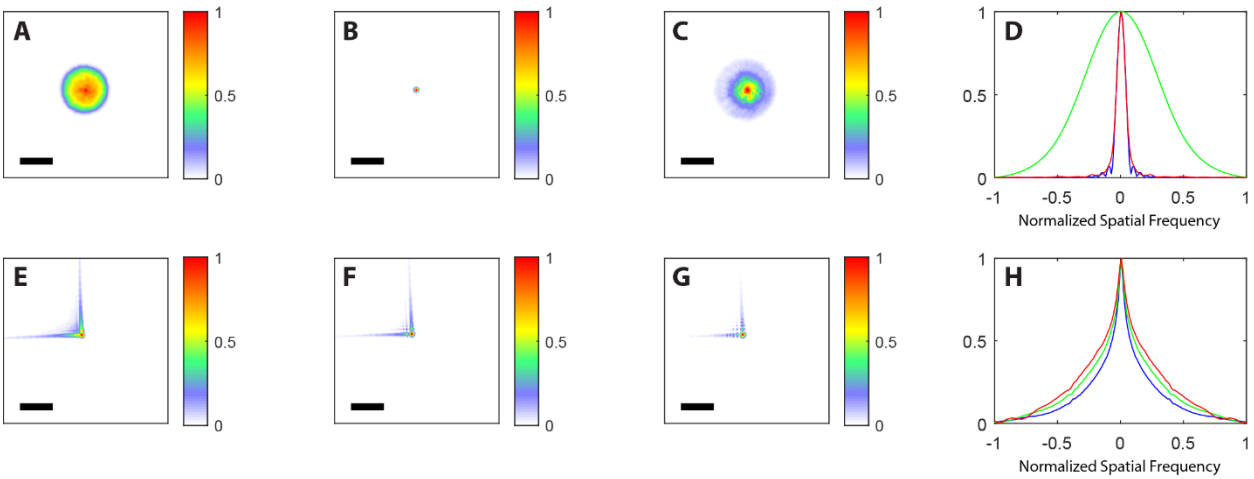


Figure 3.2. Characterization of the imaging metasurfaces. The PSFs of the conventional metasurface lens (top row) and extended depth of focus lens (bottom row) were measured under blue (A and E), green (B and F), and red (C and G) illumination conditions. The scale bars are of length 25 μm. The MTFs were also calculated for both designs (D and H).

## 3.4 IMAGING EXPERIMENT

To test the imaging performance, we first illuminated black-and-white patterns with discrete wavelength LED sources (~20 nm bandwidth) and captured images using both the singlet and EDOF metalenses (Figure 3.3 [25]). While the singlet demonstrated focused images for green light, it produced severe distortions at off-design wavelengths, namely red and blue. The EDOF metalens instead produced uniformly blurry images for all wavelengths but after deconvolution generated in-focus images at all wavelengths, albeit with reduced signal-to-noise-ratio (SNR) due to the focal intensity being distributed over a greater volume because of the extension of the focal depth. We then tested under white-light illumination using a broadband LED source and full-color patterns (Figure 3.4 [25]). Once again, while the singlet metalens was focused at its design wavelength, it severely blurred off-design wavelengths, whereas the EDOF metalens rendered focused images for a broad color range, enabling distinction between characters in colored text patterns and different bands in a rainbow pattern that the singlet metalens blurred.

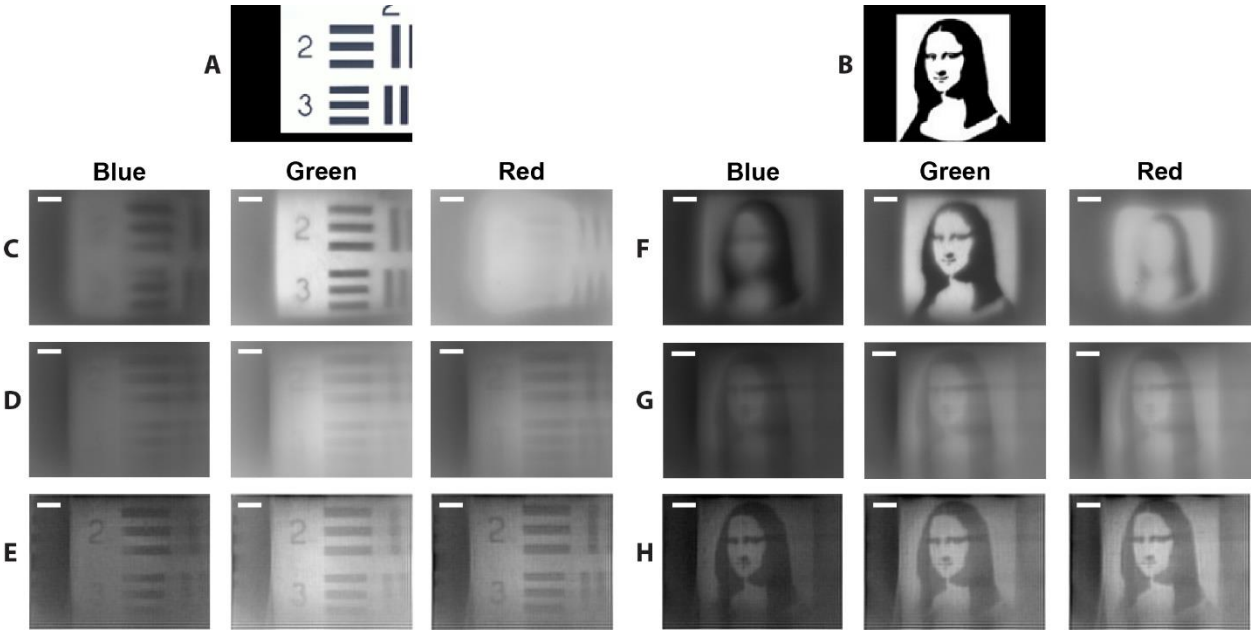


Figure 3.3. Imaging at discrete wavelengths. Images were captured of the 1951 Air Force resolution chart with the conventional metasurface lens (A) and the EDOF lens without (B) and with deconvolution (C). Images were also taken of a binary Mona Lisa pattern with the standalone ordinary metasurface lens (D) and the EDOF without (E) and with (F) deconvolution.

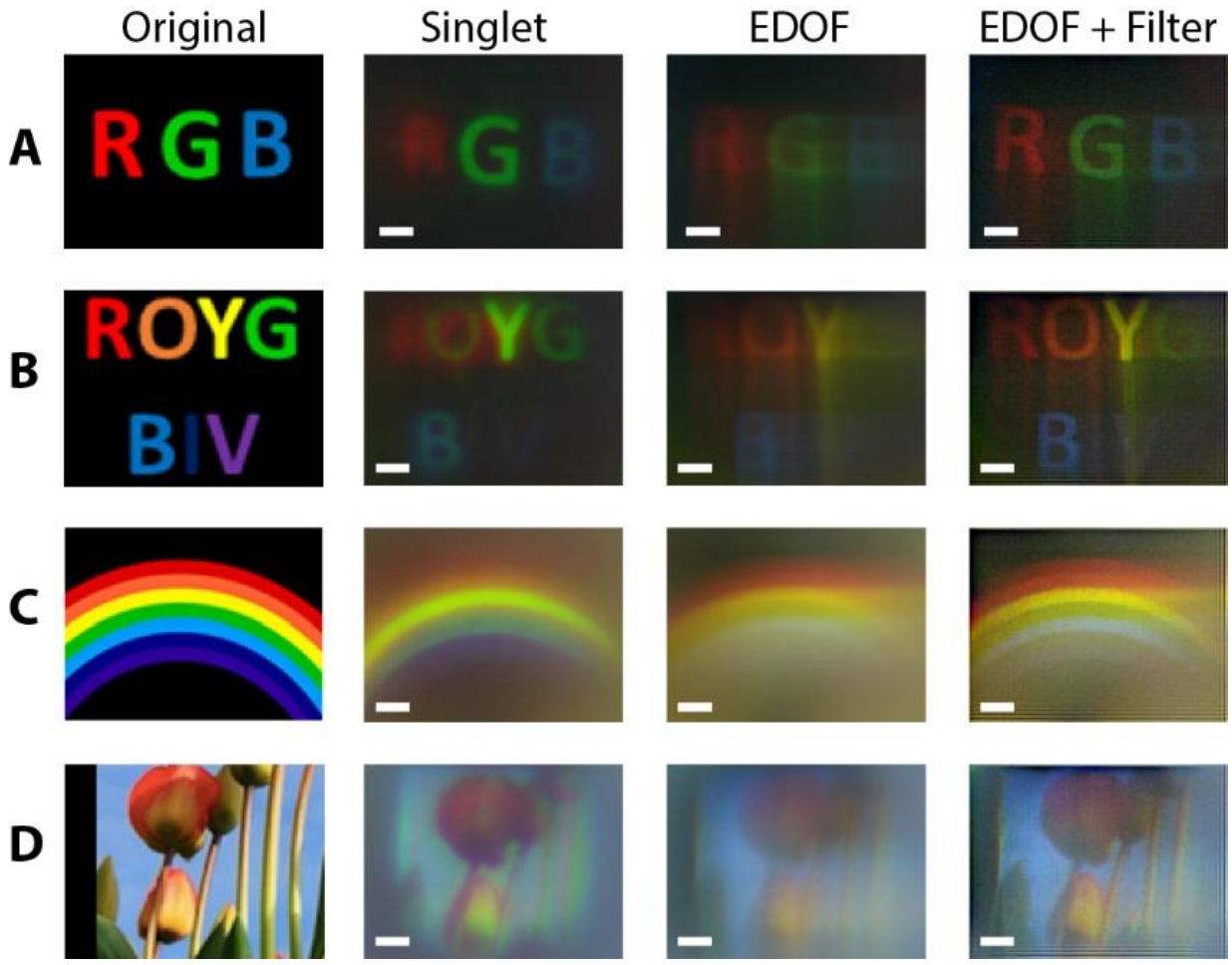


Figure 3.4. Imaging with white light. Images were taken under white light illumination of color printed RGB (A) and ROYGBIV (B) text, a colored rainbow pattern (C), and picture of a landscape (D) with a blue sky, green leaves, and multicolor flowers.

## 3.5 DISCUSSION

With the demonstration of white-light imaging using an EDOF metalens, we have made significant progress toward our goal of realizing a full-color metasurface-based computational imaging system. There is, however, still room for improvement. Notably, the deconvolved images exhibit nontrivial haze and noise but there are many routes towards mitigating this. One possibility is calibrating the Poisson and Gaussian components of our sensor [86] and incorporating these as priors to denoise the image. Separately, much of the noise arises from the low-light conditions in which we were imaging and the low light collection due to the limited area of our aperture (200 μm wide aperture) that we were constrained to working with because of the cost of fabricating larger devices using University equipment. Larger area apertures are well within the capabilities of high-throughput DUV lithography systems and our expenses only arose from the costly electron-beam lithography process we had to use to achieve our feature sizes. We also used relatively simple deconvolution algorithms, but there are existing methods with regularization terms to simultaneously denoise and deblur images [4]. These improvements could also be combined with alternative wavefront coding terms in place of the cubic phase modulation term to eliminate asymmetric artifacts in images arising from the shape of the PSF [87].

# Chapter 4. VARIFOCAL ZOOM IMAGING

*This section is adapted with permission from* [26], *S. Colburn, A. Zhan, and A. Majumdar, "Varifocal zoom imaging with large area focal length adjustable metalenses," Optica, OPTICA 5, 825–831 (2018). © The Optical Society.*

## 4.1 INTRODUCTION

As detailed in the preceding sections, exploiting arrays of subwavelength-spaced optical antennas, metasurfaces can apply spatially varying transfer functions on incident wavefronts [6–9], including those of lenses [10–16], holograms [22,23], polarization elements [71], vortex beam generators [17,19–21,71,88], and blazed gratings [41,42]. Most demonstrated metasurface devices to date, however, have been static in nature. For metalenses, focal length tuning over a wide range is of substantial interest in photography, microscopy, mixed reality, and optical communications. Stretching of metalenses on flexible substrates [89–92] is one route to accomplish this, but this entails constant application of an external force to counteract the substrate's restoring force. Furthermore, electrical control of such systems requires high voltages (kV range) as the tuning mechanism relies on a capacitive electrostatic force to compress an elastomer [92]. Microelectromechanical systems (MEMS)-based tuning is promising, with recent results adjusting the angular orientation of a metalens [93] or demonstrating large changes in optical power by actuating a metalens axially in a compound lens system [94]. Unfortunately, although MEMS devices are quite effective at short length scales, their electrostatic actuation mechanisms cannot be scaled to the macroscale sizes [95,96] necessary for applications requiring large apertures and focal lengths, such as for eyeglasses and mixed reality displays [59,63]. For large area devices with correspondingly higher tuning ranges and a more massive system, a larger gap distance and

actuation is required. With the increased mass and actuation distance, however, the required forces can become too large for electrostatic MEMS devices. As the applied force is proportional to the derivative of the capacitance, with the increased gap, the decrease in capacitance must be compensated by an increase in voltage [97]. With centimeter scale devices, the voltage required to induce sufficient displacement of large area metalenses would cause electrical breakdown and device failure [95–97].

Here, we develop a large area tunable focal length metalens system using an Alvarez lens design [24,98], combining two separate cubic metasurfaces that under lateral actuation give rise to a rapid and nonlinear change in focal length [Figure 4.1(a)]. Unlike most previous metasurface works, we fabricate our device using high-throughput stepper photolithography, circumventing the scalability issues of electron-beam lithography to build a large area (1 $cm^2$ aperture) device. Our process flow relies on a custom-developed compression algorithm which can substantially reduce the complexity of layout files, enabling us to create a metalens with nearly 120 million scatterers with, to the best of our knowledge, the largest focal length range demonstrated to date. We use a versatile silicon nitride cylindrical nanopost platform, which is polarization-insensitive, and well suited for efficient operation from the visible to the infrared. In this work, our Alvarez metalens is actuated manually using translation stages; however, electrical actuation is well within the means of commercially available miniature stepper motors [99]. We propose this actuator mechanism for the case of large area metalenses, maintaining that such a mechanism is not well suited for microscale structures, where MEMS-based actuators are effective. With the wide aperture of our system, we demonstrate its utility for varifocal zoom imaging without requiring any additional elements (e.g., objectives or tube lenses) in the optical path, achieving a magnification range with 4x zoom capability in our experiments.

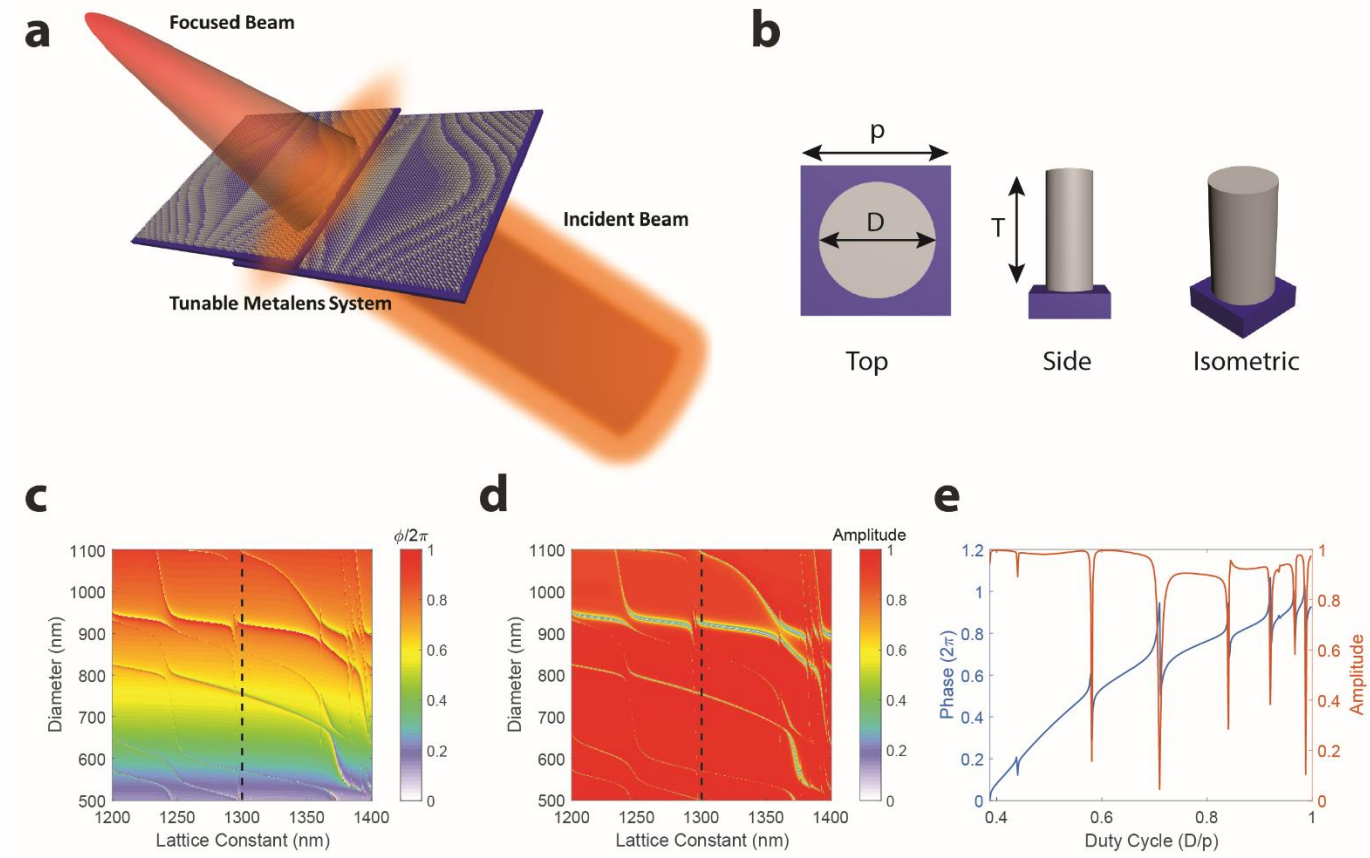


Figure 4.1 Simulation and Design of Nanoposts (a) Schematic representation of our tunable metalens system comprising two cubic metasurface phase plates actuated laterally. (b) Top, side, and isometric views of our silicon nitride nanoposts where T is thickness, D is diameter, and p is lattice constant. The simulated amplitude (c) and phase (d) of the transmission coefficient as a function of nanopost diameter and lattice constant are shown. (e) The phase and amplitude for a fixed lattice constant of 1.3 μm corresponding to the black dashed lines in (c) and (d).

## 4.2 DESIGN

### 4.2.1 *Theory and Simulation*

The phase profile of a spherical singlet metalens follows a quadratic form which is inversely proportional to its focal length. An Alvarez lens instead comprises two separate cubic phase plates that in conjunction give rise to a tunable focal length lens when the plates are actuated laterally with respect to one another. These phase plates are typically implemented using freeform glass surfaces or multi-level diffractive optics, entailing sophisticated and expensive fabrication. For our design, we use two flat metasurface phase plates where one plate obeys a cubic polynomial function and the other follows the same function but with opposite sign. When the plates are aligned along the optical axis and positioned parallel to one another, under lateral actuation the total phase profile imparted on an incident wavefront is a quadratic function with changing focus. The phase profiles of the regular and inverse metasurfaces are

$$\varphi_{\mathrm{reg}}(x,y) = -\varphi_{\mathrm{inv}}(x,y) = A\left(\frac{1}{3}x^3 + xy^2\right), \quad (6)$$

where A is a constant with units of inverse cubic length and (x,y) represents the in-plane position. The constant A denotes the cubic phase strength and is equal to $\frac{2\pi\alpha}{L^3}$, where $L$ is half the aperture width, and α gives the number of 2π cycles exhibited in traversing a path along the x-axis from the origin to the edge of the aperture of the cubic mask. Translating these phase masks by a displacement d in opposite directions, we obtain a quadratic form as below

$$\varphi_{\mathrm{Alvarez}}(x,y) = \varphi_{\mathrm{reg}}(x+d,y) + \varphi_{\mathrm{inv}}(x-d,y) = 2Ad(x^2+y^2) + \frac{2}{3}Ad^3, \quad (7)$$

Neglecting the constant $\boldsymbol{d^3}$ phase term and relating the quadratic term to the phase of a spherical singlet, we find the focal length as a function of displacement as

$$f(d) = \frac{\pi}{2\lambda A d}, \quad (8)$$

where f is the focal length and λ is the wavelength. The inverse dependence of the focal length on the displacement d induces a nonlinear and rapid change in focal length for small displacements. For a design wavelength of 1550 nm, we select the value $A = 6.756\,x\,10^9 m^{-3}$ such that by changing d from 1 mm to 4 mm, we can tune the focal length continuously from 3.75 cm to 15 cm.

To implement our tunable lens, we need to design dielectric scatterers capable of supporting high efficiency operation while remaining compatible with the spatial resolution achievable with photolithography. For the designed focal length, a large aperture is required to cover the necessary actuation range and achieve a numerical aperture (NA) high enough to image with sufficient resolution. While large area metalenses with moderate to high NA do exist, these devices rely on expensive and time-consuming electron-beam lithography, precluding widespread commercial adoption. Recently, mass manufacturing-compatible large area metalenses at 1550 nm were reported [100]. Our process flow is similar to this work [100], however, we use a silicon nitride nanopost platform and demonstrate devices on both silicon and quartz substrates, enabling visible wavelength operation in addition to 1550 nm. While our selection of silicon nitride as the nanopost material limits beam deflection efficiency at high angles [55] and focusing efficiency at high numerical apertures [67] relative to state-of-the-art high index silicon-based metalenses, the platform is advantageous in providing lossless operation over a broad wavelength range, unlike silicon devices that absorb significantly at visible wavelengths. Depending on the application and

wavelength of interest, our design process can be adapted to different nanopost materials, contingent on whether absorption or diffraction efficiency at high angles is of higher priority.

To work within the constraints of our university cleanroom's stepper lithography system, we limited the minimum diameter of our silicon nitride cylindrical nanoposts [Figure 4.1(b)] to 500 nm and designed scatterers using rigorous coupled-wave analysis (RCWA) [56]. Figure 4.1 (e) shows the simulated transmission coefficient at 1550 nm of our designed 2 μm thick silicon nitride nanoposts on a silicon substrate. We use a lattice spacing of 1.3 μm and have diameters ranging from 500 nm to 1.1 μm. As evidenced by the minimal variation in transmission coefficient over a wide range of lattice periodicities [Figure 4.1 (c)-(d)], we can approximate our nanoposts as weakly coupled dielectric scatterers, justifying our subsequent use of the unit cell approximation in designing the metasurface [13]. These nanoposts can be understood as behaving like truncated circular waveguides in which the discontinuities in refractive index at the top and bottom interfaces of the scatterers produce Fresnel reflections and low-quality factor Fabry-Perot resonances. Together these modes produce the nanoposts' complex transmission coefficient. The transmission coefficient in Figure 4.1(e) exhibits multiple resonances, which we attribute to guided mode resonances (GMRs) arising from coupling of incident radiation to surface modes in the grating layer. The electromagnetic power of GMRs is strongly confined within the grating layer but can still couple to free space [101,102]. Near the post diameters exhibiting GMRs, the phase varies rapidly and the amplitude drops significantly, but as we select diameters off resonance when designing our metasurfaces, these changes in amplitude do not impact our efficiency. GMRs are extensively studied in photonic crystal slabs and metasurfaces and they can be eliminated by ensuring the phase matching condition is not satisfied [45,101–103]. To break this condition, the

center-to-center distance of the nanoposts needs to be reduced to less than the effective wavelength inside silicon nitride, which is feasible using state-of-the-art Deep UV stepper lithography systems.

### 4.2.2 *Fabrication*

To make our metasurface cubic phase plates, we used the calculated transmission coefficient data as a lookup table, mapping the desired phase to the corresponding nanopost diameter. Fabricating the desired metasurfaces required manufacturing a reticle in accordance with a layout file, such as a GDSII, detailing the positions and diameters of nearly 120 million nanoposts. Whereas layout files for typical metasurface designs usually contain individual cells for each nanopost due to the small number of individual posts, for the exceedingly large number of elements in our design, we had to develop an algorithm based on hierarchical cell references to reduce the required memory. Minimizing the memory is critical, as layout files must undergo computationally demanding processing, such as fracturing, to convert the data into the proper format for manufacturing a reticle. With the number of elements increasing quadratically with a linear increase in aperture width, layout file compression is crucial to be able to support large area metalenses. By writing our layout file using our algorithm and converting to an OASIS file, we achieved more than a 2600x reduction in memory. While a previously developed metasurface layout file compression algorithm [100] showed an even larger reduction, our algorithm is more general in that it does not require any symmetry in the layout and can be used for general phase masks such as those for holograms or our cubic masks.

Figure 4.2(a) schematically summarizes our fabrication process flow, including deposition, spin coating, stepper lithography, hard mask patterning and etching, and mask removal. Figure 4.2(b) and Figure 4.2(c) show a standard 100 mm wafer after our exposure step and an etched and cleaved cubic metasurface phase plate with a hand for scale respectively. In Figure 4.2(d) and 2(e), we can

see scanning electron micrographs of the fabricated nanoposts from normal and diagonal (45°) views respectively. In addition to the designed metasurface Alvarez lens, our reticle also included several static singlet and vortex beam-generating metalenses to demonstrate the versatility of our nanopost design and fabrication process. In characterizing these devices, we saw close to diffraction-limited performance and successful generation of vortex beams with different orbital angular momentum states (Figure 4.5).

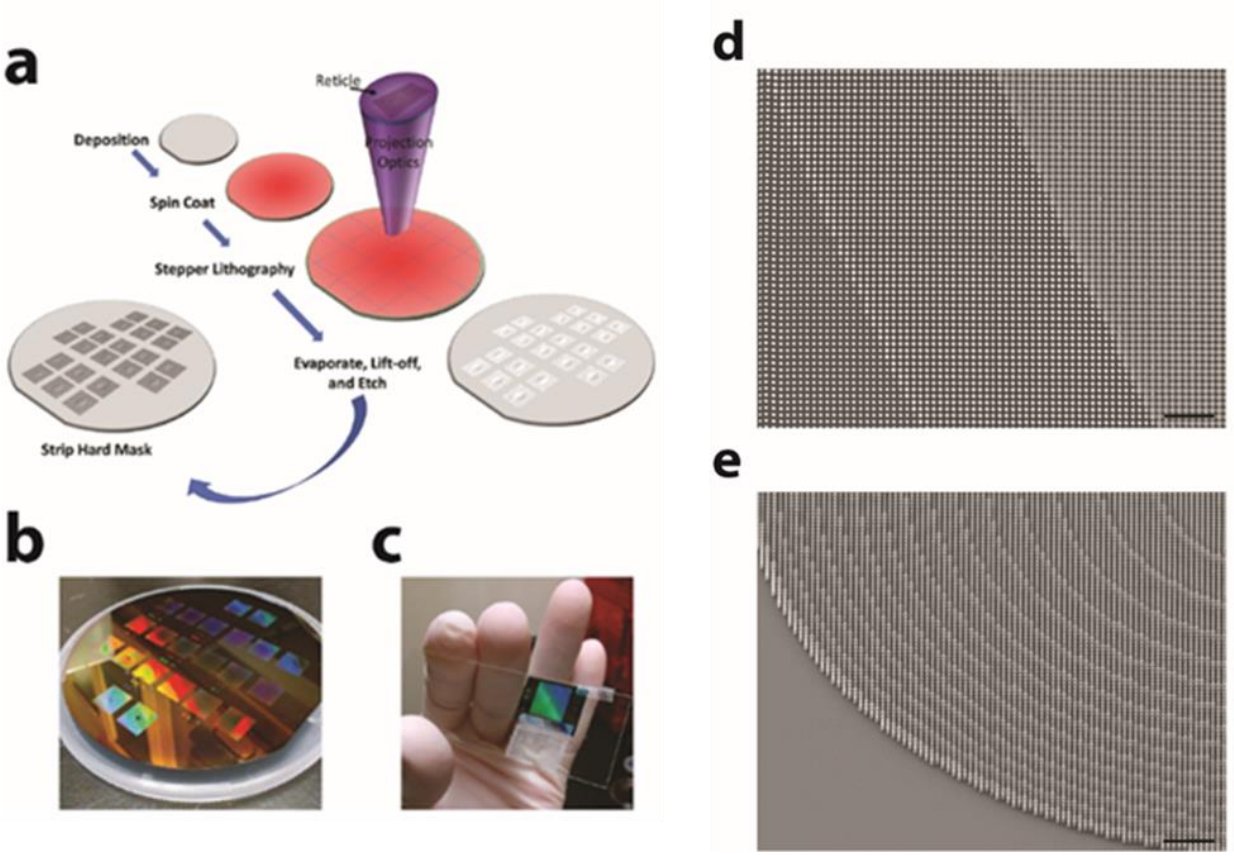


Figure 4.2. Fabrication of the large area metasurfaces. (a) Schematic of the process flow for fabricating multiple large area metalenses in parallel using high-throughput stepper lithography-based processing. (b) A fully exposed and developed 100 mm wafer, showing the capability to make large area devices. (c) A fully etched and cleaved metasurface cubic phase plate with a hand for scale. Scanning electron micrographs of fabricated nanoposts are shown at normal incidence (d) and 45° incidence (e). Scale bars 10 μm.

## 4.3 Experimental Results

We experimentally verified the tunable behavior of our Alvarez metalens system by laterally displacing the regular and inverse cubic metasurfaces with respect to one another (see Figure 4.6A for a schematic and description of the measurement setup). We displaced the metasurfaces over a 2.75 mm range, translating to a nonlinear change in focal length over a 6.62 cm range at 1550 nm, matching closely with the theoretical focal lengths [Figure 4.3(a)]. With the same reticle layout, we also fabricated a lens on a quartz substrate to operate at 633 nm wavelength. While this visible regime device is not strictly a metasurface due to its super-wavelength lattice periodicity, the near-wavelength spacing still enables a wide range of phase shifts as a function of diameter, even with fixed nanopost thickness [Figure 4.3(b)]. For this simulation, the nanoposts have the same lattice constant as before, but we use a lower thickness of 1.5 μm, which exhibited higher transmission amplitude. In having the same spatial arrangement of nanopost positions and diameters by using the same reticle as for the silicon substrate design, the metalens will still focus; however, as chromatic aberrations in metasurfaces are primarily a result of phase-wrapping discontinuities [77], in illuminating at 633 nm the phase function will exhibit discontinuities which will induce a chromatic focal shift. The resultant focal length of the metalens on quartz can be estimated via equation (8) and the strong agreement of this theoretical focal length and the experimentally measured focusing (Figure 4.6B for a schematic and description of the measurement setup) confirms this behavior [Figure 4.3(c)].

The visible lens design with its super-wavelength lattice constant does, however, come at the cost of producing higher diffraction orders that are absent for devices on a subwavelength lattice. The 1550 nm and 633 nm designs achieved focusing efficiencies of 57% and 15% respectively at

a displacement d of 2.5 mm. The large efficiency drop at 633 nm is attributed to light being lost to these additional diffraction orders, and when considering the focusing efficiency of the zeroth order beam alone (i.e., neglecting light lost to higher order diffraction) we achieve an efficiency of 58%, close to that of the 1550 nm device. We note that our university cleanroom sets a lower limit on our achievable lattice constant, but subwavelength lattices for visible frequencies are well within the capabilities of state-of-the-art deep-UV lithography systems (see Figure 4.8 for a nanopost design compatible with such systems). With a subwavelength lattice constant, we could suppress these higher diffraction orders and increase the efficiency of the 633 nm design. As calculated via angular spectrum propagation [57], the theoretical focusing efficiency of our 1550 nm lens is 92%, indicating a significant drop in performance arising from fabrication imperfections, likely resulting from overexposure of the nanoposts during the lithography stage. Furthermore, we also attribute this drop to the fact that our system comprises two optical elements, where it is assumed that light is normally incident on all scatterers in RCWA, but for our second cubic phase plate, the incident wavefront consists of oblique wavevectors after being diffracted by the first plate. This alters the scattering properties of the nanoposts and prevents exact implementation of the desired phase profile.

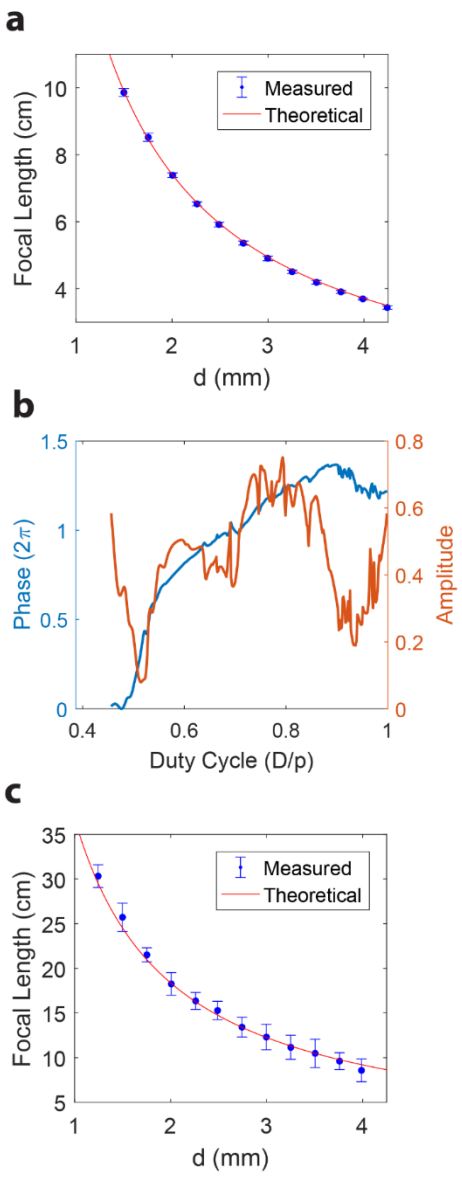


Figure 4.3. Experimental and theoretical focal lengths of the tunable lens designs. Focal length as a function of lateral displacement for the infrared (a) and visible (c) designs are shown. Errors bars represent a 95% confidence interval where the 1σ uncertainty is estimated during measurement by finding the range of distances over which the lens appears to be in focus. (b) Simulated transmission coefficient of the 1.5 μm thick silicon nitride nanoposts on a quartz substrate.

Our widely focus-tunable lens is well suited for imaging with different values of magnification for varifocal zoom applications. To examine the imaging performance of our device, we illuminated a 1951 Air Force resolution test chart with a 625 nm LED in transmission and imaged the pattern directly onto a camera with our tunable lens on a quartz substrate without the use of supplemental optics (Figure 4.7A for a schematic and description of the measurement setup). By fixing the test chart 30 cm away and tuning the focal length from 10 to 20 cm (1.8 mm actuation of each metasurface) and appropriately shifting the camera to the image plane, we provided magnifications ranging from 0.5x to 2x, achieving a 4x zoom range [Figure 4.4(a)]. We repeated this measurement for imaging a Mona Lisa pattern prepared on standard printer paper by scattering the LED light off the pattern (Figure 4.7B). To demonstrate the narrow actuation range required for changing the optical power of our metalens and its effect on imaging, we varied the degree of lateral misalignment of the two plates over a small range (-250 μm to + 250 μm) and recorded a video of the Air Force pattern with this actuation in real-time. Snapshots at specific levels of misalignment are also provided in Figure 4.4(b). The narrow range required to actuate the device demonstrates the sensitivity of this tuning method, where the nonlinear change in focal length is very abrupt as a function of displacement. The shifting and blurring of the image pattern in Figure 4.4(b) arise from the alteration to the system's phase function, in which the misalignment both longitudinally shifts the focal plane and adds a linear phase ramp that laterally translates the image.

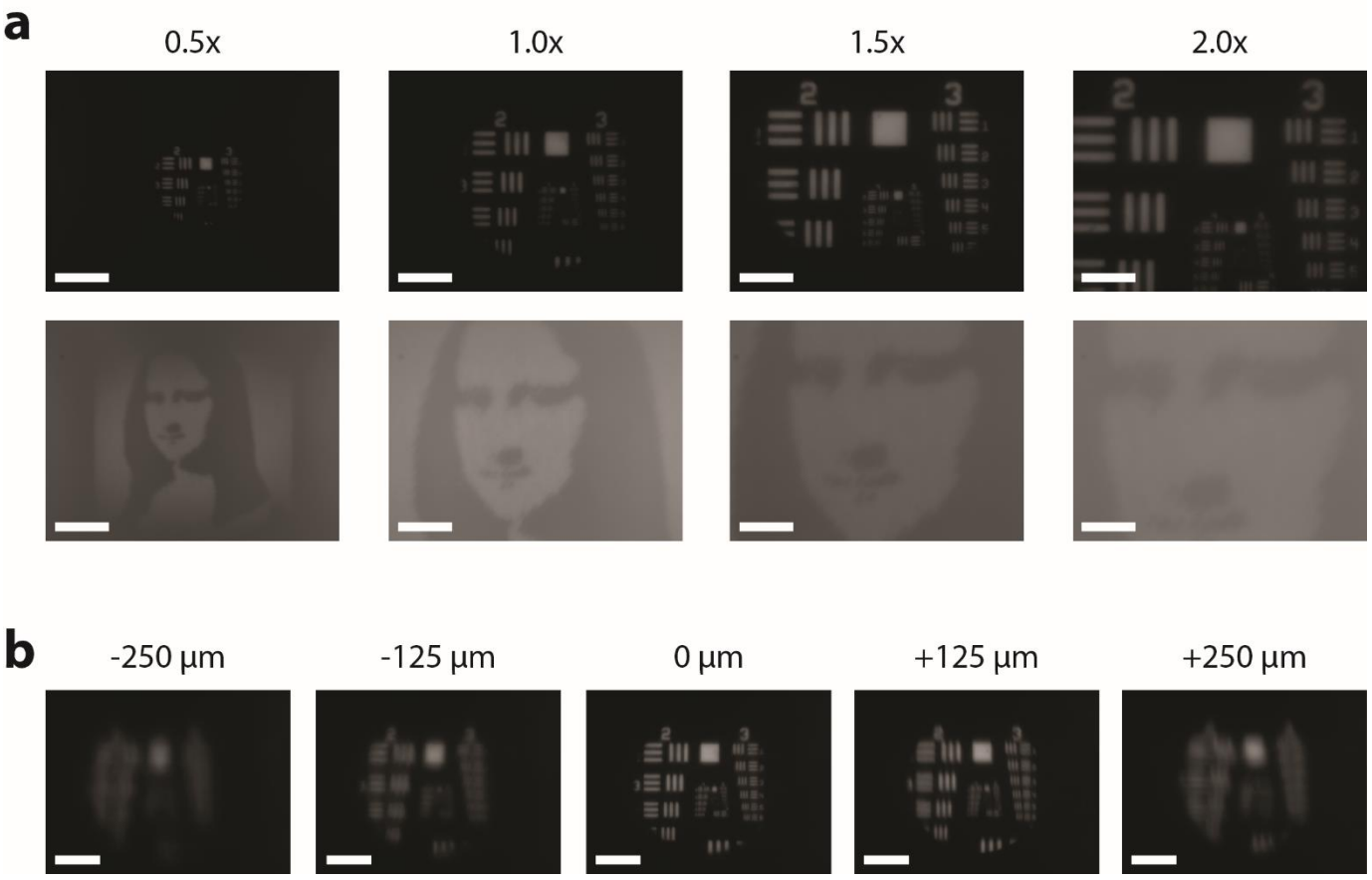


Figure 4.4 Imaging with different magnifications using the visible lens design. (a) Examples of images captured without any optical elements aside from the tunable lens system in the optical path using an Air Force resolution test chart illuminated in transmission (top row) and a Mona Lisa pattern printed on paper illuminated by scattering light off the pattern (bottom row). (b) The effect of misaligning the regular cubic metasurface phase plate on image quality. The scale bar is 1.2 mm for all images.

## 4.4 Discussion and Conclusion

Our tunable metalens system demonstrates a large change in optical power (20.8 diopters at 1550 nm and 9.2 diopters at 633 nm) with, to the best of our knowledge, the largest focal length range (6.62 cm at 1550 nm and 32.4 cm at 633 nm, 205% and 378% changes, $\frac{f_{max}-f_{min}}{f_{min}}$, respectively) for an optical metasurface demonstrated to date. Table 1 summarizes and compares some of the properties of existing mechanically tunable metalenses with the devices demonstrated in this work, indicating our designs achieved only moderate changes in optical power but very large focal length ranges. This large tuning range is enabled not only by the inverse proportionality between focal length and displacement for Alvarez lenses, but also by our developed stepper lithography platform and silicon nitride nanoposts, which can provide elements with much wider apertures using methods compatible with mass manufacturing. Currently, however, the metasurfaces in our demonstrated device are actuated by hand using micrometer translation stages. Such stages would be incompatible for any portable lens platform. Whereas the wide aperture of our device is one of its primary benefits, the corresponding increased mass of our optical element precludes MEMS-based actuation as demonstrated with other tunable metasurface systems [93,94]. The actuation is, however, well within the capabilities of commercial off-the-shelf stepper motors [99], such as those used to drive small masses or gears in wristwatches. Integration of our large area metasurface cubic phase plates with these actuators would provide rapid and low-power (zero static power dissipation) focal length-tunable metalenses.

The developed tunable lens also demonstrated varifocal zoom imaging, adjusting magnification from 0.5x to 2x, with large (10's of centimeters) object and image distances. While we did not demonstrate a true parfocal zoom with our device, integration of two such Alvarez lenses [104] would allow for zoom imaging with stationary optical components and fixed object and image

positions. Integrating these two separate devices in a compact form factor would require modification of the tunable focal length range and therefore increasing the constant A in equation (8) to provide a design with shorter focal lengths.

The reported system demonstrates metalenses with a wide focal length tuning range and varifocal zoom imaging capability requiring minimal lateral actuation. Expanding on our previous work integrating two cubic metasurfaces [24], this system provides a tunable metalens with nearly 120 million nanoposts, more than 1300 times the number in our previous work, attributable to the stepper photolithography-compatible processing we developed with a versatile nanopost platform. This wide tuning range and varifocal zoom capability could find applications in microscopy, planar cameras, mixed reality, and light detection and ranging (LIDAR). The demonstrated metalens provides a pathway for metasurfaces to become a viable commercial technology, leveraging existing mass manufacturing processes and commercial off-the-shelf electronics to reduce the mass and volume of optical systems while retaining sufficient imaging quality and providing a low-power tuning mechanism.

Table 1. Comparison between different existing mechanically tunable metalens systems.

| Reference | Actuation Mechanism | Focal Length Change (cm) | Optical Power Change ($m^{-1}$) | Wavelength (nm) | Polarization |
|---|---|---|---|---|---|
| Ee et al. [90] | Stretching | $1 \times 10^{-2}$ | 2667 | 633 | Circular |
| Kamali et al. [91] | Stretching | $8 \times 10^{-2}$ | 952 | 915 | Insensitive |
| She et al. [92] | Stretching (electrical control) | 1.5 | 5 | 1550 | Insensitive |
| Arbabi et al. [94] | MEMS | $6.4 \times 10^{-3}$ | 180 | 915 | Insensitive |
| Zhan et al. [24] | Alvarez | 0.25 | 1600 | 633 | Insensitive |
| This work | Alvarez | 6.62 | 21 | 1550 | Insensitive |
| This work | Alvarez | 32.4 | 9 | 633 | Insensitive |

## 4.5 MATERIALS AND METHODS

### 4.5.1 *Simulation and Design*

The silicon nitride nanoposts were simulated using the Stanford S4 rigorous coupled-wave analysis (RCWA) package **[56]**. The validity of the unit cell approximation was evaluated by calculating the transmission amplitude and phase as a function of both diameter and lattice constant. For our 1550 nm simulation, we set the refractive indices of silicon and silicon nitride to 3.476 and 1.996 respectively. For our 633 nm simulation, we set the refractive indices of silicon dioxide and silicon nitride to 1.457 and 2.039 respectively. Subsequent metasurface designs were evaluated as complex amplitude masks based on the RCWA data and simulated by evaluating the Rayleigh-Sommerfeld diffraction integral by means of an angular spectrum propagator.

### 4.5.2 *Fabrication*

We used a dictionary of 6 fixed nanopost designs to make a hierarchy of cell references when generating our metasurfaces' layout file to substantially cut the required memory. Our process began with either a 100 mm silicon or quartz wafer, depending on whether the infrared or visible lens design was being fabricated. Our reticle was fabricated by Toppan Photomasks, Inc. and we transferred our pattern onto a film of AZ Mir 701 11 cps spun on top of a 2 μm PECVD silicon nitride layer using a 5x reduction stepper lithography system (Canon FPA-3000 i4). After development in AZ 300, we evaporated and then lifted off a 150 nm layer of aluminum to form a hard mask. We then etched the exposed nitride layer using a CHF3 and SF6 chemistry using an inductively-coupled plasma etcher system. We removed the remaining aluminum by etching in AD-10 photoresist developer. To capture the scanning electron micrographs, we sputtered an 8 nm

Au/Pd film as a charge dissipation layer, which was subsequently removed using type TFA gold etchant.

### 4.5.3 *Focal Length Measurement*

To measure the focal length of our 1550 nm metalens, we imaged the focal plane of the tunable metalens with a custom microscope positioned on a motion-controlled stage. We illuminated the whole aperture of the lens by passing a fiber-coupled and collimated 1550 nm SLD through a beam expander and adjusted the displacement of each plate by means of separate translation stages, projecting the microscope image of the focal plane onto an InGaAs camera [Figure 4.6(a)]. To characterize the focal length of the 633 nm lens, we illuminated the device with a HeNe laser passed through a beam expander, actuated the plates with micrometer translations stages, and measured the focal length with a meterstick [Figure 4.6(b)].

### 4.5.4 *Imaging with the Metalens*

To image with our device, we illuminated our test patterns with a 625 nm LED, placed the tunable lens in the optical path at the fixed object distance, and tuned the focal length with translation stages to project the image directly onto a CCD camera [Figure 4.7]. To zoom, we tuned the focal length of our metalens and shifted the CCD camera to the image plane. We imaged both by illuminating patterns in transmission and by scattering light off printed object patterns.

### 4.5.5 *Efficiency Measurements*

To measure the focusing efficiency of the lenses, we took the ratio of the optical power measured with a power meter (Newport Model 843-R) at the focal plane to that measured near the surface of the lens after transmission. In the case of the 633 nm efficiency measurement with the quartz substrate design, due to the super-wavelength lattice constant and higher diffraction orders which

we could not capture with our power meter, we defined our focusing efficiency as the ratio of the focal plane power to that which passes through two glass plates with quartz substrates mounted on each with the same orientation and separation distance as our Alvarez lens setup. In using these glass plates and quartz substrates without any nitride patterning, this provides an underestimate of the focusing efficiency as the patterned nitride layer would induce further reflections and scattering, reducing the total optical power transmitted through the lens surface. The zeroth order beam efficiency of the metalens is defined as the ratio of the focal plane power to that measured passing through the metalens surface itself with the higher diffraction orders not being captured by the power meter.

### 4.5.6 *Characterization of lenses and vortex beam generators based on the silicon nitride nanopost platform*

In addition to the designed metasurface Alvarez lenses of the main text, to further demonstrate the versatility of our nanopost design and fabrication process, our reticle also included several static singlet and vortex beam-generating metalenses for 1550 nm operation. Figure 4.5 summarizes the data collected in characterizing these devices, demonstrating successful focusing at the design focal length [Figure 4.5(a)-(b)] and orbital angular momentum generation for different values of topological charge [Figure 4.5(c)]. Our designed 2 mm static focal length lens exhibited close to diffraction-limited performance with a spot size of 3.94 μm, near the diffraction-limited value of 3.2 μm. The success of these devices verified the behavior and fabrication of the designed dielectric scatterers using our stepper lithography-based platform.

### 4.5.7 *Setup for measuring the focal length of the tunable metalens system*

To measure the focal length of our metalens system, we had to illuminate our device with light passed through a beam expander (Thorlabs BE10M-A) to illuminate the full aperture of the metalens. In the case of the infrared design, we used a microscope on a motioned-controlled stage to image the focal plane of the metalens system (Figure 4.6A). This microscope comprised an objective lens (Nikon Plan Fluor 20x/0.50, DIC M, ∞/0.17, WD 2.1), tube lens (Thorlabs ITL200), and camera (Xenics Bobcat-1.7-320). By laterally actuating the metasurface plates by means of translation stages, the focal length of the system would shift and we could translate the microscope until it was in focus and use the displacement to calculate the focal length. For the visible design, with the larger focal range supported by our device, it was beyond the range of our motion controlled-stage and microscope, so we used a reflective screen and meterstick to measure the focal length (Figure 4.6B). For the infrared design, we used a 1550 nm SLD (Thorlabs S5FC1005P) and for the visible design we used a HeNe laser as our illumination sources.

### 4.5.8 *Setup for imaging in transmission and scattering modes*

To image patterns with our metalens system, we illuminated objects in transmission (Figure 4.7A) and by scattering light off printed object patterns with off-axis illumination (Figure 4.7B) using a 625 nm LED (Thorlabs M625F2). Without additional optical elements in the path, we adjust the focal length of our metalens with translation stages to project an image of the object pattern directly onto a camera (AmScope MU300).

### 4.5.9 *Layout file generation algorithm*

In our algorithm, we use a dictionary data structure containing 6 unique nanopost radii as keys, each of which maps to a unique 32-sided regular polygon cell which approximates a circle. The 6

possible key-value pairings correspond to 6 possible discrete phase shifts in the 0 to 2π range to reduce the required memory, as opposed to utilizing a continuous spectrum of diameters. In generating the file, we iterate through a list of diameters and positions describing our layout and instantiate the appropriate cell reference for each nanopost by accessing our dictionary with the nanopost's radius key, as opposed to making a separate cell for each nanopost. In the case of our metasurface Alvarez lens metasurface plates, we cut the memory from 372 GB to 4.4 GB as a GDSII, and to only 140 MB as an OASIS file (more than a 2600x reduction).

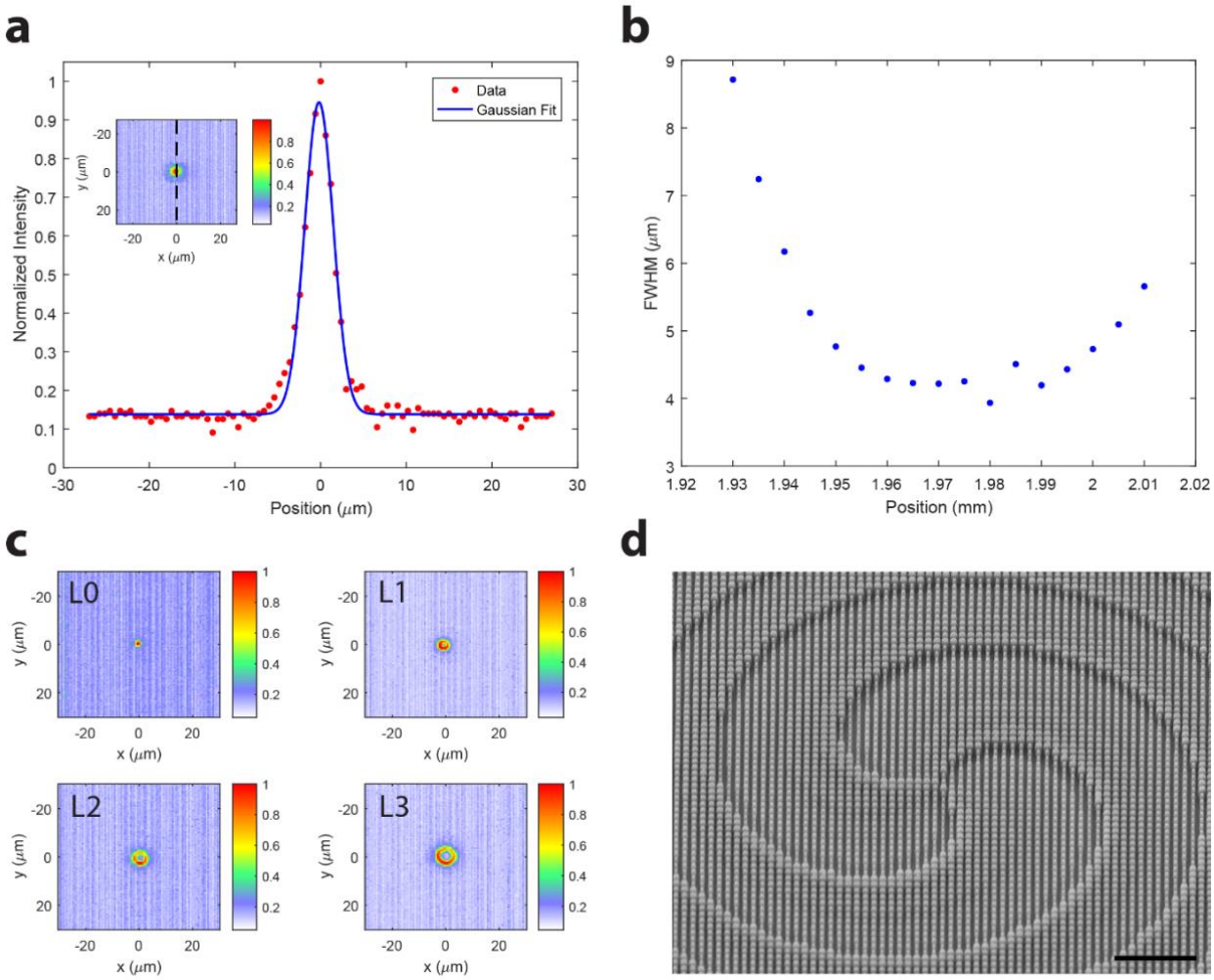


Figure 4.5. Characterization of static metasurface aspherical and vortex beam-generating lenses for 1550 nm wavelength. (a) Cross section of a measured intensity profile at the focal plane of a designed static 2 mm focal length lens with 1 mm diameter using our nanoposts. The inset shows the 2D profile where the black dashed line indicates the position of the cross section. (b) Beam spot size in terms of full width at half maximum as a function of position along the optical axis of our lens from (a). (c) Measured cross sections at the focal plane of vortex beam-generating lenses, showing doughnut-shaped beams with different labelled values of topological charge. (d) 45° incident scanning electron micrograph of the L3 vortex beam lens. Scale bar 10 μm.

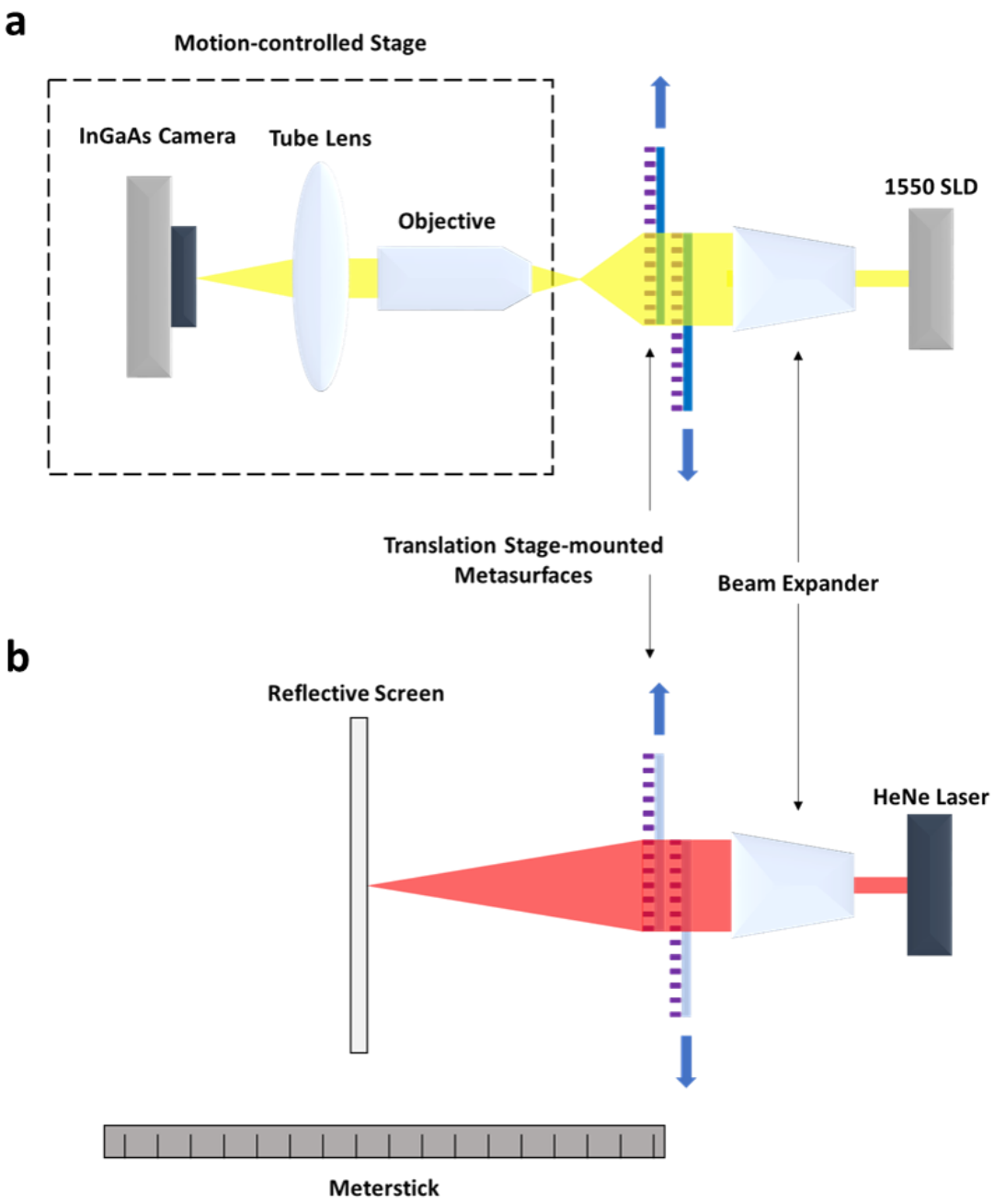


Figure 4.6. Experimental setups for measuring the focal length of our tunable system. (a) Setup for measuring the focal length of our infrared tunable metalens. (b) Schematic of experimental setup for measuring the focal length of our visible wavelength tunable lens design.

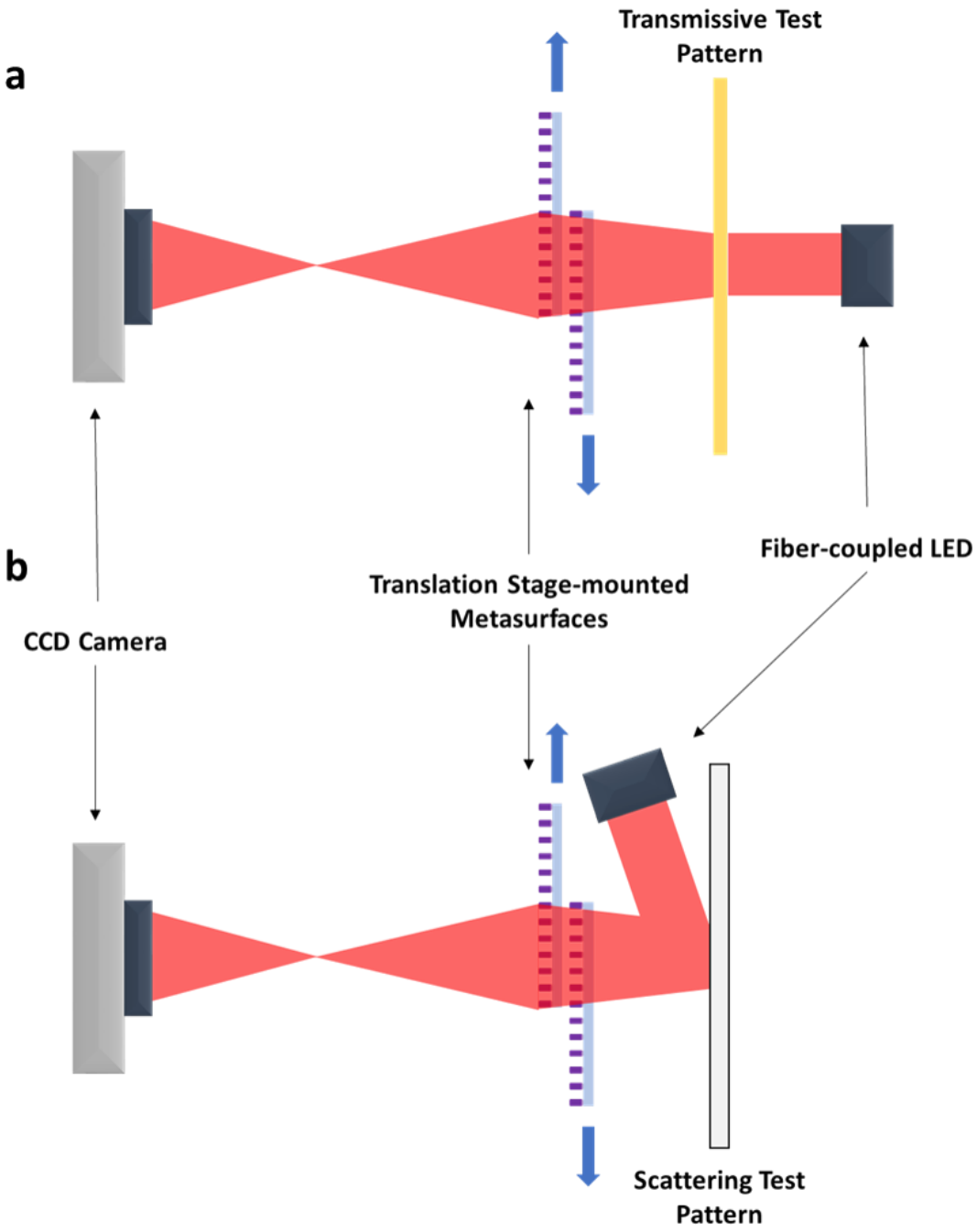


Figure 4.7. Experimental setup for imaging experiments. We imaged object patterns in transmission (a) and by scattering light off objects (b) by projecting the image directly onto a camera without any additional magnification optics.

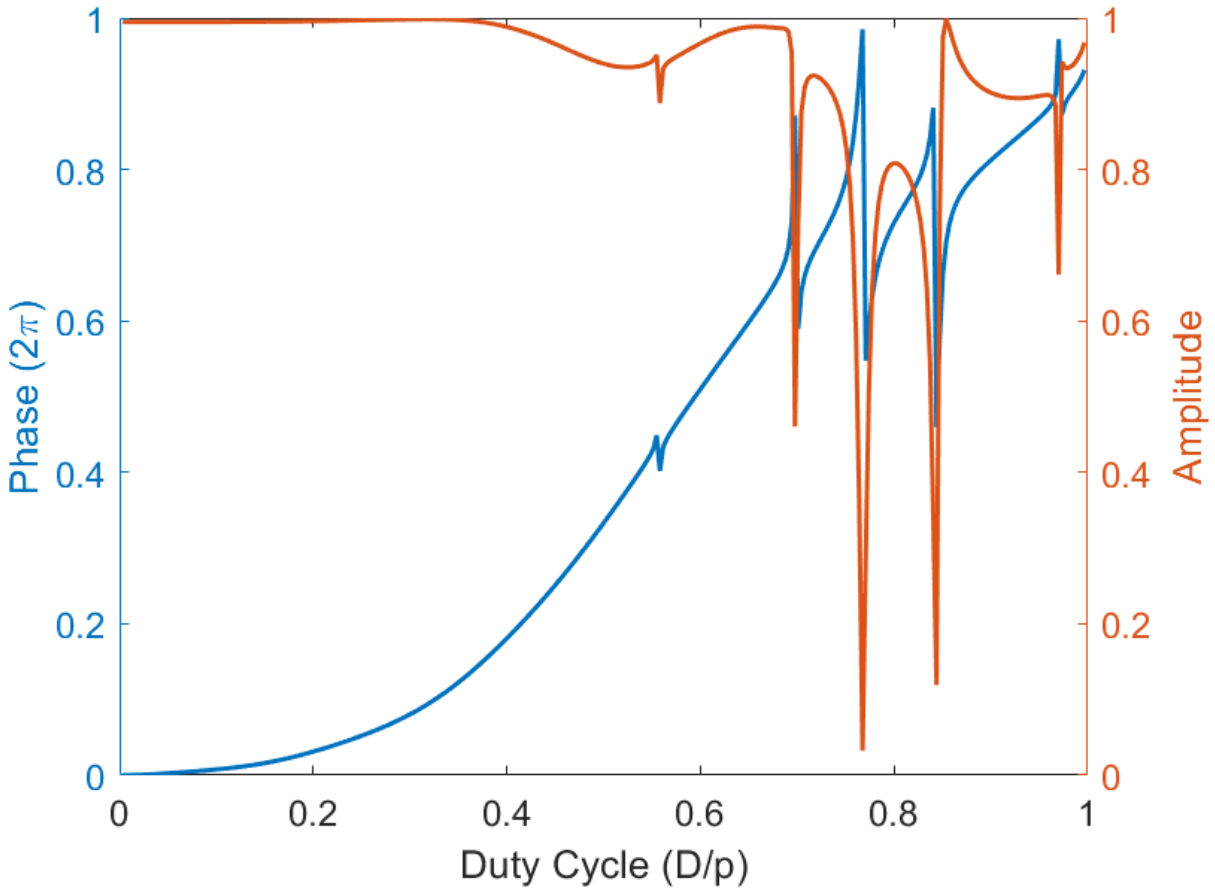


Figure 4.8. DUV lithography-compatible silicon nitride nanopost design simulation. The simulated transmission coefficient is shown as a function of duty cycle. The nanopost is of thickness 633 nm and lattice constant 443 nm. By varying the post diameter between 125 nm and 400 nm, high efficiency metasurfaces can be realized.

# Chapter 5. SIMULTANEOUS VARIFOCAL AND ACHROMATIC METALENSES

*Reproduced with permission from* [105], *S. Colburn and A. Majumdar, "Simultaneous Achromatic and Varifocal Imaging with Quartic Metasurfaces in the Visible," ACS Photonics 7, 120–127 (2020). Copyright 2019. American Chemical Society.*

## 5.1 INTRODUCTION

Imaging systems today boast high-quality achromatic imaging with optical zoom. These systems, however, often entail bulky elements incapable of meeting the demand for compact, next-generation sensors and cameras. Computational imaging reduces this complexity by replacing sophisticated optics with simple elements and leveraging computation to transfer part of the imaging process into software [1–3]. This has enabled high-quality imaging using simple lenses combined with post-processing [4].

Recently, computational imaging and metasurfaces were used together to perform full-color imaging [25], as detailed earlier in this thesis. By introducing a cubic term to a metalens' phase profile, a spectrally invariant point spread function (PSF) was designed, enabling deconvolution with a single filter for achromatic imaging. At the cost of increased power consumption and latency from post-capture computation, this wavefront coding [27–29] technique circumvents the area scaling limitations of dispersion-engineered metalenses. These elements, like dispersion-engineered metalenses, however, are limited compared to state-of-the-art cameras in their inability to perform an optical zoom, which requires a varifocal lens. While various techniques exist for tuning metalenses, such as using MEMS to adjust the gap between two metalenses [94] or stretching metasurfaces on a flexible substrate [89–92], these approaches have not yet been demonstrated simultaneously with achromatic focusing. Though MEMS could

feasibly support actuation of dispersion-engineered metalenses, it is limited to small devices to prevent dielectric breakdown, and while dispersion-engineered metalenses can be stretched, it is unknown whether the scatterers can maintain their dispersion as the distance between the scatterers changes. Recently, focal length tuning was also achieved with an achromatic response in the 483-620 nm range, but this required a continuous change of input polarization state [106].

To simultaneously achieve achromatic operation and an adjustable focal length, in this chapter, we employ lateral actuation of a pair of wavefront-coded metasurfaces. Our design comprises two quartic metasurfaces that together produce a continuously tunable extended depth of focus (EDOF) lens, exhibiting a near spectrally invariant PSF at visible wavelengths for all focal lengths. In conjunction with a regularized post-capture deconvolution algorithm, we demonstrate white light imaging of colored patterns over a 5x zoom range. We report, to the best of our knowledge, the first polarization-independent metasurface system demonstrating simultaneous achromatic and varifocal zoom imaging.

## 5.2 RESULTS

### 5.2.1 *Design*

Our design is inspired by a traditional Alvarez lens [24,26,98] as described earlier in this thesis, which comprises two cubic phase elements positioned in series along the optical axis. When the elements in an Alvarez lens are in alignment, the net phase delay is zero, as their spatial phase shifts exactly cancel each other according to

$$\theta_1(x,y) = -\theta_2(x,y) = A\left(\frac{1}{3}x^3 + xy^2\right), \quad (9)$$

where $A$ is a constant and $(x,y)$ gives the in-plane position coordinates. On the other hand, when the two elements are laterally shifted in opposite directions, the superposition of their phase

profiles yields a quadratic function. The focus of the quadratic function depends on the relative displacement, yielding a varifocal lens with a phase function

$$\varphi_{Alvarez}(x,y) = \theta_1(x+d,y) + \theta_2(x-d,y) = 2Ad(x^2+y^2) + \frac{2}{3}d^3, \quad (10)$$

and a focal length

$$f(d) = \frac{\pi}{2\lambda Ad}, \quad (11)$$

where $d$ is the lateral displacement and λ is the wavelength. If the phase elements are implemented as metasurfaces, however, the system would exhibit a significant chromatic focal shift, typical for diffractive lenses. Its point spread function (PSF) is strongly wavelength-dependent and yields zeros for large spatial frequency bands in the corresponding modulation transfer functions [27,29] (MTFs) for wavelengths deviating from the designed value. As was recently demonstrated, however, the addition of a cubic term to a metalens' phase profile provides an EDOF that yields a PSF that is nearly insensitive to longitudinal chromatic focal shift [25]. Instead of focusing to a point like a metalens, such an element produces a focused Airy beam and an asymmetric PSF that blurs images. Via a monochromatic PSF calibration measurement, however, this blur can be negated via deconvolution across the visible spectrum. We emphasize that such a deconvolution approach cannot be applied for the case of a singlet metalens under white light illumination, as the wavelength dependence of the PSF and the large increase in PSF size results in a loss of higher spatial frequency information that deconvolution cannot recover [25]. Modifying equation (10) to include a cubic term, neglecting the $d^3$ constant phase, and substituting the focal length from equation (11), the phase

$$\varphi_{EDOF} = \frac{\pi(x^2+y^2)}{\lambda f} + \frac{\alpha}{L^3}(x^3+y^3), \quad (12)$$

simultaneously imparts the profile for a focusing lens and extends its depth of focus. Here, $L$ denotes half the aperture width and $\alpha$ is the cubic phase strength (i.e., the number of 2π cycles

from the cubic phase term when traversing a path from the origin to the aperture edge in the $x$ direction). Expressing $\varphi_{EDOF}$ as a superposition of two oppositely signed and laterally displaced phase functions,

$$\varphi_{EDOF} = \theta_{plate}(x + d,\ y) - \theta_{plate}(x - d,\ y), \quad (13)$$

we can relate the derivative of $\theta_{plate}$ to this difference and $\varphi_{EDOF}$ via the two-sided definition of the derivative as below

$$\frac{\partial \theta_{plate}}{\partial x} = \lim_{d \to 0} \frac{\theta_{plate}(x+d, y) - \theta_{plate}(x-d, y)}{2d} = \lim_{d \to 0} \frac{\varphi_{EDOF}}{2d}, \quad (14)$$

Making the substitution $\frac{\alpha}{L^3} = Bd$, where $B$ is a constant, we can find

$$\theta_{plate}(x,\ y) = A\left(\frac{1}{3}x^3 + xy^2\right) + B\left(\frac{1}{8}x^4 + \frac{1}{2}xy^3\right), \quad (15)$$

When $B = 0$, $\theta_{plate} = \theta_1$ and the superposition of the two laterally displaced plates behaves exactly as an Alvarez lens; however, for nonzero B, $\theta_{plate}$ becomes a quartic phase polynomial in $x$. Continuous lateral displacement of these conjugate plates yields a tunable focal length EDOF lens with a phase distribution given by equation (12). Instead of focusing to a point, this system produces a tunable focused accelerating beam that generates spectrally invariant point spread functions that enable wavelength-uniform deconvolution [25] for each focal length. We refer to this device as an EDOF Alvarez metalens henceforth. While tunable cubic phase masks via conjugate quartic phase plates have been theoretically studied before [107–109], our design is the first to our knowledge that combines the functionality of both tunable focusing and tunable wavefront coding with only two elements.

To implement the phase profile of equation (15) and its inverse with metasurfaces, we choose silicon nitride as the material for our scatterers due to its broad transparency window and CMOS compatibility [49,50,52]. The scatterers are polarization-insensitive cylindrical nanoposts

arranged in a square lattice on a quartz substrate (Figure 5.1A-B). The phase shift mechanism of these nanoposts arises from an ensemble of oscillating modes within the nanoposts that couple amongst themselves at the top and bottom interfaces of the post [13,53,55]. By adjusting the diameter of the nanoposts, the modal composition varies, modifying the transmission coefficient. At a nominal wavelength of 530 nm (green light), we simulate the transmission coefficient of a periodic array of these nanoposts with a thickness $t = 600\ nm$ and period $p = 350\ nm$ (Figure 5.1C) (see Figure 5.7 and 5.8 for simulations at other wavelengths and justification of the local phase approximation respectively). In sweeping the diameter of the nanoposts, the transmission phase exhibits a nearly $2\pi$ range with amplitude close to unity except for several resonances that are avoided when selecting diameters for phase shifting elements.

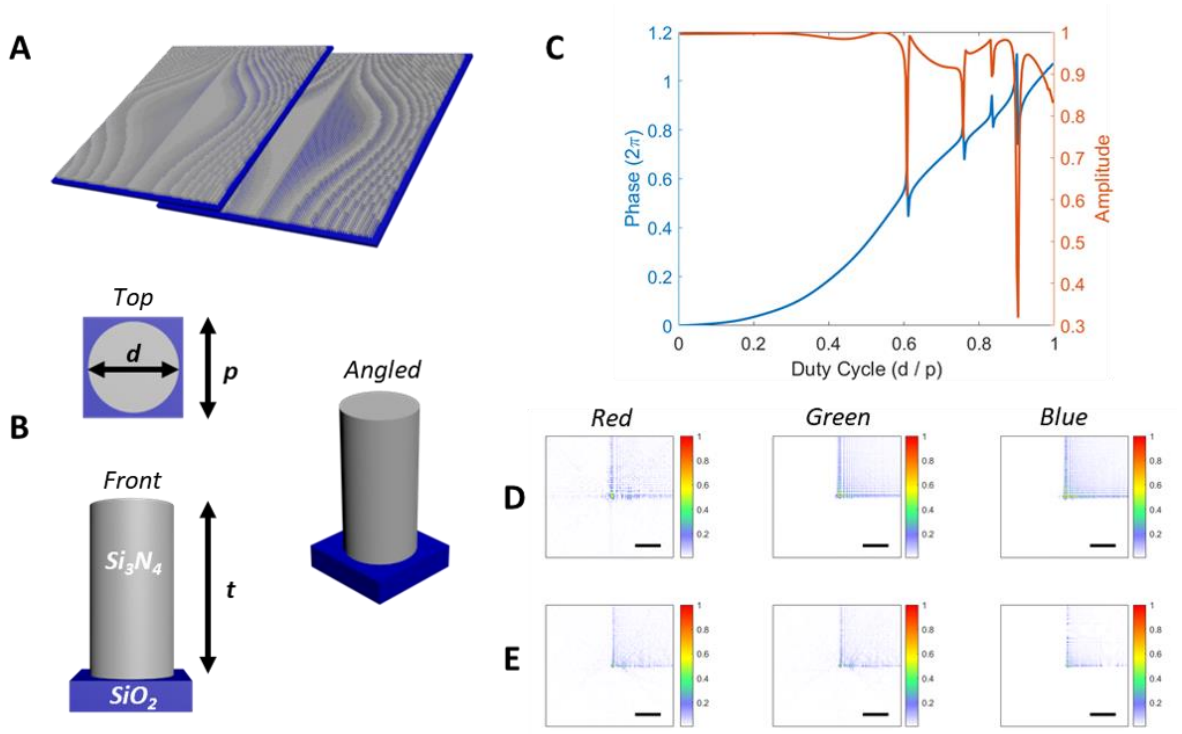


Figure 5.1 Metasurface Design and Simulation. Schematics are shown of the Alvarez EDOF metalens system (A) and the nanoposts that comprise the metasurfaces (B). (C) The simulated amplitude and phase of the transmission coefficient of a periodic array of the designed nanoposts. Simulated point spread functions are shown for lateral displacements of 50 μm (D) and 100 μm (E) for the designed system at image planes of 3 mm and 1.5 mm respectively. Scale bar 80 μm.

To change the focal length from 6 mm to 1.2 mm by tuning $d$ from 25 μm to 125 μm at 530 nm wavelength, we use a value of $A = 1.98 \times 10^{13}\ m^{-3}$. A lower value of $A$ increases the focal length but reduces the numerical aperture for a fixed metasurface size. The value of $B$ depends on the desired operating wavelength range, which here spans from blue (455 nm) to red (625 nm) light. Higher values of $B$ increase the depth of focus at the cost of reducing the signal-to-noise-ratio (SNR). As the range of chromatic focal shift increases with a wider optical bandwidth, however, the focal depth must be extended to ensure a spectrally invariant PSF over the whole wavelength range. For our wavelength range, $B = 7.59 \times 10^{16}\ m^{-4}$ satisfies this requirement (Figure 5.16 shows the corresponding nanopost radii distributions for the resulting metasurfaces). With an aperture of 1 mm, Figure 5.1D compares the simulated PSFs of our system under incoherent red, green, and blue illumination. We use a fixed displacement of $d = 50\ \mu m$ at an image plane of 3 mm, demonstrating highly similar responses for each wavelength. Figure 5.1E examines PSFs of the system at the same three wavelengths but with a displacement of $d = 100\ \mu m$, producing near-invariant PSFs at a 1.5 mm image plane. The difference in PSFs between Figure 5.1D and 1E is intended as the focal length and cubic phase strength change with $d$. The PSFs, however, remain nearly wavelength-invariant for a fixed displacement, validating the behavior of the Alvarez EDOF metalens. To quantify the spectral bandwidth of our imaging system, we perform memory effect correlation calculations [110] as a function of input wavelength for our PSFs and estimate that our PSF similarity ranges from ~440-640 nm (Figure 5.14). Similarly, we assess the input angle dependence of our PSFs to estimate a field of view [111] of ~36° for our system (Figure 5.13). In our calculations, we assume an incoherent imaging model in which the system is linear in intensity and the intensity PSF is the modulus squared of the coherent PSF determined via angular spectrum propagation. While a coherent imaging system with such a

device is theoretically possible, in practice it would be challenging due to speckle and a coherent source would require detection not only of intensity but also phase information for deconvolution, which is significantly more challenging at optical frequencies.

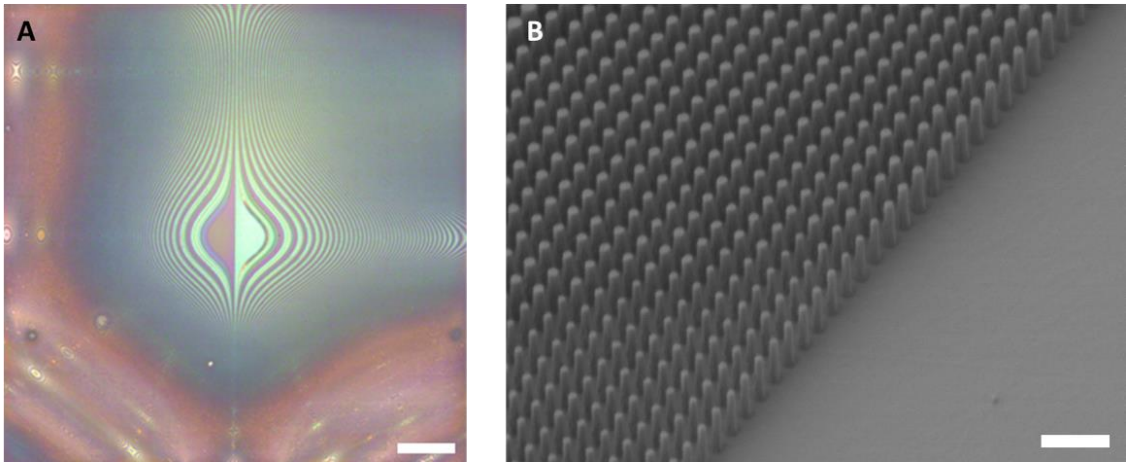


Figure 5.2 Fabrication. (A) An optical image at normal incidence of one of the Alvarez EDOF metalens' plates is shown. Scale bar 0.125 mm. (B) A scanning electron micrograph captured at 45° depicting the fabricated silicon nitride nanoposts. Scale bar 1 μm.

### 5.2.2 *Experimental Verification*

We fabricated the metasurfaces and an optical image and a scanning electron micrograph of one of the completed structures is shown in Figure 5.2A and 2B respectively. We experimentally verified the varifocal behavior of the metalens by measuring its response under 530 nm illumination (see Figure 5.11 for a schematic of the experimental setup). Figure 5.3 depicts the intensity along the $x = 0$ plane after the metalens for values of $d$ ranging from 25 μm to 125 μm. For each tuning state, the focal spot exhibits an extended depth, and the z-position of maximum intensity for each state agrees well with the theoretical focal length of a conventional Alvarez metalens, i.e., for $B = 0$ (Figure 5.3 inset). As both the quadratic and cubic terms in equation (12) are proportional to $d$, the depth of focus also increases with increasing focal length.

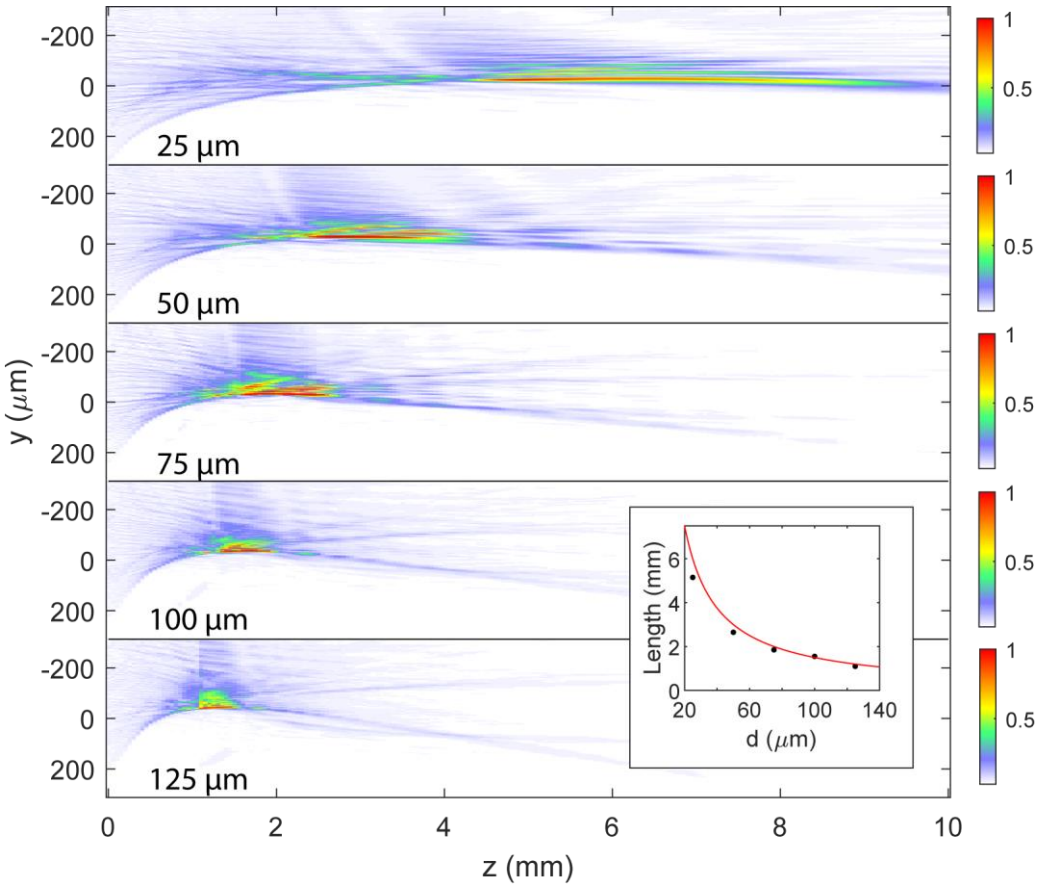


Figure 5.3. Varifocal Behavior. Normalized measured intensity cross sections along the optical axis of the Alvarez EDOF metalens are depicted for different values of lateral displacement ranging from 25 µm to 125 µm going from the top to the bottom. The inset depicts the z distance to the point of maximum measured intensity (black dots) compared to the theoretical focal length of an Alvarez lens without an EDOF (red curve).

We next examined the chromatic focal shift of the device by illuminating with blue and red light and capturing intensity cross sections in the vicinity of the desired focal plane. Figure 5.4A (Figure 5.4B) shows the intensity for the case of a 100 μm (50 μm) lateral displacement about the 1.5 mm (3 mm) plane. While the longitudinal shift of the extended focal spot is significant over the wavelength range measured, for all three wavelengths the spatial intensity distributions at the desired focal plane (indicated by the dashed lines) are quite similar, elucidating the mechanism of generating spectrally invariant PSFs with an EDOF Alvarez metalens. The tested device also achieved an average diffraction efficiency of 37% at the three test wavelengths over the 25 μm to 125 μm actuation range (Figure 5.10).

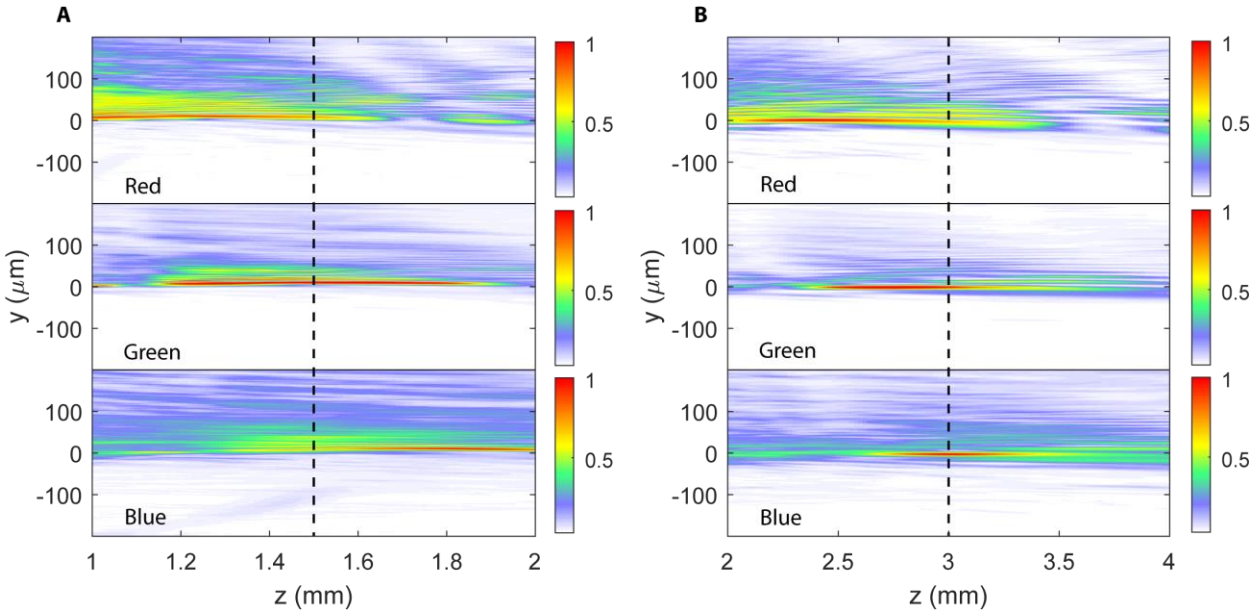


Figure 5.4. Chromatic Focal Shift. Normalized measured intensity cross sections are shown for lateral displacements of 100 μm (A) and 50 μm (B) about their respective focal planes for red (625 nm), green (530 nm), and blue (455 nm) illumination cases.

To verify the spectral invariance of the system, we measured the PSFs (Figure 5.5) for different values of $d$ and compared to those of a static singlet metalens with a phase given by

$$\varphi_{singlet}(x, y) = \frac{2\pi}{\lambda}\left(f - \sqrt{x^2 + y^2 + f^2}\right), \quad (16)$$

We fabricated two singlets with 1 mm apertures, 1.5 mm and 3 mm focal lengths, for green light (wavelength 530 nm) and their PSFs are shown in Figure 5.5A-C and Figure 5.5H-J respectively. While these elements produce a tightly focused PSF for the green design wavelength, they vary drastically at other wavelengths, generating large diffraction blurs under red and blue illumination. For the case of the Alvarez EDOF metalens, however, its PSF remains much more similar under these different illumination wavelengths as shown in Figure 5.5D-F (5K-M) for a displacement of 100 μm (50 μm) measured at the same focal plane position as the 1.5 mm (3 mm) singlet. MTFs corresponding to these PSFs are shown in Figure 5.9, allowing us to estimate the experimental resolution of the system in terms of the 10% point for the MTF averaged over wavelength, giving 11 cycles/mm and 9.6 cycles/mm for the 3 mm and 1.5 mm focal length states respectively.

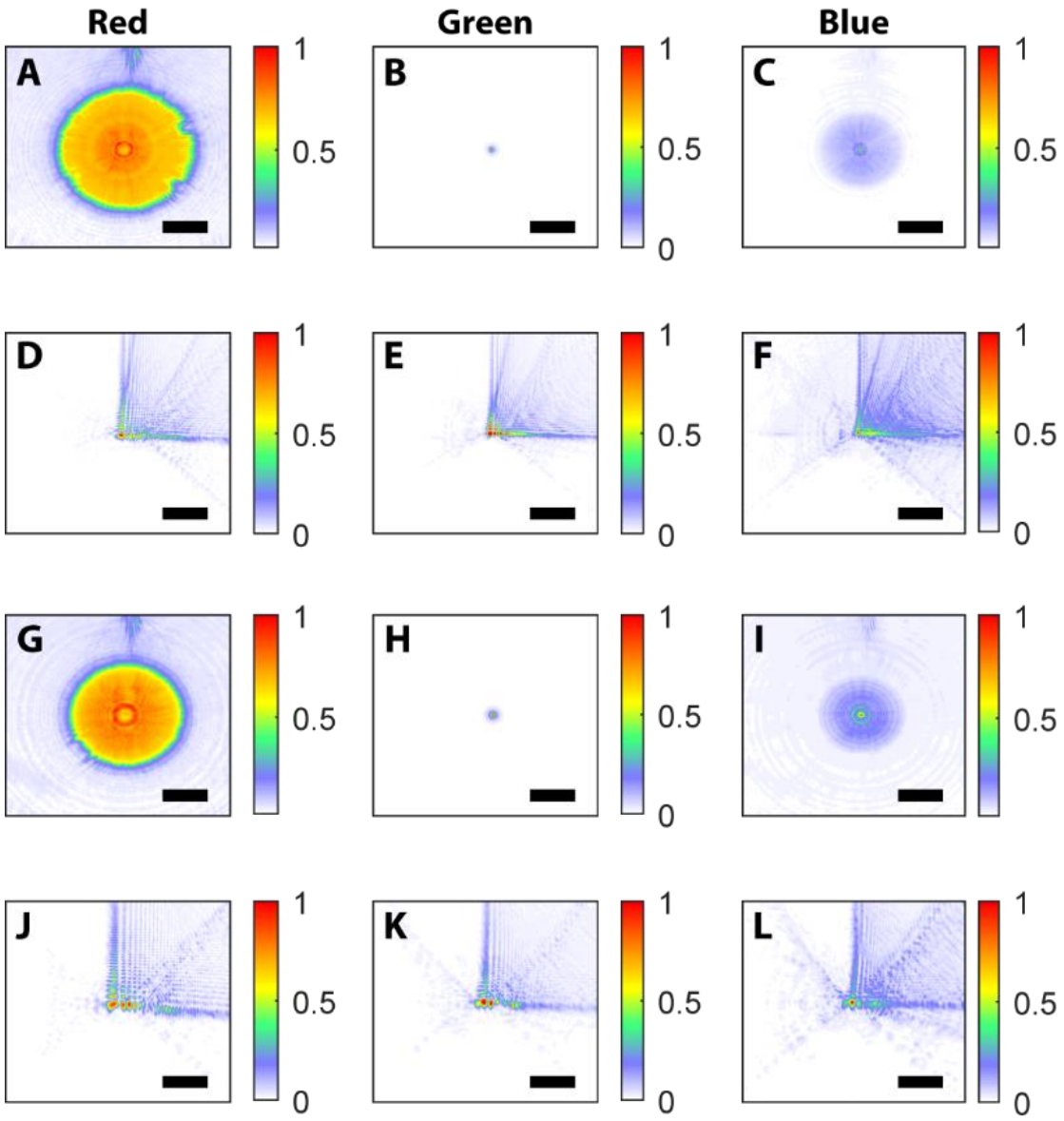


Figure 5.5. Experimental Point Spread Functions. PSFs for the 1.5 mm singlet are shown (A-C) compared to those at an equivalent focal length for the Alvarez EDOF metalens with a lateral displacement of 100 µm (D-F). In (G-I) equivalent PSFs are depicted for the 3 mm singlet, while (J-L) show the corresponding Alvarez EDOF metalens' PSFs under 50 µm displacement at a 3 mm image plane. Scale bar 78.3 µm.

### 5.2.3 *Imaging*

Leveraging the wavelength insensitivity of the Alvarez EDOF metalens' PSF, we performed imaging experiments (see Figure 5.12 for a schematic of the experimental setup) by capturing and deconvolving images of object patterns under white light illumination. Our image model can be compactly summarized via the equation $y = Kx + n$, where $y$ denotes the vectorized blurry captured image, $K$ is a matrix form of the measured PSF, $n$ is noise, and $x$ is the latent image that we want to reconstruct. Various deconvolution algorithms have been employed to solve this problem in computational imaging systems; here we elect to solve for $x$ using a regularized approach based on the total variation regularizer so that we can easily balance the tradeoff between deblurring and denoising, described via

$$x = argmin_x\, TV(x) + \frac{\mu}{2}\|Kx - y\|_2^2, \quad (17)$$

In this equation, $TV$ denotes the total variation regularizer and μ is a hyperparameter that we can tune to adjust the weight assigned to deblurring or denoising [112]. In solving for $x$, we assume the PSF is spatially invariant, which reduces the complexity of equation (17), allowing us to use FFT operations rather than constructing the full $N \times N$ kernel matrix.

Applying this framework to our system, we imaged and deconvolved a set of three different object patterns with different underlying spatial features and color content (Figure 5.6) at five different magnification levels by tuning the lateral displacement of the metasurfaces. While a separate PSF is required for deconvolution in each tuning state, their near wavelength-invariant behavior enables us to use the same PSF for all colors. We also captured images of the same objects with our 1.5 mm singlet metalens for comparison. While much of the color content in the ground truth objects is smeared out by the large diffraction blurs of the singlet metalens, different colors are far more distinct for the deconvolved EDOF metalens images. Prior to deconvolution, the

captured EDOF metalens' images are blurry for all colors, but the near spectrally invariant nature of the blur is the enabling condition for deconvolution with a single filter. Furthermore, while the singlet metalens is capable of imaging at only one magnification because of its static nature, in tuning the displacement of the Alvarez EDOF metalens from 25 $\mu m$ to 125 $\mu m$ and shifting the image plane, the magnification is seamlessly swept over a 5x zoom range.

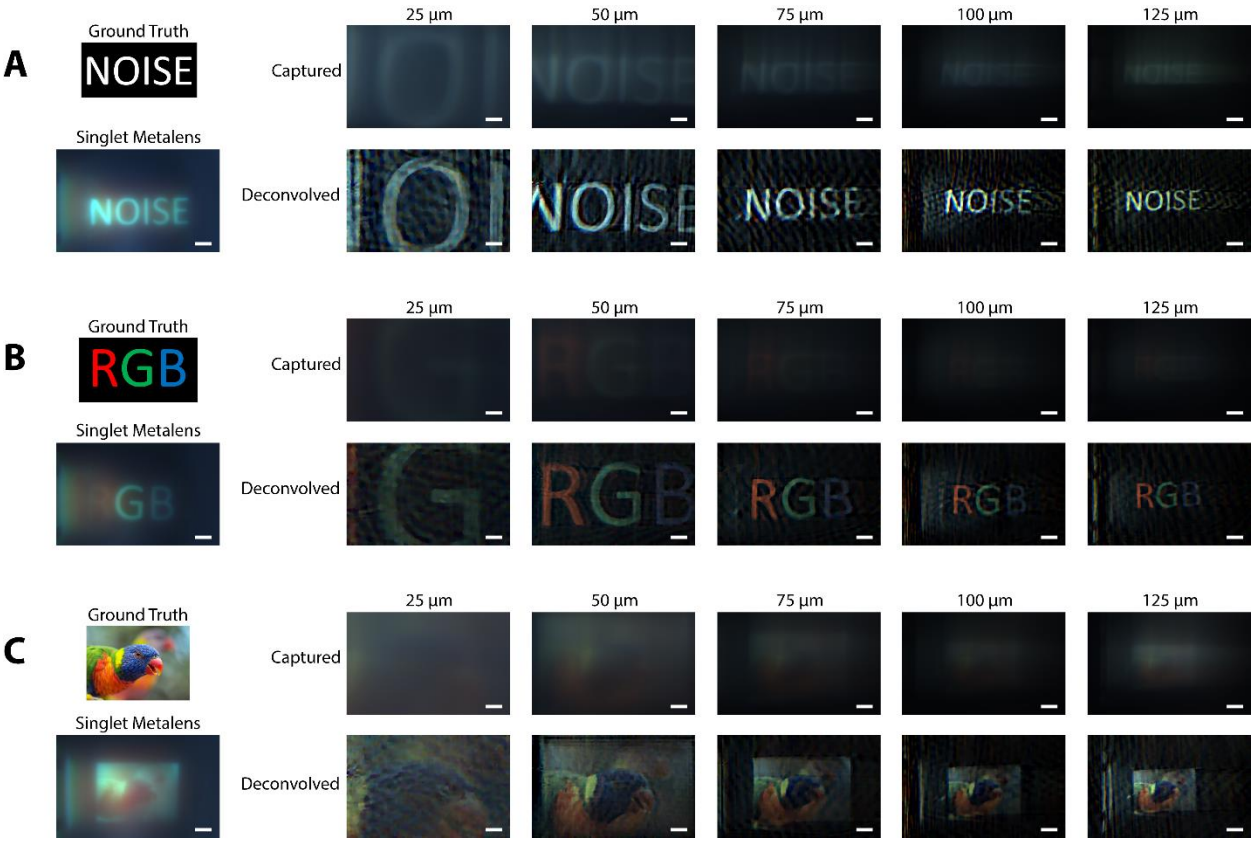


Figure 5.6. White Light Imaging. Images are shown depicting the ground truth objects that were imaged, including "NOISE" text (A), "RGB" text (B), and a colorful bird (C). Also shown are images captured using the 1.5 mm singlet metalens under white light for comparison, and the images from the Alvarez EDOF metalens before and after deconvolution for five different lateral displacements ranging from 25 µm to 125 µm from left to right. Scale bar 62 µm in all images.

## 5.3 DISCUSSION

Our Alvarez EDOF metalens system demonstrates a wide tunable focal length range (a 4.8 mm or 400% change, $\frac{f_{max}-f_{min}}{f_{min}}$, or equivalently a 667-diopter change in optical power at 530 nm). This broad tuning range arises from the inverse proportionality of focal length to lateral displacement in equation (11). Simultaneously, the depth of focus of the lens is also tuned as the focal length shifts. This is not achieved by the inherent extension of the depth of focus that naturally comes with longer focal lengths, but by directly modifying the cubic phase strength via lateral displacement of a pair of phase elements, the first experimental demonstration of such behavior [107–109] to the best of our knowledge. For proof of concept, the metasurfaces are currently actuated by hand using kinematic stages, but for practical applications electrical control can be realized. Depending on the scale of the metasurface elements, a vast array of different actuation mechanisms may be employed. For devices with apertures on the order of hundreds of microns, for example, MEMS actuators could feasibly translate the metasurfaces, whereas for centimeter-scale devices, for which the masses and actuation distances are greater, a combination of miniature gears and stepper motors could be used [99].

While the tuning of the PSF is accomplished fully via mechanical actuation of the two plates, the zoom imaging behavior is unlike that of alternative tunable metalenses as a post-capture deconvolution step is required to produce a focused image. This requirement arises from the simultaneous wavefront coding that distinguishes our design from alternative varifocal metalenses. In applications with monochromatic or narrowband illumination, the added computational cost from the deconvolution step would introduce extra power consumption and latency that existing varifocal metalenses can avoid. As such, existing metasurface zoom lenses that do not depend on post-processing software for image formation would outperform our system in monochromatic

applications. The added computation, however, extends the operating bandwidth and enables the system to image over a broad spectral range and not just with monochromatic light. As such, our system is well suited for imaging applications requiring a range of wavelengths and when additional power consumption and reduced SNR are tolerable.

Unlike metasurfaces optimized for operation at discrete wavelengths (e.g., at only red, green, and blue) [80], our system can produce in-focus images for intermediate colors such as yellow (Figure 5.6C). Compared to many of the existing broadband achromatic metasurface systems [45–47,83], our technique does not utilize specialized dispersion-engineered scatterers and as such does not have to contend with the area scaling limitations and polarization dependence. Furthermore, no other work exhibits a metasurface-based achromatic varifocal zoom. Our system, however, circumvents these challenges by sacrificing SNR to extend the depth of focus [28] and by adding post-processing software to the imaging pipeline. This adds power consumption to an imaging process that is conventionally passive and produces a latency that may hinder real-time operation when capturing video. Using a MATLAB implementation of the software on an ordinary personal laptop computer (Intel Core i7, 12 GB RAM), the deconvolution algorithm averaged 3.9 minutes per full-color 1936 × 1216 image. The deconvolution algorithm, however, could be hardware-accelerated by using field-programmable gate arrays (FPGAs) or adapted to run on state-of-the-art graphics processing units (GPUs) to enable real-time processing. Furthermore, in any application where real-time operation is unnecessary, all captured frames could be subsequently deconvolved offline. Alternative post-processing algorithms could also be used, including efficient and simple Wiener deconvolution, which averages 2.07 seconds per full-color image, representing a 113 × speedup, albeit at the cost of greater noise amplification and ringing artifacts in the absence of TV regularization (see Figure 5.15). Depending on the required magnification level,

these artifacts can become more pronounced but depending on the requirements of the system, the speedup offered may outweigh the costs.

While the deconvolved images from our device exhibit noise amplification, these features can be mitigated with improvements in design and noise calibration. The limited aperture of our metalens (1 mm) precludes a high photon count and constrains our imaging to low light levels, contributing to the noise. With a larger aperture and increased space-bandwidth product, however, the Alvarez EDOF metalens would be capable of imaging with higher fidelity [1]. Additionally, in this work we have not performed any sophisticated noise calibration beyond dark noise subtraction. By calibrating and calculating the Poisson and Gaussian noise components of the sensor [86], the deconvolution and denoising could be significantly improved.

## 5.4 CONCLUSION

In this chapter, we demonstrated the design, fabrication, and characterization of the first polarization-independent metasurface-based achromatic imaging system with varifocal zoom. We derived the phase functions for the metasurfaces in an Alvarez lens-like configuration that enable a varifocal lens with an extended depth of focus, and then experimentally demonstrated a 400% change in focal length with a nearly spectrally invariant PSF across the visible regime at each focal length. Leveraging our tunable focal length EDOF design, we imaged object patterns in full color over a 5x zoom range with significantly mitigated chromatic aberrations compared to conventional metalenses. While our captured images exhibit noise, we anticipate improvements in this via more advanced sensor calibration [86] and utilizing a wider aperture design [1]. With the demonstrated imaging and the ease in scaling our device to various sizes, our work may benefit a variety of

applications including planar cameras, microscopy, augmented reality systems, and autonomous navigation.

## 5.5 Materials and Methods

### 5.5.1 *Simulation*

We use rigorous coupled-wave analysis (RCWA) to simulate the amplitude and phase of the transmission coefficient of our nanoposts. The refractive index of Si3N4 (SiO2) was set to 2.077 (1.465), 2.056 (1.461), and 2.041 (1.457) for 455 nm, 530 nm, and 625 nm wavelengths respectively. We simulate the PSFs of our system by treating the metasurfaces in the design as complex amplitude masks, where each pixel's diameter maps to the corresponding amplitude and phase from the RCWA-simulated transmission coefficient. The light propagation to calculate the PSFs is modeled via the angular spectrum method. The modulus squared of the calculated field then yields the incoherent PSF.

### 5.5.2 *Fabrication*

In this work, a total of four separate metasurfaces (two singlets and two metasurfaces for the Alvarez EDOF metalens) were fabricated on separate samples. For each device, a 600 nm layer of silicon nitride was first deposited via PECVD on a quartz substrate followed by spin coating with ZEP-520A. An 8 nm Au/Pd charge dissipation layer was then sputtered followed by subsequent exposure with a JEOL JBX6300FS electron-beam lithography system. The Au/Pd layer was then removed with type TFA gold etchant and the samples were developed in amyl acetate. To form an etch mask, 50 nm of aluminum was evaporated and lifted off via sonication in methylene chloride,

acetone, and isopropyl alcohol. The samples were then dry etched using a $CHF_3$ and $SF_6$ chemistry and the aluminum was removed by immersion in AD-10 photoresist developer.

### 5.5.3 *Characterization*

To measure the intensity along the optical axis, we illuminated with a set of different wavelength LED sources and used a custom microscope positioned on a motion-controlled stage to image cross sections of the region after the metalens. The metasurfaces were actuated via separate translation stages to control the lateral displacement (Figure 5.11). The PSFs were measured by illuminating a pinhole in the far-field and measuring the focal plane intensity. Our diffraction efficiencies were calculated by taking the ratio of the intensity integrated within the aperture area of the device at the focal plane to that at the plane of the second metasurface in the optical path. To image, we illuminated objects on standard printer paper with a commercial camera panel light source (Figure 5.12) and we deconvolved the captured images using an open source library that solves the TV-regularized deconvolution problem using the Split Bregman method. We use a value of $\mu = 2.5 \times 10^4$ for our regularization parameter for all deconvolutions to balance denoising and deblurring.

## 5.6 TRANSMISSION COEFFICIENT CALCULATIONS AT MULTIPLE WAVELENGTHS

In addition to the nanoposts' operation at a nominal wavelength of green light, 530 nm (Figure 5.1C in the main text), we also examined their performance under blue (455 nm) and red (625 nm) illumination to enable calculation of PSFs at these wavelengths. Figure 5.7 shows the transmission coefficients for all three wavelengths, depicting near 2π phase ranges for each wavelength with resonances (primarily guided mode resonances), that are avoided to ensure high transmission amplitude nanoposts.

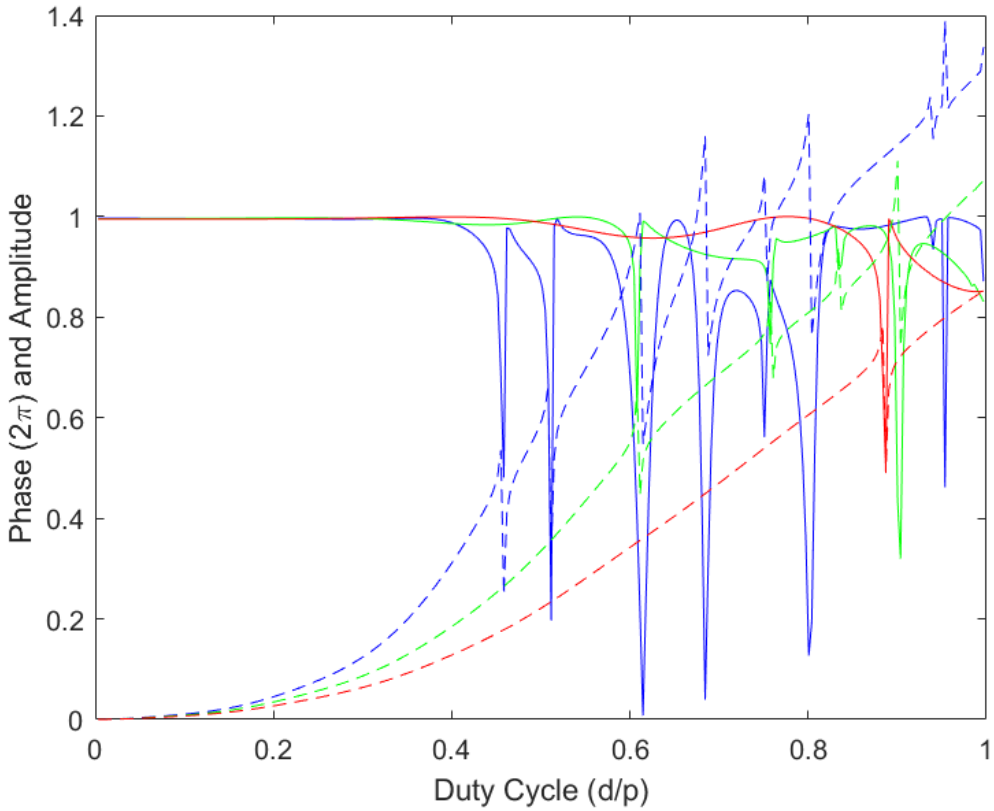


Figure 5.7. Multiwavelength transmission coefficient. The transmission phase (dashed lines) and amplitude (solid lines) simulated via RCWA are plotted for 625 nm (red), 530 nm (green), and 455 nm (blue) wavelengths as a function of duty cycle, where the lattice constant is fixed at 350 nm, corresponding to the design from Figure 5.1C.

## 5.7 JUSTIFICATION OF THE LOCAL PHASE APPROXIMATION

To ensure our nanoposts satisfy the local phase approximation for which adjacent elements are weakly coupled to one another, we analyze the effect of changing the spacing between elements by sweeping the lattice constant. Figure 5.8A and Figure 5.8B show the amplitude and phase at 530 nm wavelength respectively when sweeping both the diameter and phase of a periodic array of our nanoposts. As the amplitude and phase remain relatively invariant over this wide range of lattice constants about the design value (depicted by the dashed line), this indicates that the nanoposts are weakly coupled and can be treated as independent phase shifting elements.

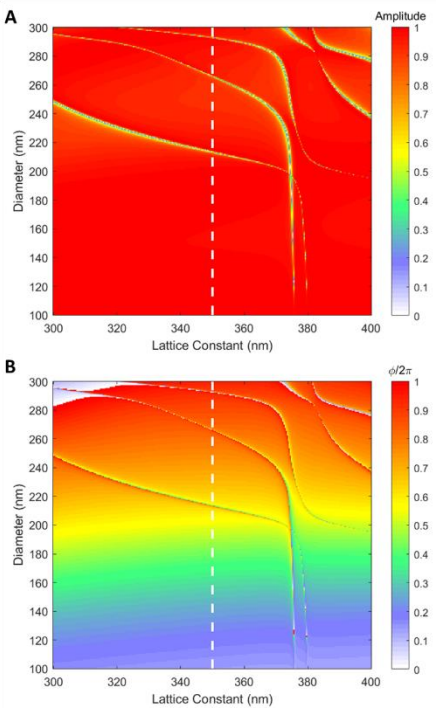


Figure 5.8. Transmission coefficient as a function of diameter and lattice constant. The transmission amplitude (A) and phase (B) are shown as a function of diameter and lattice constant at 530 nm wavelength. The white dashed line indicates the lattice constant value used for the nanopost design in the main text.

## 5.8 Modulation Transfer Function Measurement

The MTFs corresponding to the PSFs in Figure 5.5 are shown in Figure 5.9A and Figure 5.9B for the 1.5 mm (100 μm displacement) and 3 mm (50 μm displacement) cases respectively. While the singlets exhibit the best response of all the measured devices at their design wavelength, their responses degrade significantly under blue and red illumination, with more than a 30 dB reduction in some cases. The Alvarez EDOF metalens instead exhibits an attenuated frequency response compared to the singlets for green light, but in switching to off-design wavelengths the change in the MTF is substantially mitigated. Furthermore, the MTFs of the Alvarez EDOF metalens are not only more similar but are significantly improved relative to the blue and red cases for the singlets. The overall reduction in MTFs relative to the diffraction limit is attributed to the nonnegligible bandwidth of the LED sources used (15 nm for red, 30 nm for green, and 25 nm for blue) and fabrication imperfections.

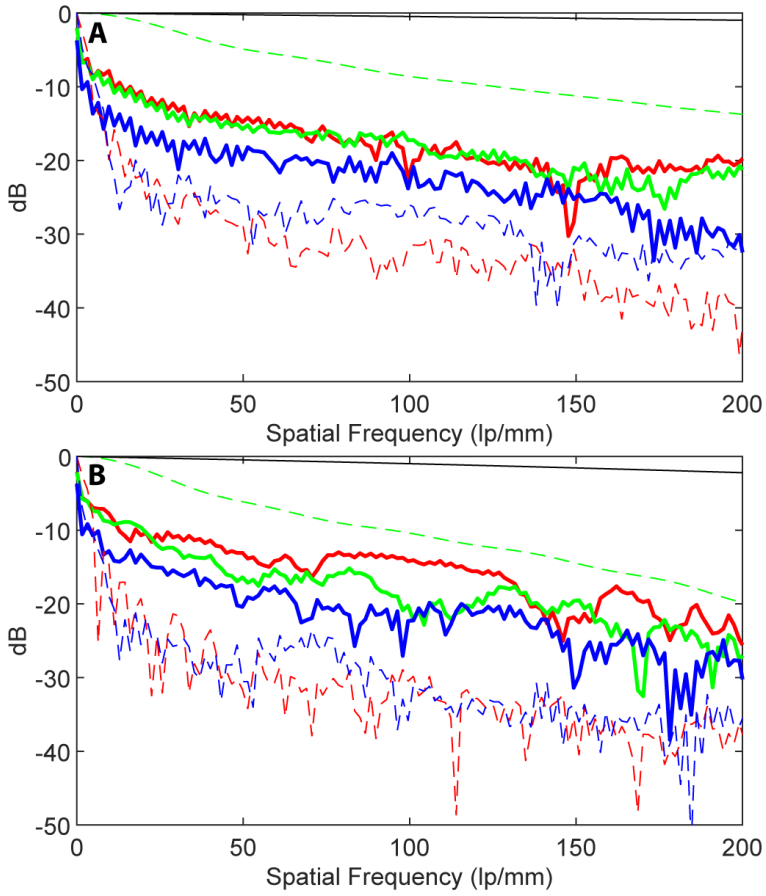


Figure 5.9. Modulation Transfer Functions. MTFs are plotted for the 1.5 mm focal length case in (A), for which the lateral displacement is 100 µm, and the 3 mm focal length case in (B), for which the lateral displacement is 50 µm. The black lines indicate the diffraction-limited MTF at 530 nm, the solid colored lines represent the measured MTFs at the wavelengths of their respective colors (red is 625 nm, green is 530 nm, blue is 455 nm) for the Alvarez EDOF metalens, while the dashed lines show the MTFs at the wavelengths of their respective colors for the singlet lenses.

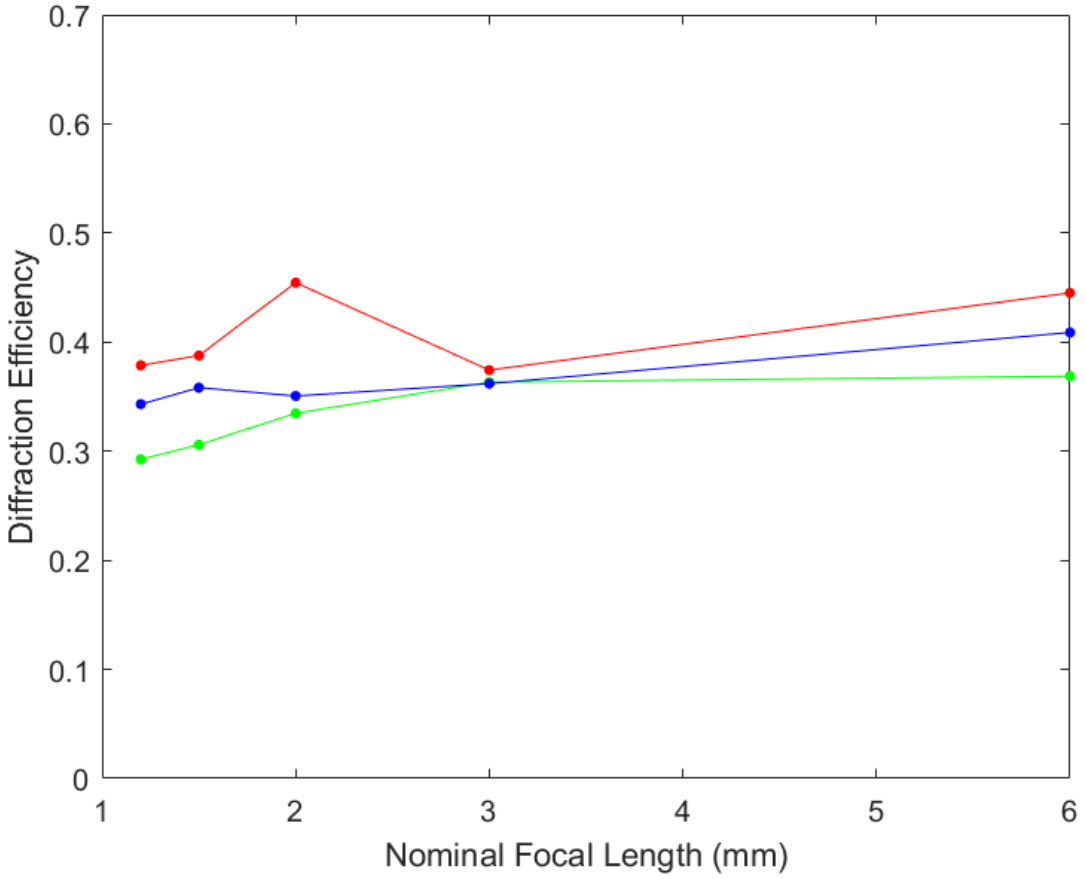


Figure 5.10. Measured diffraction efficiency. The measured diffraction efficiencies for 625 nm (red), 530 nm (green), and 455 nm (blue) wavelengths are shown as a function of nominal focal length, corresponding to lateral displacements in the range of 25 µm to 125 µm.

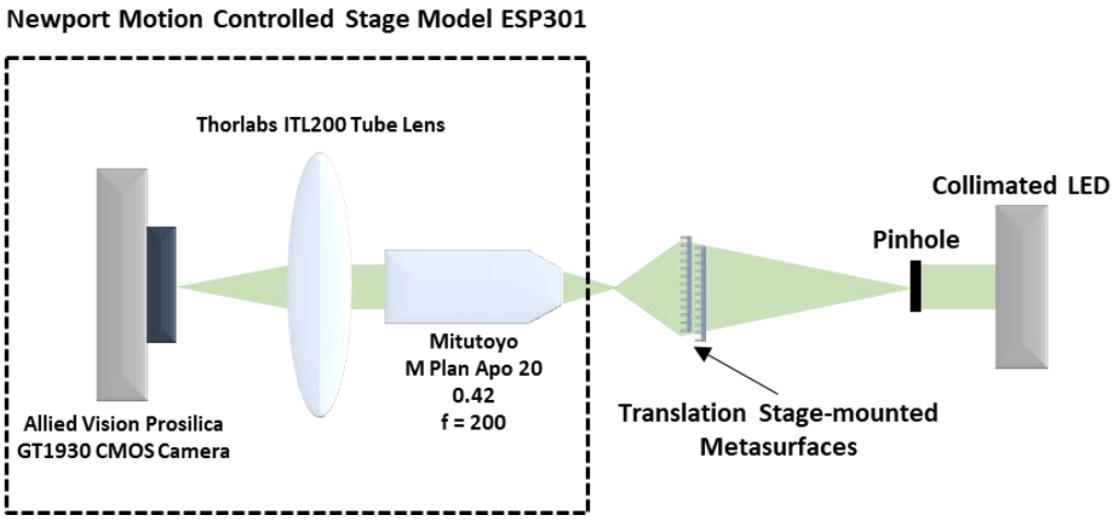


Figure 5.11. Point spread function measurement setup. The experimental setup for measuring point spread functions is depicted. The LED sources used were Thorlabs M455F1, M530F2, and M625F2.

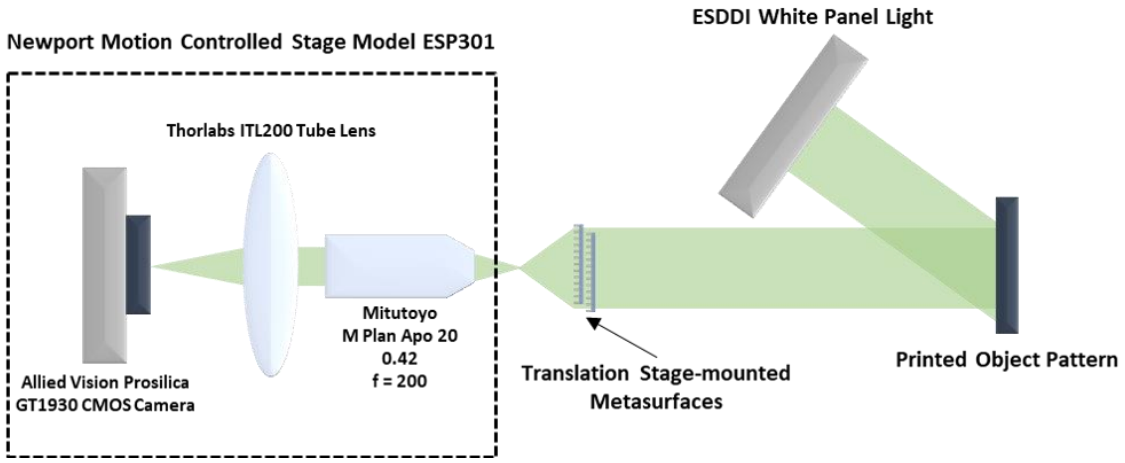


Figure 5.12. Imaging measurement setup. The experimental setup for capturing images using the Alvarez EDOF metalens.

## 5.9 Spatial and Spectral PSF Correlation Calculations

To quantify the field of view (FOV) of our imaging system, we simulate the point spread function (PSF) of our system under angled illumination and compute the inner product between the resultant PSF and a shifted version of the PSF obtained under normal incidence. The shifted version of our normal incidence PSF represents the response for a perfectly shift-invariant system. In these simulations, we simulate the full 1 mm aperture metasurfaces as complex amplitude masks via the angular spectrum method, where the complex values for each unit cell represents the transmission coefficients calculated by rigorous coupled-wave analysis for the corresponding angle of incidence. Performing these calculations over a range of field angles and for three different focal length states of our system, we define the field of view as the range over which the normalized correlation coefficient exceeds 0.5. In Figure 5.13 we see that at ~18°, the correlation coefficient falls to 0.5 for all three of the simulated focal length states, which by doubling to apply for negative incidence angles as well gives an estimate of ~36° for the total field of view of our system at 530 nm nominal wavelength.

We performed similar correlation calculations but as a function of illumination wavelength to assess the spectral bandwidth of the system. Treating the PSF at 530 nm wavelength as our reference, we calculated the correlation coefficient for wavelengths ranging from 400 nm to 700 nm, spanning the visible regime (Figure 5.14). Using the same criterion as for our FOV estimate, the bandwidth of our system extends from ~440-640 nm, representing coverage of wavelengths ranging from blue all the way to red.

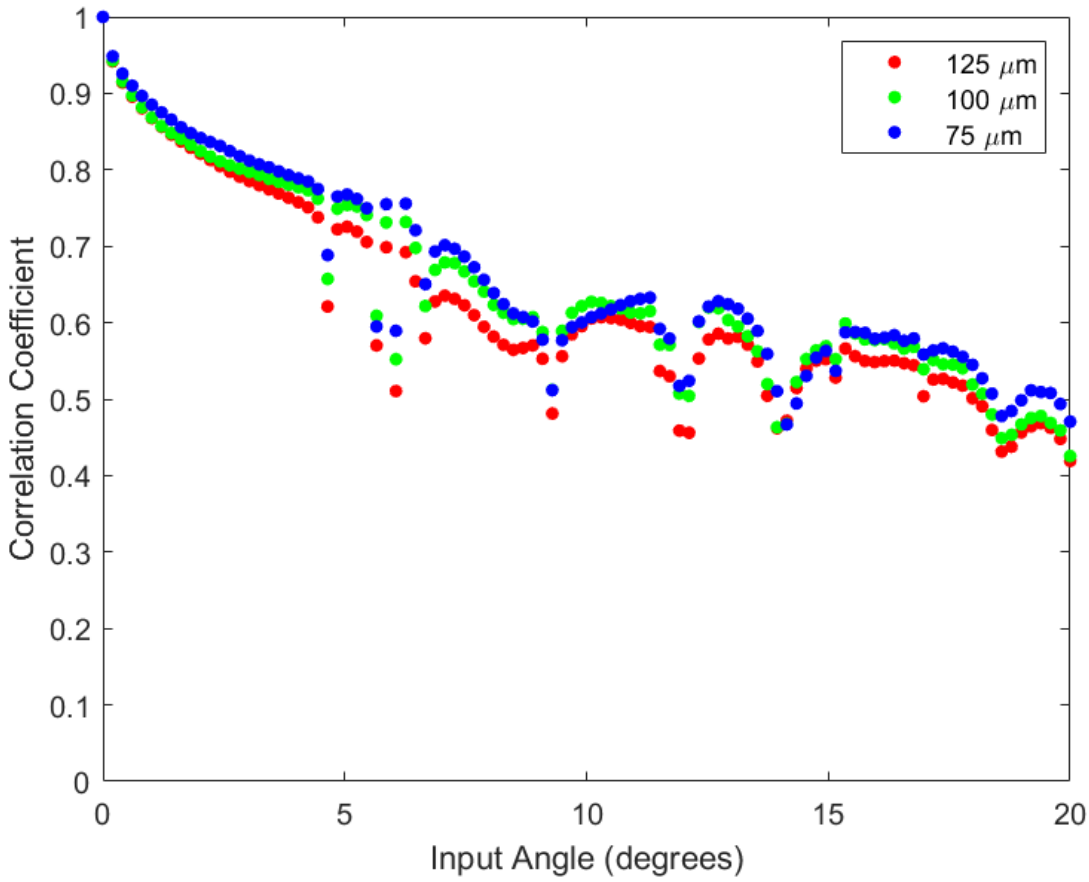


Figure 5.13. Point Spread Function Correlations with Input Angle. The simulated correlation coefficients for a range of input angles under 530 nm wavelength illumination. The different colors in the plot correspond to three different displacements of the two metasurfaces, corresponding to focal lengths of 1.2 mm, 1.5 mm, and 2 mm for the red, green, and blue colors in the plot respectively.

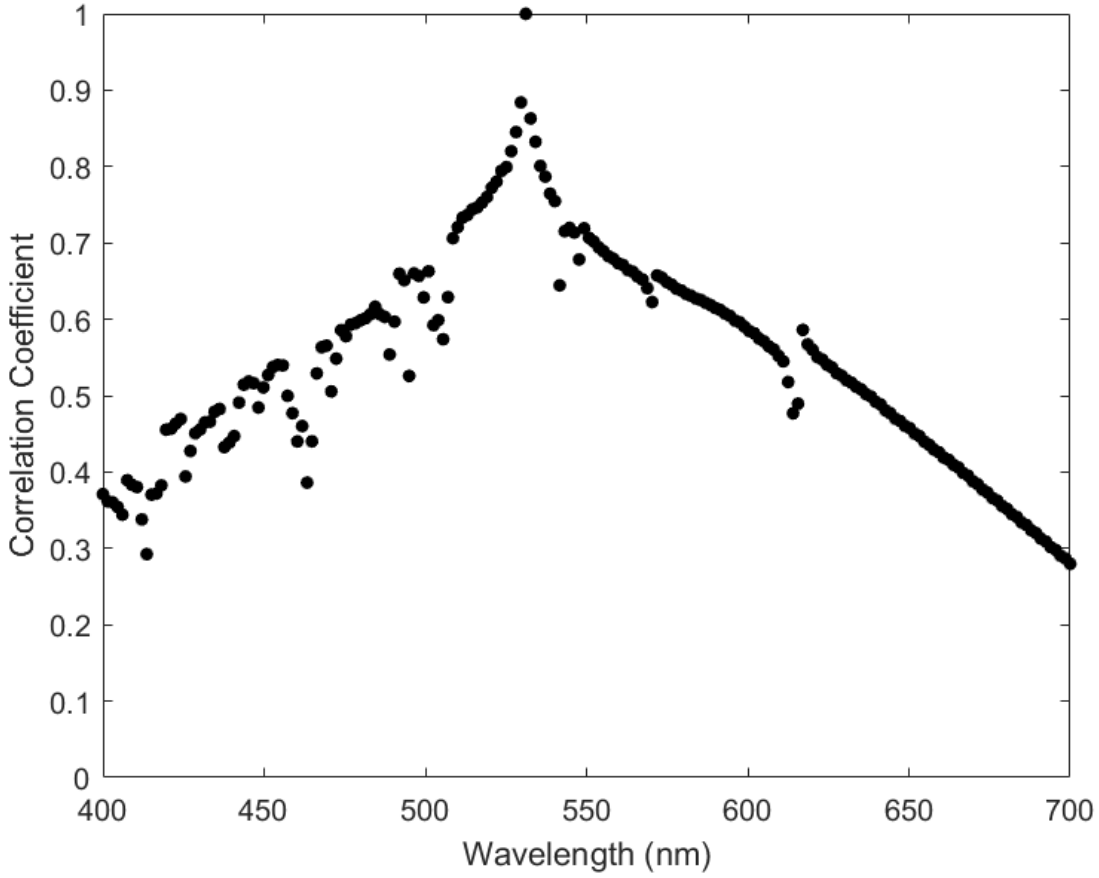


Figure 5.14. Point Spread Function Correlations with Wavelength. The simulated correlation coefficients for a range of input wavelengths under normal incidence illumination. The correlation of each wavelength's PSF is determined relative to the PSF at 530 nm wavelength.


Figure 5.15. Deconvolution Algorithm Comparison. Raw images captured of RGB characters are shown (A) for five different zoom levels and images after post-processing with Wiener deconvolution (B) and using the TV-regularized algorithm of the main text (C) are also shown. Wiener deconvolution in this work offers a 113x average computation time speedup but for high magnification levels, ringing artifacts become more significant.

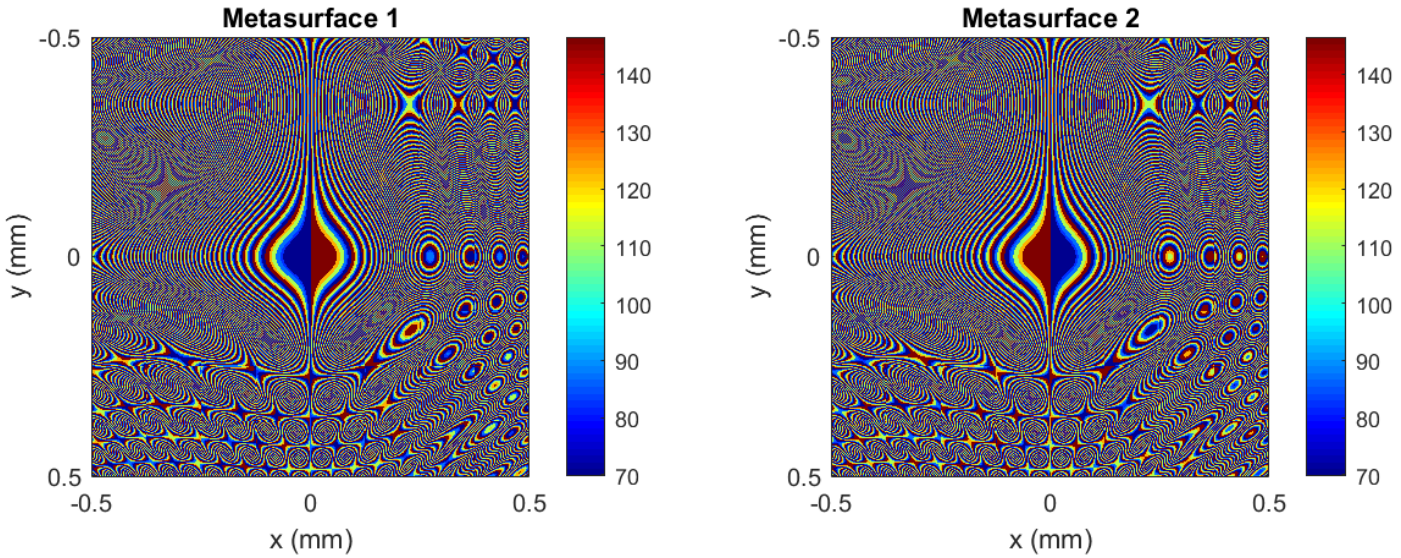


Figure 5.16. Metasurface Nanopost Radii Distributions. Radii distributions for the silicon nitride nanoposts are shown for both metasurfaces of the main text in nanometers.

# Chapter 6. DEPTH IMAGING WITH METASURFACES

*Reproduced with permission from [113], S. Colburn and A. Majumdar, "Metasurface Generation of Paired Accelerating and Rotating Optical Beams for Passive Ranging and Scene Reconstruction," ACS Photonics (2020). Copyright 2020. American Chemical Society.*

## 6.1 INTRODUCTION

Conventional cameras capture two-dimensional projections of intensity information from three-dimensional scenes without any knowledge of object depths. While this is often sufficient, depth information is crucial to the operation of numerous next-generation technologies, such as autonomous transportation and gesture recognition in augmented reality. A variety of approaches for collecting depth information from a scene exist [114,115], but these often require active illumination or multiple viewpoints that prohibitively increase system size. Alternatively, there are depth from defocus methods [116–119] that obtain depth information from a sequence of images under different defocus settings; however, this typically requires a dynamic setup where the optics are physically adjusted between each capture. Moreover, information theoretic calculations show that the precision from such depth from defocus methods is fundamentally limited for a standard lens [120,121], as the point spread function (PSF) varies slowly with changes in depth and it is often ambiguous whether an object is defocused away from or towards the lens.

There are, however, optical elements with more exotic PSFs compared to that of a standard lens, enabling significantly more precise depth discrimination. A prominent example of this is the double-helix PSF (DH-PSF), which distinguishes depths as it produces a beam with two foci that rotate continuously in plane in response to shifting the distance of a point source [33,121–125]. While single-shot depth imaging with a DH-PSF was demonstrated by analyzing an image's power cepstrum [126], the presence of sidelobes in the PSF limited the reconstructed image quality. The

image quality can be improved by capturing an additional reference image, albeit at the cost of not being a single-shot capture [121]. For real-time depth imaging, this entails physically adjusting the optics and repetitively capturing images. In one implementation of a double-helix-based depth camera [33], this functionality was achieved via a spatial light modulator (SLM) whose phase was switched between that of a DH-PSF and a cubic phase mask. This required an extensive setup comprising an imaging lens paired with a polarizer and the SLM, as well as a 4f correlator with two Fourier transform lenses [33].

Metasurfaces present a compelling route for miniaturizing such systems. While depth imaging was recently reported using a metasurface-based plenoptic camera [127], this required circularly polarized illumination and relied on small aperture (21.65 μm) lenses that limit lateral imaging resolution. Three-dimensional imaging was also demonstrated using a 3 mm aperture design with two interleaved off-axis focusing metalenses [128], but this leveraged the conventional lens PSF from depth from defocus methods, which limits the achievable depth precision [120,121]. Separately, a metasurface-based DH-PSF [129] was shown and used for depth imaging [130], but this operated in the infrared, utilized a separate refractive imaging lens, and did not reconstruct the scene. In this paper, we demonstrate a miniature, visible wavelength depth camera by collapsing the functionality of multiple supplemental lenses into a single polarization-insensitive spatially multiplexed metasurface with an aperture area of 2 $mm^2$. We exploit accelerating and rotating beams together to both extend the depth of field and improve precision. Coupled with deconvolution software, our system generates three-dimensional images, i.e., both a transverse depth map and a monochromatic focused scene image with a single snapshot under incoherent, visible illumination.

## 6.2 RESULTS

Our system comprises a dual aperture metasurface element, consisting of two adjacent metasurfaces with distinct and complementary PSFs that work in tandem to enable simultaneous scene reconstruction and depth acquisition (see Figure 6.1A). These metasurfaces form two separate and non-overlapping sub-images on a sensor array with a single snapshot. The detected sub-images are then processed via a deconvolution algorithm to produce both a focused image and a corresponding depth map. The functionality of the SLM, 4f correlator, and imaging lens present in the standard implementation [33] are combined into a single surface by setting the phase of each metasurface to a sum of a lens term and a wavefront coding term as

$$\Phi = \Phi_{lens} + \Phi_{WC}, \quad (18)$$

in which

$$\Phi_{lens} = \frac{2\pi}{\lambda}\left(f - \sqrt{x^2 + y^2 + f^2}\right), \quad (19)$$

where $\lambda$ is the optical wavelength, $x$ and $y$ are the in-plane position coordinates, and $f$ is the focal length of the lens. In our design, both metalenses have a 1 mm wide square aperture, focal length $f = 5$ mm, and a design wavelength $\lambda = 532$ nm.

For the first metasurface, the wavefront coding term creates an accelerating Airy beam [131], which exhibits a PSF that is highly invariant with depth due to its non-diffracting properties near focus. On the other hand the wavefront coding term for the second metasurface creates a rotating beam, which generates a double-helix PSF that is highly sensitive to changes in object depth [33]. Both metasurfaces are made of silicon nitride cylindrical nanoposts [25,49,50,105]. Silicon nitride was selected due to its CMOS compatibility and transparency over the visible wavelength range [52], while cylindrical nanoposts provide the benefit of polarization insensitivity [13]. The nanoposts in our design have a thickness $t =$

600 $nm$ and period $p = 400\ nm$. Figure 6.1B shows their transmission coefficient as a function of diameter calculated by rigorous coupled-wave analysis [56] (see Figure 6.7 for transmission coefficient data as a function of lattice constant). Using the simulated transmission coefficient's phase as a lookup table, a diameter is assigned to impart the desired phase for each position in equation (18).

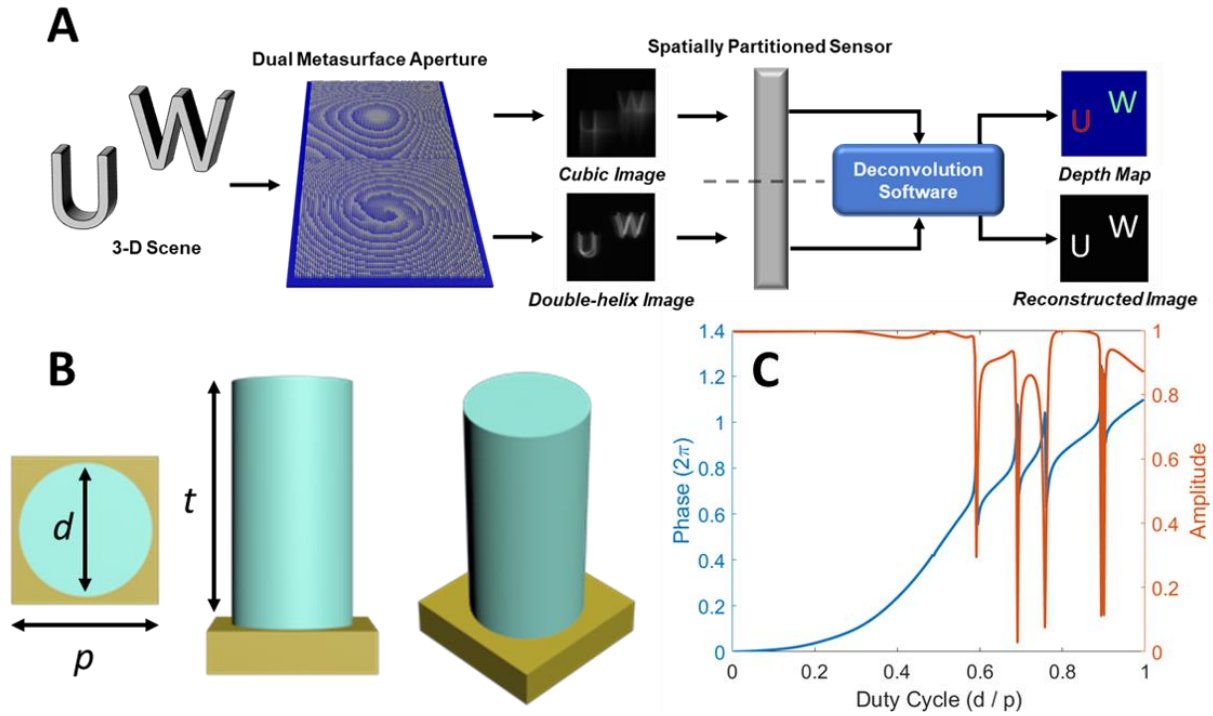


Figure 6.1. System Design. (A) Light from a scene incident on the dual aperture metasurface will be captured on a sensor as two side-by-side sub-images: one of them depth-variant and the other one depth-invariant. These sub-images will then be computationally processed to output both a reconstructed scene and a transverse depth map. (B) Schematic of the silicon nitride cylindrical nanoposts on a silicon dioxide substrate. The nanoposts have a lattice constant of $p$, diameter $d$, and thickness $t$. (C) The transmission coefficient (phase and amplitude) as a function of duty cycle for the designed nanoposts. The pillars have a thickness $t = 600\ nm$ and periodicity $p = 400\ nm$.

The depth-invariant design is achieved via an extended depth of focus (EDOF) metalens [25] with the wavefront coding term

$$\Phi_{WC} = \frac{\alpha}{L^3}(x^3 + y^3), \quad (20)$$

where $L$ is half the aperture width, and $\alpha$ is a constant that multiplies the cubic phase modulation term to generate an accelerating Airy beam that produces a misfocus-insensitive PSF [24,25,27,28,33,105]. Figure 6.2A shows simulated PSFs for the EDOF metalens with $\alpha = 20\pi$ as the point source is shifted to different depths along the optical axis, demonstrating the uniformity in the response. While this metalens does not focus to a point and therefore captures blurry images, by calibration with a single PSF measurement and subsequent deconvolution, focused images can be reconstructed with high fidelity over a wide depth range [25].

Complementing the depth-invariant design, the depth-variant metasurface creating a rotating beam leverages a DH-PSF. The wavefront coding term of a double-helix metalens is determined via a sum of Laguerre-Gaussian modes [31,32,121] and a block-iterative weighted projections algorithm [132–134] (see Figure 6.8). Figure 6.2B shows simulated PSFs for the designed DH metalens, exhibiting distinct intensity patterns for each depth unlike the case of the EDOF metalens. In an imaging system, the DH metalens creates two spatially shifted and rotated copies of objects, where the rotation angle between the two copies is determined by the distance of the object being imaged.

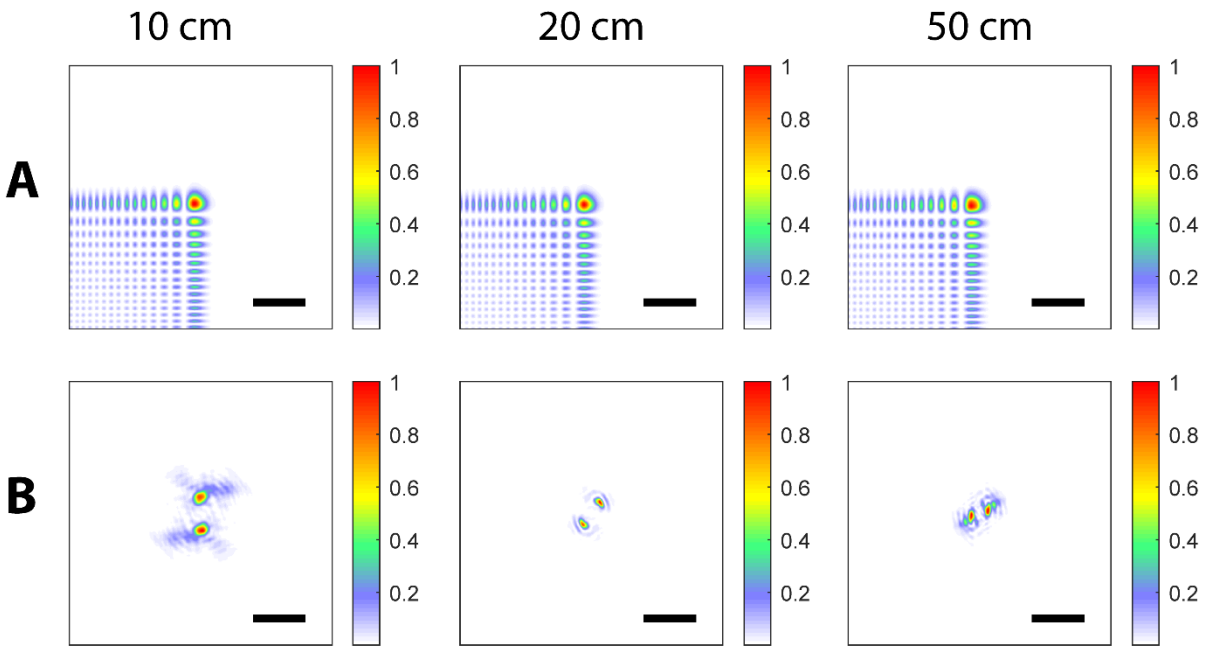


Figure 6.2. Simulated metasurface point spread functions. The normalized intensities of the simulated PSFs are shown for the EDOF (A) and DH-PSF (B) metalenses for three different object distances. Scale bar 32 μm.

We then fabricated the dual aperture metasurface to validate our design. Figure 6.3A shows a picture of the sample mounted on a microscope slide. An optical micrograph of the adjacent metasurfaces in Figure 6.3B shows the asymmetry in their phase profiles, where the different colored zones correspond to regions of different diameters that were selected to achieve $2\pi$ phase coverage. In Figure 6.3C and 3D, scanning electron micrographs depict zoomed in views of the nanoposts on a rectangular lattice at normal and $45^o$ incidence respectively.

We then measured the PSFs of the fabricated metasurfaces. As expected, the PSF of the EDOF metasurface varied minimally with depth (Figure 6.4A), while that of the DH metalens (Figure 6.4B) strongly depends on the point source distance, demonstrating a large change ($\sim 87^o$) in orientation angle over the measured depth range (Figure 6.4C). Furthermore, the orientation angle of the lobes in the measured DH-PSFs as a function of depth agrees very well with the theory [32,121]. The measured diffraction and transmission efficiencies of the full combined metasurface aperture were 75% and 91% respectively.

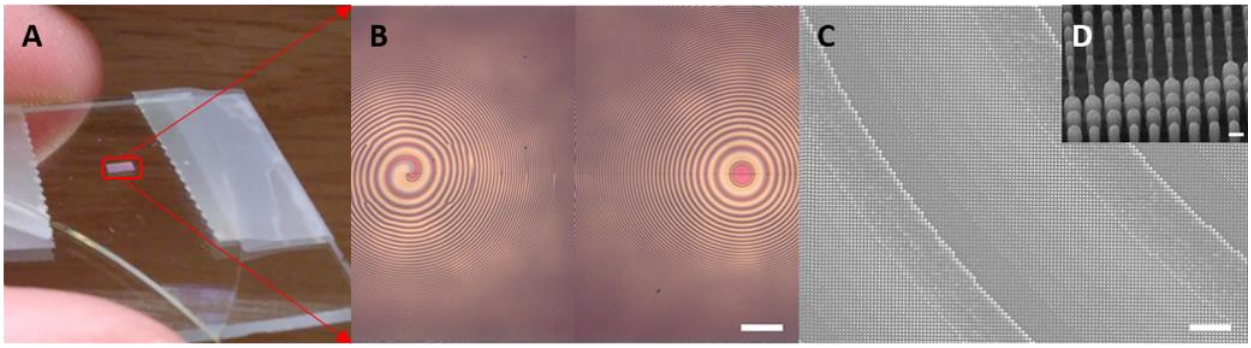


Figure 6.3. Fabricated Metasurface. (A) Optical image of the metasurface on a glass slide for testing. (B) Optical microscope image of the dual aperture metasurface. Scale bar 0.125 mm. Scanning electron micrographs at normal (C) and $45^{o}$ incidence (D) where the scale bars are 5 μm and 300 nm respectively.

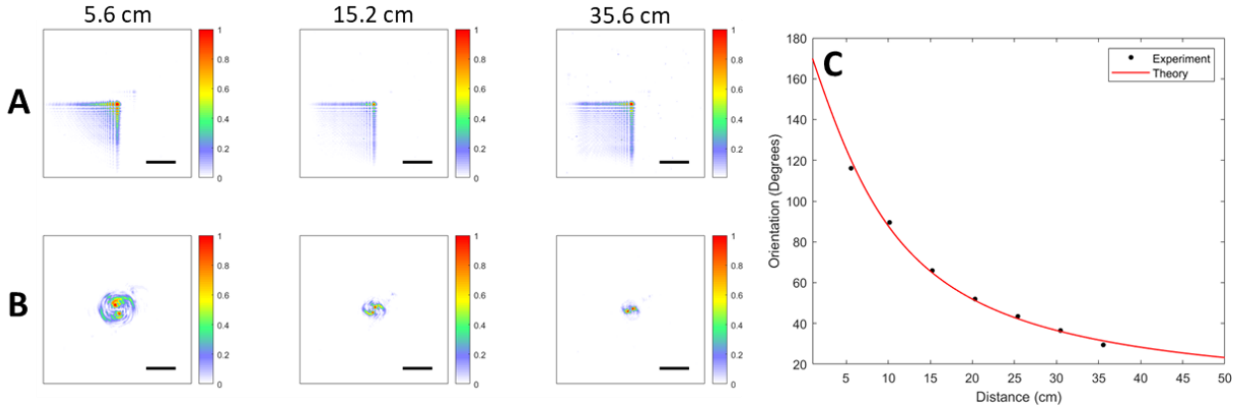


Figure 6.4. Metasurface Characterization. Normalized measured intensities of the point spread functions for the EDOF (A) and DH-PSF (B) metalenses for three different object distances. Scale bar 78 μm. (C) Orientation angle of the double-helix foci as a function of object distance.

Armed with our dual metasurface aperture exhibiting complementary depth responses, we performed a computational imaging experiment on a scene consisting of patterns on standard printer paper located at different depths. Our patterns were illuminated with a wideband incoherent white light source but the light incident on our sensor was spectrally filtered via a 1 nm full width at half maximum bandpass filter centered at 532 nm wavelength. Each captured image comprised two sub-images (Figure 6.5A). The full scene was then reconstructed by applying a total variation-regularized deconvolution algorithm [112] to the sub-image produced by the EDOF metalens and its measured PSF. After segmenting the reconstructed image and labelling objects for depth estimation, we could estimate the experimental DH-PSF for each object of interest. Figure 6.5B shows the PSF calculated from the image of a "3" character located 6.5 cm away from the metasurface. With the calculated PSFs, we estimated the depth per object (see Methods for further details). Applying this computational framework, we reconstructed scenes and calculated depth maps for the "3" character of Figure 6.5B located at 5 different depths in the 6.5 cm to 16.9 cm range (Figure 6.5D-E).

As the DH-PSF's rotation angle depends on the wavefront's accumulated Gouy phase [31,32], off-axis aberrations such as field curvature induce rotation offsets to the PSF that vary as a function of field angle (i.e., the angle to an object in the scene as measured from the optical axis). In a refractive lens system with multiple surfaces that mitigate aberrations from off-axis light (e.g., Petzval field curvature, coma, etc.), the resulting focal shift and rotation offset are negligible and the depth can be extracted directly from a calibration curve [33] as in Figure 6.4C. Our metalens, however, does not correct for these off-axis aberrations (Figure 6.9). Hence, naively treating all fields angles in the same manner produces erroneous depth estimates as the focal shift is nonnegligible. To address this, our algorithm accounts for focal shifts induced by off-axis

aberrations and correspondingly compensates the rotation angle to improve the depth estimation accuracy by calculating the additional Gouy phase due to field angle (details are found in the succeeding sections).

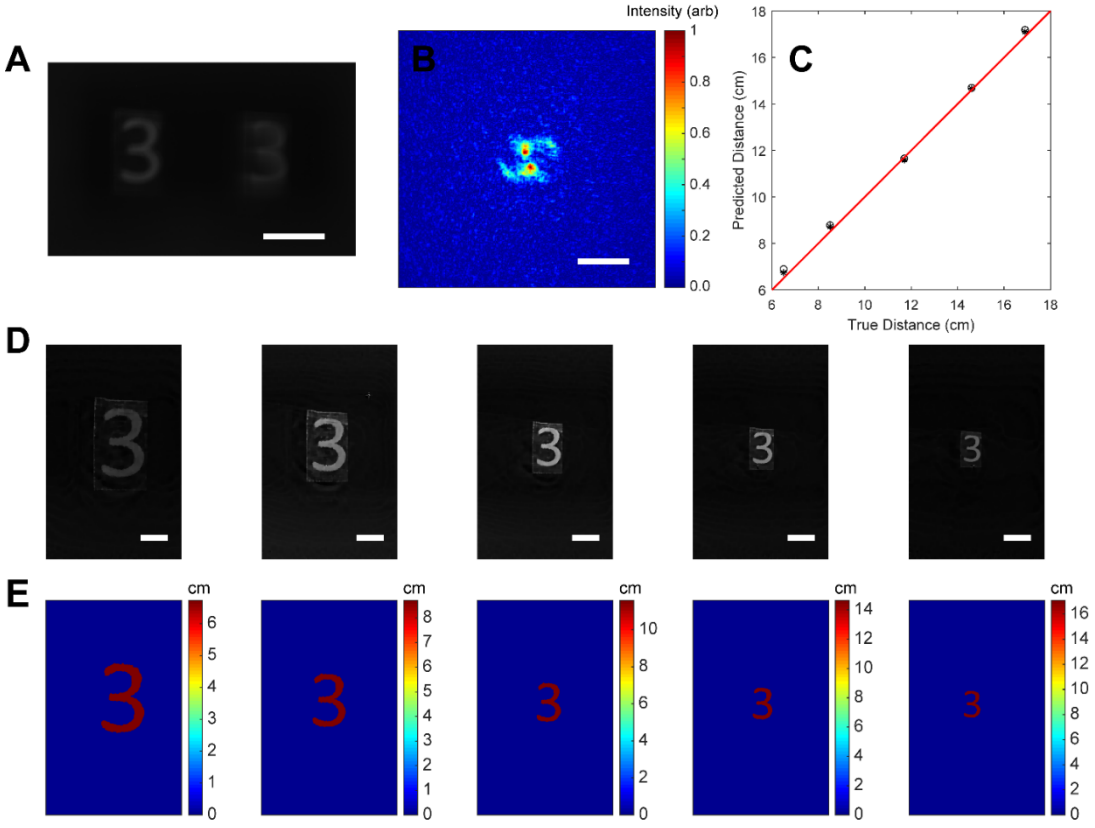


Figure 6.5. Single Object Depth Imaging. (A) Raw and unpartitioned image with the double-helix metalens sub-image on the left and the EDOF metalens sub-image on the right. Scale bar 0.5 mm. (B) Estimated DH-PSF from the image in (A). Predicted distances compared to the true distances are plotted in (C) for the case of imaging a "3" character at five different distances, where the reconstructed images and depth maps are shown in (D) and (E) respectively. The circles and asterisks in (C) correspond respectively to depth estimates without and with corrections accounting for changes in Gouy phase due to field angle. The red line denotes the performance of a perfect depth estimation algorithm. Scale bars are 78 μm and 0.2 mm in (B) and (D) respectively.

For the case of the single object “3” character at five different depths, the accuracy of our estimation is demonstrated in Figure 6.5C, where the estimated and true depths strongly agree. In this case, accounting for off-axis aberrations had minimal effect as there was little rotation offset to mitigate because the “3” characters were located near the center of the field of view. We then applied our framework to a scene comprising more than one object located off-axis with higher field angles, consisting of a further located “U” character and a closer “W” character. Here, the captured data (Figure 6.6A) and the subsequently reconstructed image (Figure 6.6B) allowed us to estimate distinct double-helix PSFs for each character, shown in Figure 6.6C and 6D for the “U” and “W” respectively. A naive depth estimation without accounting for off-axis focal shift yields highly erroneous depth estimates; however, once the change in Gouy phase due to the field angle of each character is compensated for, the estimates agree well with the true depths once again (Figure 6.6E). With the depth estimates of both Figure 6.5 and Figure 6.6, our system achieves a fractional ranging error of 1.7%, higher than but of similar order compared to existing commercial passive depth cameras but with a much more compact form factor.

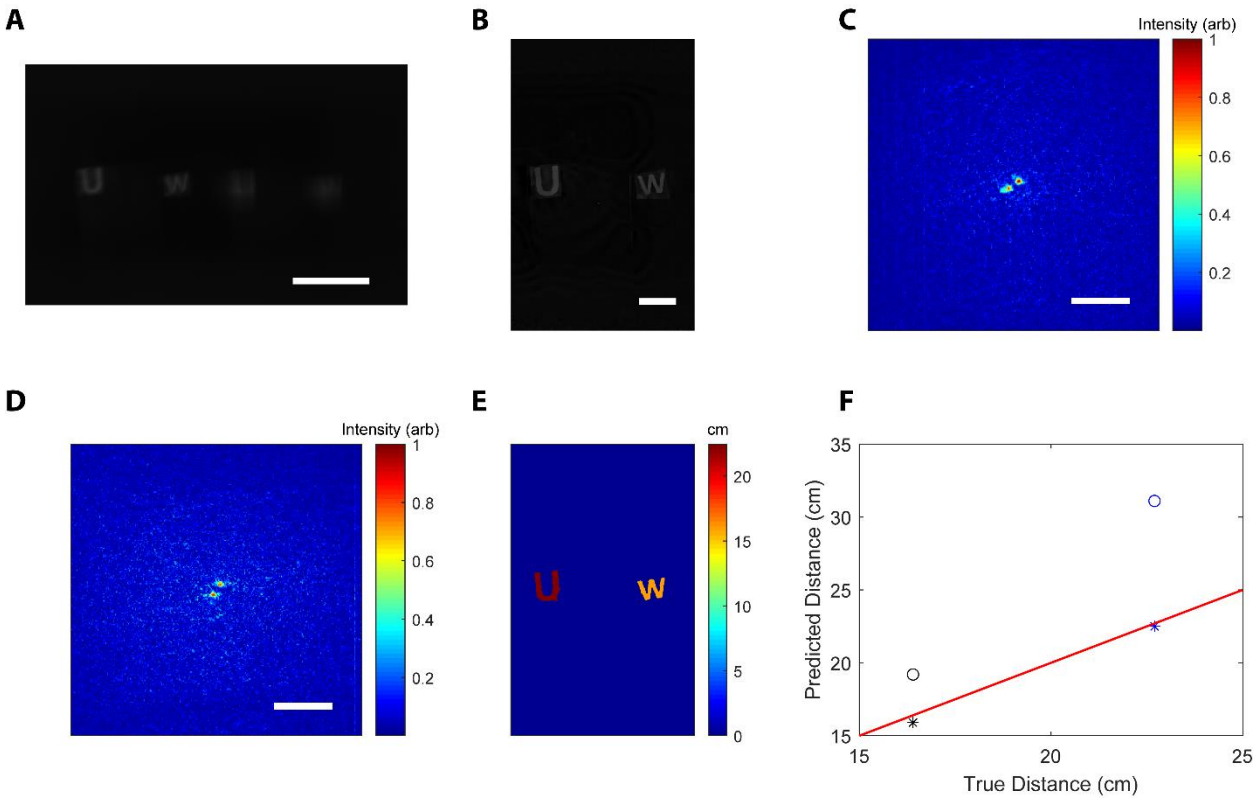


Figure 6.6. Imaging Multiple Objects. (A) Raw and unpartitioned image with the double-helix metalens sub-image on the left and the EDOF metalens sub-image on the right of a scene with "U" and "W" characters located at different distances. Scale bar 0.51 mm. (B) Reconstructed object scene with a scale bar of 0.2 mm. Estimated DH-PSFs are shown for the "U" (C) and "W" (D) with scale bars of 78 μm. (E) The calculated transverse depth map for the scene. (F) Predicted distances compared to the true distances are plotted, where the circles and asterisks correspond respectively to depth estimates without and with corrections accounting for changes in Gouy phase due to field angle. The blue and black points correspond to the "U" and "W" characters respectively. The red line denotes the performance of a perfect depth estimation algorithm.

## 6.3 DISCUSSION

While various depth estimation techniques exist, our method enables 3-D imaging of scenes in an ultra-compact form factor without having to take multiple snapshots under different optical configurations. By combining the imaging lens and the wavefront coding steps into a single aperture, the size is reduced significantly, albeit at the cost of introducing off-axis and chromatic aberrations from the metalenses. These aberrations, however, are largely mitigated by limiting the optical bandwidth in detection and accounting for the field angle dependence of the focal length when calculating depths. The form factor reduction will be beneficial for a variety of systems, such as head-mounted displays for augmented reality which impose stringent size limitations on sensors. Shifting the functionality of the SLM and 4f correlator into the dual aperture metalens not only contributed to this size reduction, but also eliminated the time multiplexing required in previously reported PSF engineering methods [33]. Eliminating this time multiplexing serves a dual purpose: it reduces the system complexity and also circumvents the issue of a scene changing between sequential captures. Although the spatial multiplexing of two metasurfaces does induce parallax, the center-to-center separation of each metasurface poses a negligible angular separation (less than 0.4°) for the average object depth in our experiments.

We demonstrated a compact and visible wavelength depth camera for three-dimensional imaging based on a dual aperture optical metasurface. Our system relies on imparting two complementary wavefront coding functions on light from a scene to create an accelerating and a rotating beam, enabling simultaneous focused scene reconstruction at all distances and depth discrimination for objects in the scene with a single image snapshot. Compared to existing implementations of depth cameras, we demonstrated an ultra-compact solution with a 2 $mm^2$ optical aperture and without requiring a separate imaging lens, 4f correlator, or spatial light

modulator. While use of metasurfaces must contend with off-axis aberrations via computational correction and a limited operating bandwidth, recent works demonstrating achromatic lensing [25,45–47,82–84,127,135] and wide-angle field of view correction by stacking metasurfaces [136] are feasible routes for circumventing these issues. Although in this work we focused on the 5 cm to 35 cm range, applicable to gesture recognition for augmented reality systems, the optical design is readily adaptable to other length scales and operating wavelengths by appropriately tuning the cubic phase strength of the EDOF metalens, aperture size, and focal length.

## 6.4 METHODS

### 6.4.1 *Metasurface Design*

To optimize the phase for the double-helix metalens, a block-iterative weighted projections algorithm [132–134] was used that axially constrained the diffracted intensity along the optical axis at 8 different parallel planes, decomposed the metasurface mask into a linear combination of Laguerre-Gaussian modes, and enforced a phase-only constraint for the mask (see succeeding sections for additional details of the algorithm). The nanopost designs were first simulated using the Stanford S4 rigorous coupled-wave analysis package [56] to extract their transmission coefficients. These coefficients were then assigned to their corresponding diameters and treated as complex amplitude pixels in a custom wave optics MATLAB code to simulate the full designs. The wave optics simulation was based on the angular spectrum method [57].

### 6.4.2 *Fabrication*

Our process began with a cleaved piece of glass from a 100 mm double side polished fused silica wafer. The silicon nitride layer was first deposited via plasma-enhanced chemical vapor deposition

at 350°C. The sample was then spin coated with ZEP 520A and an 8 nm Au/Pd charge dissipation layer was sputtered on top. Both metasurface patterns were subsequently exposed adjacent to one another using a JEOL JBX6300FS electron-beam lithography system at 100kV. After stripping the Au/Pd layer, the sample was developed in amyl acetate. A 50 nm layer of aluminum was evaporated and lifted off via sonication in methylene chloride, acetone, and isopropyl alcohol. The silicon nitride layer was then etched with the remaining aluminum as a hard mask using an inductively coupled plasma etcher with a $CHF_3$ and $SF_6$ chemistry. The remaining aluminum was finally removed by immersing the sample in AD-10 photoresist developer. An Au/Pd layer was sputtered on top of the sample for charge dissipation when capturing scanning electron micrographs.

### 6.4.3 *Experiment*

To measure the point spread functions, a 50 μm pinhole was aligned with the sample and illuminated from behind with a LED source. For imaging experiments, the pinhole was removed and objects on printer paper were illuminated with a white light LED array panel source. For both the point spread functions and images, the captured signal was limited in bandwidth via a 1 nm full width at half maximum spectral bandpass filter centered at 532 nm wavelength. The images and PSFs were magnified via a custom relay microscope comprising an objective and tube lens. The experimental setups and corresponding part numbers for components used in this work are shown in Figure 6.10 and Figure 6.11 for PSF measurement and imaging respectively. The transmission efficiency was calculated by taking the power ratio of the light on the sensor side of the metasurface to that on the source side. The diffraction efficiency was calculated by taking the ratio of the power at the metasurface on the sensor side to that at the focal plane. These powers

were measured by integrating the intensity within the area of the metasurface aperture from images when it was backside illuminated.

### 6.4.4 *Deconvolution*

The reconstructed scene images are calculated by deconvolving the cubic sub-images using a total variation-regularized deconvolution algorithm. This deconvolution problem is solved using an open source MATLAB library based on the split Bregman method [112], which iteratively solves the reconstruction problem. After segmenting the reconstructed scene and labelling objects for depth estimation, we applied a Kaiser window in each desired subregion of the image with a labelled object. Subsequent deconvolution of the subregions via a Wiener filter applied to the double-helix sub-image provided an estimate of the DH-PSF for each object of interest. With the PSF estimates for each labelled object, the orientation angles of the lobes were extracted and compared against the experimentally calibrated angle response of the DH-PSF as a function of depth (Figure 6.4C), providing a depth estimate for each object. We calculate the focal shift due to off-axis aberrations by finding ray intersections and determine the subsequent change in Gouy phase and rotation angle by using an ABCD formalism for the Gaussian complex beam parameter (see succeeding sections for details). As scene reconstruction and depth estimation per segmented object average 26.5 and 0.8 seconds respectively using an ordinary personal laptop computer (12 GB RAM, Intel CORE i7) with the algorithm implemented in MATLAB, real-time processing would not be possible, though video data could be processed offline after data capture. Significant speedups to achieve real-time processing are feasible, however, if dedicated hardware were used, such as field-programmable gate arrays (FPGAs) or graphics processing units (GPUs).

## 6.5 NANOPOST DESIGN AND THE VALIDITY OF THE UNIT CELL APPROXIMATION

To evaluate the validity of using our RCWA-simulated nanoposts in an aperiodic structure, we simulate our nanoposts as a function of both diameter and lattice constant. If the transmission coefficient is invariant as the lattice constant changes, i.e., the separation gap between nanoposts varies, then we can assume that the scatterers are weakly coupled to one another and that making the unit cell approximation is justified. Here, we have included simulation results for our nanopost design as we vary both the diameter and lattice constant (Figure 6.7), demonstrating minimal change in the transmission coefficient as a function of lattice constant over a wide range.

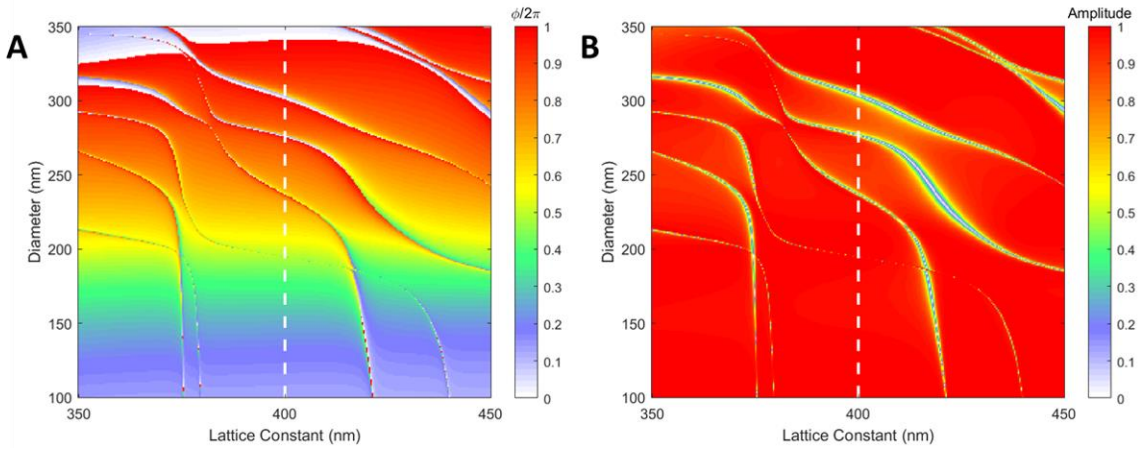


Figure 6.7. Transmission Coefficient as a function of both diameter and lattice constant. Phase (A) and amplitude (B) of the transmission coefficient for the nanopost design as a function of both diameter and lattice constant. The white dashed line corresponds to the lattice constant used for the actual design in the main text.

## 6.6 High-efficiency Double-helix PSF Phase Mask Optimization

To design the double-helix (DH) metalens, we sum the phase functions of a standard metalens and that of high-efficiency rotating point spread function (HR-PSF) [132]. Compared to a standard DH-PSF, a HR-PSF exhibits a DH-PSF with reduced sidelobes that concentrates more of the diffracted power within the two main peaks. These reduced sidelobes improve the signal-to-noise ratio of captured images and enable less noisy estimates of PSFs when performing depth imaging. To calculate the phase required for the HR-PSF, we use a block-iterative weighted projections algorithm [133,134] based on an algorithm from a prior work [132]. We reproduce some of the discussion of the algorithm here for convenience and provide parameter values specifically used in our design.

The phase mask optimization consists of a loop upon which successive iterations increase the amount of power within the two main lobes of the PSF. The loop consists of 1) diffracting light incident on the current iteration of the phase mask to several different axial planes 2) applying a spatial constraint on the intensity in those planes to reduce sidelobes 3) backpropagating the constrained intensity to the phase mask's plane 4) decomposing the resultant electric field into a Laguerre-Gaussian mode sum 5) applying a constraint in the Laguerre-Gaussian modal plane to ensure a continuous rotation between axial sample planes and 6) converting the electric field to a phase-only mask.

Prior to the loop, the electric field required for a double-helix PSF is calculated by summing the five required Laguerre-Gaussian $(m, n)$ modes [121]. Here, $m$ and $n$ are the azimuthal and radial numbers that characterize each Laguerre-Gaussian mode as in the original algorithm [32,132]. In this modal sum, the aperture of our design is 1 mm, our pitch is 400 nm to match our metasurface lattice constant, the wavelength is 532 nm, and the waist radius is set to 0.125 mm. The initial

phase mask for the optimization is then set to the phase of this calculated electric field sum, setting the amplitude function to unity everywhere. As has been previously shown [132], such a phase mask produces a DH-PSF but with reduced efficiency and large sidelobes. With this initial estimate, the diffracted intensity was then calculated at 8 different axial planes in the range from 1.5 cm to 27 cm, obeying the axial sampling rate for intensity required for three-dimensional diffracted fields [133]. At each of these axial planes, the two peaks were separately fit to two-dimensional gaussian functions. The sum of these fit functions constituted a constraint mask for that axial plane that would be multiplied with the diffracted intensity at each iteration. This constrained the optical power to be concentrated within the peaks at the desired positions of the lobes. When determining the axial sampling rate, the inner and outer radii that define the region of support (i.e., where the function is nonzero) for the initial intensity pattern at the device plane correspond to the radial distance of the peaks (they are symmetric with respect to the origin) plus or minus two times the standard deviation of the gaussian fit to these peaks. This definition of the function support for the initial distribution ensures almost all the power in the aperture is encompassed.

In the optimization loop, after applying the spatial constraints at the axial planes based on our fit functions that we calculated from our initial phase mask, we backpropagate the light from each of these axial planes back to the plane of our phase mask. We then perform a weighted average over these backpropagated fields, with the nearest plane having a weight of 0.01 and the furthest weighted at 0.24 with intermediate planes increasing linearly so that the sum of all weights is 1. This more heavily emphasizes further axial planes as we found during testing that this had a more pronounced effect on improving the overall efficiency.

After performing a weighted average of the backpropagated fields, we decompose the resulting electric field into a Laguerre-Gaussian basis. We then multiply this mode decomposition by a modal constraint function of the same functional form used in the original phase optimization algorithm [132]. This constraint function ensures that in the Laguerre-Gaussian modal plane, the modes lie along a line where the slope determines the rotation rate of the point spread function. Utilizing their cloud weight function [132] and notation we use a value of $p = 10$ to set our constraint.

The phase masks before and after optimization are shown in Figure 6.8A-B. The optimized mask constitutes the wavefront coding term for the double-helix metalens of the main text. The Laguerre-Gaussian modal decomposition of this optimized wavefront coding term as compared is shown in Figure 6.8C, where we see that the modes primarily lie along a line that dictates the rotation rate. In Figure 6.8D, the transfer function efficiency as a function of iteration and axial sample plane is shown, demonstrating a marked improvement and convergence after only a few iterations. As expected, the later axial planes improve more as these were weighted more heavily. Finally, we show the simulated point spread functions for a metalens with a wavefront coding term based on the initial phase mask (Figure 6.8E) and the optimized phase mask (Figure 6.8F) of the main text, exhibiting a noticeable reduction in sidelobes after optimization.

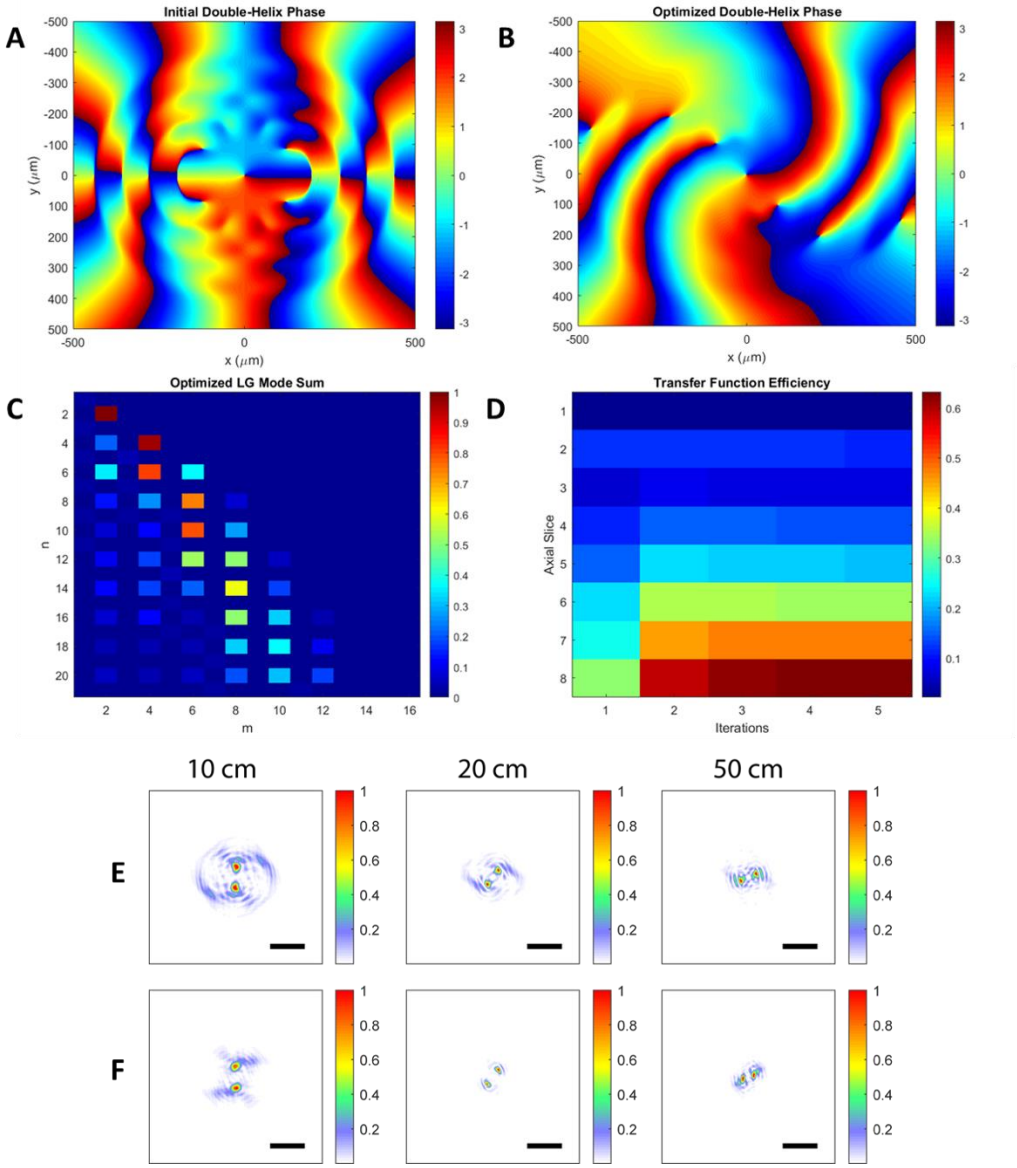


Figure 6.8. Double-helix phase optimization. (A) The modal decomposition of the optimized mask design in the Laguerre-Gaussian modal plane. (B) Transfer function efficiency as a function of both axial sample plane and number of optimization iterations. The efficiency is defined as the power fraction retained within two standard deviations of the Gaussian peaks that define the spatial constraint function. The initial (C) and optimized (D) phase masks are also shown. In (E) and (F) are the simulated point spread functions for the initial and optimized designs respectively.

## 6.7 VALIDITY OF SUPERPOSING PHASE MASKS FOR PSF ENGINEERING

In our metasurface system, we collapse the functionality of several optical elements into a single surface. Specifically, we do not have a separate refractive imaging lens and do not use a 4f system to modify the PSF of the system. Instead, we superpose the phase functions of wavefront coding terms and a metalens' phase to achieve the desired PSFs. We present a brief derivation below to demonstrate the equivalence of this method compared to imparting a wavefront coding term at the Fourier plane of a 4f system.

The PSF $h$ of a system is equal to the Fourier transform of its generalized pupil function $P(x, y)$

$$h = FT\{P(x, y)\}, \quad (21)$$

For a pupil function with phase $\Phi$, this gives

$$h = FT\left\{e^{j\Phi}\right\}, \quad (22)$$

For a simple imaging lens with phase $\Phi = \Phi_L$

$$h_{lens} = FT\left\{e^{j\Phi_L}\right\}, \quad (23)$$

If we modify the phase to superpose a lens term and a wavefront coding term such that $\Phi = \Phi_L + \Phi_{WC}$ we get

$$h_{WC} = FT\left\{e^{j\Phi_L}\, e^{j\Phi_{WC}}\right\} = FT\left\{e^{j\Phi_L}\right\} * FT\left\{e^{j\Phi_{WC}}\right\}, \quad (24)$$

where * denotes convolution. Alternatively, for a 4f system the PSF can be determined by exciting with a delta function, yielding

$$h_{4f} = FT\left\{e^{j\Phi_{4f}}\right\}, \quad (25)$$

as the Fourier transform of the first lens yields a planewave and a phase mask of $\Phi_{4f}$ at the Fourier plane then produces an electric field of $e^{j\Phi_{4f}}$. If a 4f system is preceded by a separate imaging lens, then the PSF of the full system can be found by convolving the two PSFs, giving

$$h_{system} = h_{lens} * h_{4f} = FT\{e^{j\Phi_L}\} * FT\{e^{j\Phi_{4f}}\}, \quad (26)$$

When the Fourier plane phase is set to that of the wavefront coding term of interest, $\Phi_{4f} = \Phi_{WC}$, we see that superposing the phase function onto a metasurface lens phase function gives the same PSF.

## 6.8 Scene Reconstruction Algorithm

In our optical system, the extended depth of focus (EDOF) metalens produces a blurred image of the scene that is then corrupted by sensor noise. One of the two primary goals of our system is to produce a high-fidelity reconstructed version of the scene (the other being generating a transverse depth map). For scene reconstruction, our imaging problem is described by the equation $y = Kx + n$ where $y$ is the image captured by the sensor, $K$ is the blur kernel or matrix form of the measured PSF of the optical element (i.e., that of the EDOF metalens), $x$ is the latent image or object scene that we're trying to reconstruct in vectorized form, and $n$ is noise that corrupts the captured data. For our PSF, we measure at a single depth of 15.24 cm due to the depth-invariant nature of the EDOF metalens. As $n$ is unknown, we cannot exactly solve for $x$. Various deconvolution techniques exist to extract an estimate and here we use a total variation-regularized deconvolution algorithm based on the split Bregman method [112]. This algorithm iteratively solves for $x$ by balancing denoising and deconvolution via a regularization parameter $\mu$ as in the equation below

$$x = argmin_x \, TV(x) + \frac{\mu}{2}\|Kx - y\|_2^2, \quad (27)$$

In this equation, $TV$ denotes the total variation operator that computes the sum of the gradient magnitudes throughout the image, thereby enforcing a smoothness constraint that suppresses noise as the image is deconvolved. In this work, we use $\mu = 2 \times 10^4$.

## 6.9 Depth Estimation Algorithm

After the scene has been reconstructed via deconvolution of the EDOF metalens' image, we find and label objects for detection in the reconstructed image. This process entails first binary thresholding the image, followed by morphological opening (i.e., removing objects smaller than a certain area) to eliminate any small artifacts (e.g., due to noise) for which we are not interested in calculating the depth. Following this, we label the connected components of the image to determine all the objects of interest. For each labelled object, we calculate the centroid and apply a square Kaiser window [33] of width 700 and $\beta = 5$ to the reconstructed and double-helix images centered at the centroid position from the binary image. Applying this window eliminates objects from other regions in the image but more smoothly attenuates features as compared to a rectangular window. After applying the Kaiser window to the reconstructed image, we treat this as the ground truth and solve for the PSF that gives rise to the Kaiser window-multiplied double-helix sub-image. To calculate this PSF, we use Wiener deconvolution with $NSR = 4 \times 10^{-6}$ as below

$$\hat{h}_{DH} = \frac{\hat{o}_{TV}^{*} \hat{\imath}_{DH}}{|\hat{o}_{TV}|^2 + NSR}, \quad (28)$$

where ^ denotes the Fourier domain representation of an image, $o_{TV}$ is the TV-regularized reconstructed object scene, $i_{DH}$ is the captured double-helix sub-image, and $h_{DH}$ is the resulting double-helix PSF estimate. With this estimate, we then extract the orientation angle of the lobes as this parameter enables us to calculate depth. To find the locations of the two peaks, the image is first binary thresholded and the number of connected component objects is calculated. This threshold level is initially set high and the original image is then thresholded repeatedly with a progressively decreasing threshold level as long as the number of connected components objects is still 2. This procedure enables us to isolate the two regions where the peaks are located with as

large an area surrounding each region as possible. With the two regions where the peaks are located determined, we then perform a weighted centroid calculation for each of these objects in order to identify the peaks' positions. With the two positions determined, we calculate the orientation angle.

When there is negligible focal shift due to off-axis aberrations, the determined orientation angle of the DH-PSF estimate is directly related to depth via the experimental calibration curve of Figure 6.4C of the main text. This orientation angle is determined by the properties of Laguerre-Gaussian mode sums. When the modal indices in a Laguerre-Gaussian superposition lie along a line, meaning the (m, n) indices are related by an equation of a line, the result is a rotating intensity distribution [32]. The in-plane orientation $\varphi$ of this intensity distribution is

$$\varphi = \varphi_0 + V_1\psi(\hat{z}), \quad (29)$$

where $\varphi_0$ is the initial orientation at $z = 0$, $V_1$ is the slope of the line that passes through the (m, n) indices in the modal sum, and $\psi(\hat{z}) = -\tan^{-1}\hat{z}$ is the Gouy phase in which $\hat{z}$ is the distance $z$ normalized by the Rayleigh length $z_R = \frac{\pi w_0^2}{\lambda}$. In Figure 6.4C of the main text, the theoretical curve comes from this equation by setting $w_0$ equal to the 0.125 mm waist radius of our double-helix wavefront coding mask and then fitting the $\varphi_0$ offset parameter to the experimental data to account for any experimental rotation misalignment. After fitting the experimental data, we solved for the depth $z$

$$z = \frac{\pi w_0^2}{\lambda}\tan\left[\frac{\varphi_0 - \varphi}{V_1}\right], \quad (30)$$

## 6.10 Correcting Depth Estimates for Nonzero Field Angles

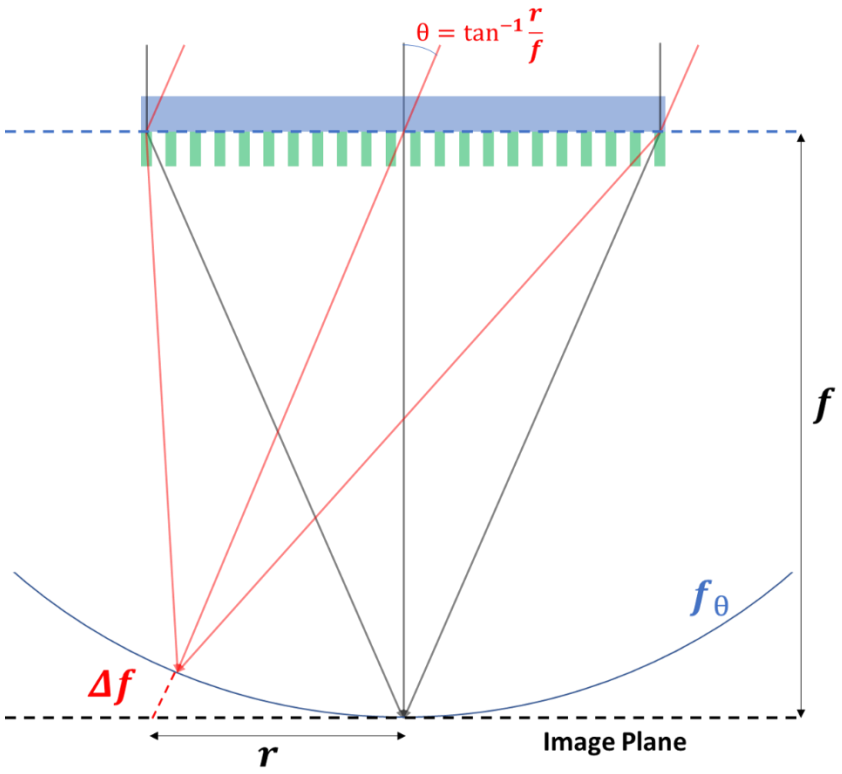


Figure 6.9. Depth estimates and nonzero field angles. Diagram of the system indicating the shift in focal length that induces additional Gouy phase shift due to off-axis illumination.

While our depth estimation algorithm described in the previous section works when the focal plane is fixed, as the field angle for an object increases (i.e., as it moves off-axis and further out into the field of view), off-axis aberrations (e.g., Petzval field curvature, coma, etc.) induce a shift of the focal plane that reduces the accuracy of the depth estimate. In a refractive lens system with multiple surfaces, the field curvature and coma are often mitigated; however, in our metasurface system consisting of a single surface, these aberrations are not addressed in the lens design itself. Hence, the standard depth estimation for a DH-PSF becomes erroneous, and the estimates need to be modified for a metasurface that simultaneously performs the functionality of the imaging lens. As our sensor position is fixed with respect to our metasurface so that we are imaging our metalens' nominal focal plane of 5 mm, the shift in focal plane makes it so that for off-axis fields angles, there is an additional propagation distance from the position of the new focal plane in order to reach the sensor (Figure 6.9). This additional wavefront propagation causes further rotation as dictated by the change in accumulated Gouy phase. This renders our orientation calibration curve accurate only for small field angles near normal incidence. This focal shift, however, is well described by an ABCD formalism, allowing us to predict the change in Gouy phase as a function of field angle and compensate the orientation angle appropriately. In the following paragraphs, we derive and describe our algorithm for correcting this.

To perform this compensation, for an object for which we are estimating the depth, we first determine its field angle. With our reconstructed image, as a lens converts angles to positions, the centroid of each object lets us find its field angle by simple geometry, yielding $\theta = \tan^{-1}\frac{r}{f}$, where $r$ is the radial distance from the center of the image to the centroid of the segmented object and $f$ is the nominal (i.e., zero field angle) focal length of the metalens (Figure 6.9). To determine the focal length for the field angle $\theta$, we use generalized Snell's law [8] and find the intersection

position of rays incident on a metalens' aperture at that field angle. This process begins by relating the metalens' phase

$$\varphi(r) = \frac{2\pi}{\lambda_0}\left(f - \sqrt{r^2 + f^2}\right), \quad (31)$$

to the incident and transmitted angles via

$$\sin\theta_t - \sin\theta_i = \frac{\lambda_0}{2\pi}\frac{\partial\varphi(r)}{\partial r} = \frac{-r}{\sqrt{r^2+f^2}}, \quad (32)$$

If we let a ray pass through $r = 0$, we have that $\theta_t = \theta_i$, yielding $y = x\tan\theta_i$ for the $(x, y)$ coordinates of the line characterizing the ray's trajectory after passing through the lens. Alternatively, if a ray instead passes through a radial position $r = r_0$ with incidence angle $\theta_i$, the equation describing the ray's trajectory is $y = m_s x + r_0$ where the slope $m_s$ is given by

$$m_s = \tan\left[\sin^{-1}\left(\frac{-r_0}{\sqrt{r_0^2+f^2}} + \sin\theta_i\right)\right], \quad (33)$$

Equating the line equations for these two ray trajectories, we find the intersection point giving

$$(x_{int}, y_{int}) = \left(\frac{r_0}{\tan\theta_i - m_s}, \frac{m_s r}{\tan\theta_i - m_s} + r_0\right), \quad (34)$$

The focal length under this illumination condition is then given by $f_\theta = \sqrt{x_{int}^2 + y_{int}^2}$. This length, however, varies depending on the value of $r_0$. As such, we calculate an average $\overline{f_\theta}$ of two cases, where $r_0 = \pm R$ for which $R$ is the metalens' aperture radius (0.5 mm).

With our calculated field-angle dependent focal length for an object, the next step was to determine the change in Gouy phase for which we would need to compensate our measured orientation angle to estimate the depth. To do this, we use the complex Gaussian beam parameter $q(z) = z + iz_R$, where $z$ is the propagation distance and $z_R$ is the Rayleigh length. In our system,

when we have a focal shift due to off-axis illumination, from the plane of the metasurface to our image plane, we can separate the change in the beam parameter $q$ into two successive operations. The first operation is the action of a thin lens with focal length $\overline{f_\theta}$, which yields

$$q_2 = \frac{q_1}{-\frac{q_1}{\overline{f_\theta}}+1}, \quad (35)$$

while the second is the effect of propagating through free-space by some distance $d$ which gives

$$q_2 = q_1 + d, \quad (36)$$

Sequentially applying these operations to our initial beam parameter of $q_i = iz_R$, we obtain a final beam parameter

$$q_f = \frac{d\left(\frac{z_R}{\overline{f_\theta}}\right)^2 - \frac{z_R^2}{\overline{f_\theta}} + d + iz_R}{\left(\frac{z_R}{\overline{f_\theta}}\right)^2 + 1}, \quad (37)$$

With the final gaussian beam parameter, the new Rayleigh length is equal to the imaginary part

$$z_{Rf} = \frac{z_R}{\left(\frac{z_R}{\overline{f_\theta}}\right)^2 + 1}, \quad (38)$$

from which we can solve for the final waist radius

$$w_{0f} = \frac{w_0}{\sqrt{\left(\frac{\pi w_0^2}{\lambda \overline{f_\theta}}\right)^2 + 1}}, \quad (39)$$

where $w_0$ is the initial waist radius, the phase mask's design value of 0.125 mm.

Bringing these different pieces together, we can now update our depth estimate $z$ to include a rotation offset term, yielding

$$z_{corrected} = \frac{\pi w_0^2}{\lambda} \tan\left[\frac{\varphi_0 + \varphi_{defocus} - \varphi}{V_1}\right], \quad (40)$$

where $\varphi_{defocus}$ is the rotation due to the Gouy phase accumulated from a focal shift $\Delta f$. This offset term is given by

$$\varphi_{defocus} = V_1 \psi\left(\frac{\Delta f}{w_{0f}}\right), \quad (41)$$

Here, the focal shift is determined by the difference between the total distance from the lens to the image plane when incident at field angle $\theta$, given by $f \sec\theta$ and the calculated field angle-dependent focal length $\bar{f}_\theta$, giving

$$\Delta f = f \sec\theta - \bar{f}_\theta, \quad (42)$$

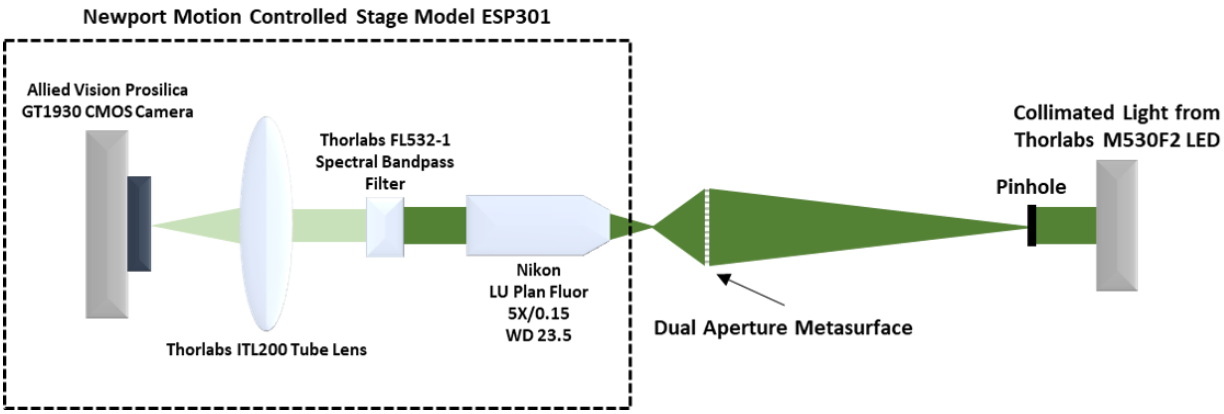


Figure 6.10. Point spread function measurement setup. The experimental setup for measuring the point spread functions of the metasurfaces with the specific components used.

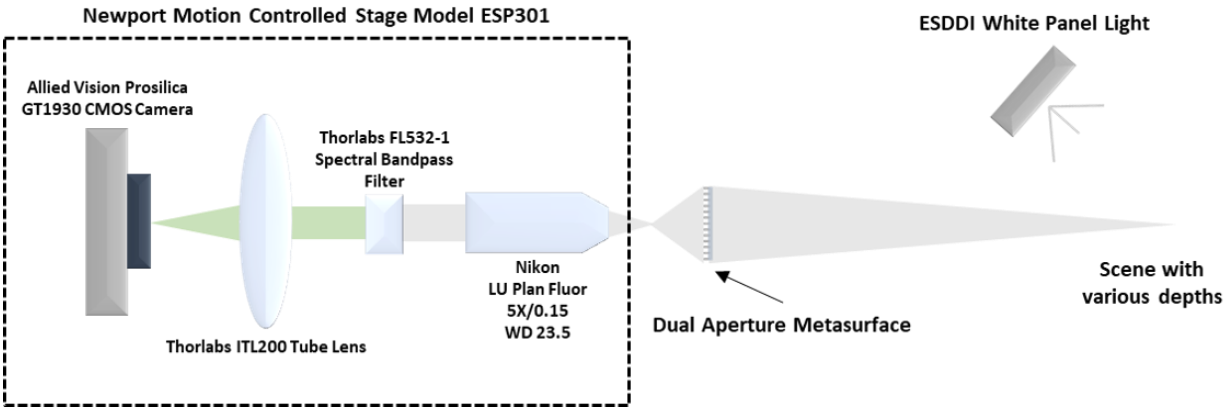


Figure 6.11. Imaging Setup. The experimental setup for imaging with the dual aperture metasurface with the specific components used.

# Chapter 7. CONCLUDING REMARKS

In this dissertation, we detailed some of the work we have conducted in exploring imaging modalities with metasurfaces and how we can use computation as a component for enhancing system performance and circumventing certain aberrations. We make the claim that metasurfaces, or possibly other diffractive elements as well, may be able to deliver a benefit in terms of reducing the size and weight of existing, bulky refractive systems; however, in order to realize these benefits, they often come at the cost of reduced image quality, increased chromatic aberrations, and efficiency reduction. The central theme of the work detailed in this dissertation is leveraging computation to overcome some of the limitations of existing metasurface technology (e.g., chromatic aberrations, limitations on scaling of the aperture with dispersion engineering, and reliance on polarization-dependent scatterers). By treating computation as an integral aspect of the image formation process, rather than relying on a cascaded system of corrective optical elements, we can factor much of aberration correction functionality into software, thereby reducing the form factor of the system.

We began this dissertation by giving a general background on metasurfaces, detailing material considerations and their significance with respect to efficiency, how we computationally model metasurface systems, and highlighted some of the differences between metasurfaces and other diffractive elements (e.g., binary optics and kinoforms). After providing some background, we then shifted towards detailing some of our own contributions in the area of full-color imaging with metasurfaces. By modifying the design of a metalens' phase mask, we engineered the point spread function to be insensitive to misfocus over a wide wavelength range, enabling computational recovery of the scene for wavelengths spanning the visible regime. We then summarized our work on developing a large area, Alvarez metalens system that achieved a wide

focal length tuning range that supported varifocal zoom imaging capability. While this Alvarez lens itself was not paired with a deconvolution block, we expanded on this design by incorporating a quartic polynomial into the phase mask design to achieve simultaneous depth of focus and focal length tuning. This system enabled both varifocal and achromatic behavior at the same time without any polarization dependence or reliance on dispersion-engineered scatterers, which have strong limitations on aperture scaling. Finally, in the previous chapter, we detailed our work on synthesizing a cubic phase mask, extended depth of focus metalens with a second metasurface that exhibited a double-helix point spread function. By pairing these two metasurfaces in a single aperture, we were able to not only reconstruct a scene but also acquire the depths of objects with a single camera snapshot. This depth acquisition system enabled a low fractional ranging error and did so with a single metasurface aperture based on a technique that typically requires a separate imaging lens, two Fourier transform lenses, a spatial light modulator, and a polarizer [33]. This combination of the imaging functionality and the wavefront coding for the double-helix point spread function, however, came at the cost of introducing rotation behavior from off-axis incident light. We worked around this limitation by modifying the depth estimation algorithm to compensate for the rotation offset based on the change in Gouy phase over the field of view.

There is still significant work to do to make these systems practical and adopted for certain use cases, but we believe that the benefit offered by computation is notable. At this juncture, for consumer photography applications that achieve extremely high-quality aesthetically pleasing images with small form factor cameras, ubiquitous in smartphones today, metasurfaces appear unlikely to supplant the optimized refractive assemblies on which these systems are based. There are, however, a range of applications for which metasurface computational imaging systems may find use. These use cases are for the most size and weight-constrained applications, perhaps in

implantable microscopy settings where minimally invasive form factors are necessary, in space applications and solar imaging where the polarization-manipulation capability of metasurfaces could enhance the behavior of primitive but radiation-hardened imaging optics such as photon sieves [137], or in machine vision or defense applications where the utmost size reduction is necessary and refractive elements cannot deliver the required form factor.

While metasurfaces can modify wavefronts in an ultrathin form factor, in lens designs requiring multiple surfaces, another significant limitation is that free space occupies a significant portion of the system's volume. As such, metasurfaces can only provide modest benefits in terms of size reduction when multiple, cascaded elements are required. One route to work around this is to leverage the benefits of folded optics technology. By fabricating multiple metasurfaces on the same substrate and treating the substrate as a waveguide, the total track length of a lens design can be significantly reduced. This has been explored in the context of a metasurface-based spectrometer [138], which relied on folding in one dimension, but lens designs could also utilize annular folded optics [139], akin to Cassegrain reflectors. Such annular folded optics can also be combined with wavefront coding functions for extending the depth of field [140].

The most significant benefit of using metasurfaces may arise when their uniqueness compared to existing diffractive elements is leveraged. While arbitrary phase masks can be mapped onto binary optics, up to resolution limitations, and different functionalities can be imparted on separate diffracted orders, in a single order we cannot multiplex different behavior based on incident angle, polarization, and wavelength. While such sensitivity with polarization and angle are often considered drawbacks of an optical system, by modifying the metasurface scatterer design to intentionally discriminate such properties of a wavefront, we conceivably could enhance the information collection capability of a system. Exotic scatterer designs that distinguish

polarization states and incidence angle differently combined with computation could potentially improve the quality or information content of captured images, perhaps in the same sense that the PSF engineering we explored in this dissertation jumbled information from a scene in exotically shaped and blurry PSFs but that yielded increases in the total amount of information captured when coupled with post-processing software [28].

Another research direction that can extend the functionality explored in this thesis is end-to-end design techniques [141] in which the optics and software are jointly optimized as part of an imaging pipeline. In this approach, an analytical model of the image formation process as well as the effect of the deconvolution filter can be implemented based on algorithmic differentiation, enabling fast calculation of gradients via backpropagation and flexibility in defining figures of merit (e.g., based on the image quality of the output image from the system). The flexibility and power of machine learning frameworks developed in recent years lends themselves well to such optimization problems.

While much of the work in this thesis related to achieving similar functionality for different wavelengths, in many applications, distinguishing finely spaced wavelengths is critical (e.g., spectroscopy and hyperspectral imaging). One potential route for achieving this is to use an optical element that has a strongly wavelength-dependent point spread function but that yields high Fisher information with respect to change in wavelength. One such point spread function is the double-helix mask discussed in the preceding section, where the lens terms yields a strong longitudinal chromatic aberration that induces wavelength-dependent rotation of the PSF. In much the same manner that a calibration curve relating depth to orientation angle can be determined, orientation with respect to wavelength could also be calculated. By measuring the PSFs of broadband light with some spectrum, one could envision computationally extracting the spectrum based on the

calibration curve. This could conceivably be extended to hyperspectral imaging applications as well by pairing with a cubic metalens to generate a focused image of the scene.

Altogether, the work detailed here represents a survey of using computational imaging in conjunction with metasurfaces as a means for circumventing certain limitations, explored through several imaging modalities. Though in this dissertation we focused on using these systems in the visible wavelength range, the utility of such systems may be even greater for other wavelength ranges such as the mid-infrared, where optics and pixels are more expensive, and where computation is a more viable alternative compared to in the visible range where silicon-based detectors are cheap and efficient. Future work on combining polarization, wavelength, and incidence angle sensitivity can expand on the work detailed here. Furthermore, while we focused mostly on correcting chromatic aberrations, computation may be of benefit for handling Seidel aberrations that we cannot eliminate with a single layer metasurface.

# BIBLIOGRAPHY


1. J. N. Mait, G. W. Euliss, and R. A. Athale, "Computational imaging," Adv. Opt. Photon., AOP **10**, 409–483 (2018).
2. F. Heide, M. Steinberger, Y.-T. Tsai, M. Rouf, D. Pająk, D. Reddy, O. Gallo, J. Liu, W. Heidrich, K. Egiazarian, J. Kautz, and K. Pulli, "FlexISP: A Flexible Camera Image Processing Framework," ACM Trans. Graph. **33**, 231:1–231:13 (2014).
3. C. J. Schuler, M. Hirsch, S. Harmeling, and B. Schölkopf, "Non-stationary correction of optical aberrations," in *2011 International Conference on Computer Vision* (2011), pp. 659–666.
4. F. Heide, M. Rouf, M. B. Hullin, B. Labitzke, W. Heidrich, and A. Kolb, "High-quality Computational Imaging Through Simple Lenses," ACM Trans. Graph. **32**, 149:1–149:14 (2013).
5. A. Ozcan and E. McLeod, "Lensless Imaging and Sensing," Annu. Rev. Biomed. Eng. **18**, 77–102 (2016).
6. N. Yu and F. Capasso, "Flat optics with designer metasurfaces," Nat Mater **13**, 139–150 (2014).
7. "Planar Photonics with Metasurfaces | Science," http://science.sciencemag.org/content/339/6125/1232009.
8. N. Yu, P. Genevet, M. A. Kats, F. Aieta, J.-P. Tetienne, F. Capasso, and Z. Gaburro, "Light Propagation with Phase Discontinuities: Generalized Laws of Reflection and Refraction," Science **334**, 333–337 (2011).
9. S. Jahani and Z. Jacob, "All-dielectric metamaterials," Nat Nano **11**, 23–36 (2016).
10. A. Arbabi, R. M. Briggs, Y. Horie, M. Bagheri, and A. Faraon, "Efficient dielectric metasurface collimating lenses for mid-infrared quantum cascade lasers," Opt. Express, OE **23**, 33310–33317 (2015).
11. P. R. West, J. L. Stewart, A. V. Kildishev, V. M. Shalaev, V. V. Shkunov, F. Strohkendl, Y. A. Zakharenkov, R. K. Dodds, and R. Byren, "All-dielectric subwavelength metasurface focusing lens," Opt. Express, OE **22**, 26212–26221 (2014).
12. F. Lu, F. G. Sedgwick, V. Karagodsky, C. Chase, and C. J. Chang-Hasnain, "Planar high-numerical-aperture low-loss focusing reflectors and lenses using subwavelength high contrast gratings," Opt. Express, OE **18**, 12606–12614 (2010).
13. A. Arbabi, Y. Horie, A. J. Ball, M. Bagheri, and A. Faraon, "Subwavelength-thick lenses with high numerical apertures and large efficiency based on high-contrast transmitarrays," Nature Communications **6**, ncomms8069 (2015).
14. D. Lin, P. Fan, E. Hasman, and M. L. Brongersma, "Dielectric gradient metasurface optical elements," Science **345**, 298–302 (2014).
15. D. Fattal, J. Li, Z. Peng, M. Fiorentino, and R. G. Beausoleil, "Flat dielectric grating reflectors with focusing abilities," Nat Photon **4**, 466–470 (2010).
16. "Aberration-Free Ultrathin Flat Lenses and Axicons at Telecom Wavelengths Based on Plasmonic Metasurfaces - Nano Letters (ACS Publications)," http://pubs.acs.org/doi/abs/10.1021/nl302516v.
17. M. I. Shalaev, J. Sun, A. Tsukernik, A. Pandey, K. Nikolskiy, and N. M. Litchinitser, "High-Efficiency All-Dielectric Metasurfaces for Ultracompact Beam Manipulation in Transmission Mode," Nano Lett. **15**, 6261–6266 (2015).

18. K. E. Chong, I. Staude, A. James, J. Dominguez, S. Liu, S. Campione, G. S. Subramania, T. S. Luk, M. Decker, D. N. Neshev, I. Brener, and Y. S. Kivshar, "Polarization-Independent Silicon Metadevices for Efficient Optical Wavefront Control," Nano Lett. **15**, 5369–5374 (2015).
19. G. Li, M. Kang, S. Chen, S. Zhang, E. Y.-B. Pun, K. W. Cheah, and J. Li, "Spin-Enabled Plasmonic Metasurfaces for Manipulating Orbital Angular Momentum of Light," Nano Lett. **13**, 4148–4151 (2013).
20. S. Vo, D. Fattal, W. V. Sorin, Z. Peng, T. Tran, M. Fiorentino, and R. G. Beausoleil, "Sub-Wavelength Grating Lenses With a Twist," IEEE Photonics Technology Letters **26**, 1375–1378 (2014).
21. Y. Yang, W. Wang, P. Moitra, I. I. Kravchenko, D. P. Briggs, and J. Valentine, "Dielectric Meta-Reflectarray for Broadband Linear Polarization Conversion and Optical Vortex Generation," Nano Lett. **14**, 1394–1399 (2014).
22. X. Ni, A. V. Kildishev, and V. M. Shalaev, "Metasurface holograms for visible light," Nature Communications; London **4**, 2807 (2013).
23. G. Zheng, H. Mühlenbernd, M. Kenney, G. Li, T. Zentgraf, and S. Zhang, "Metasurface holograms reaching 80% efficiency," Nat Nano **10**, 308–312 (2015).
24. A. Zhan, S. Colburn, C. M. Dodson, and A. Majumdar, "Metasurface Freeform Nanophotonics," Scientific Reports **7**, 1673 (2017).
25. S. Colburn, A. Zhan, and A. Majumdar, "Metasurface optics for full-color computational imaging," Science Advances **4**, eaar2114 (2018).
26. S. Colburn, A. Zhan, and A. Majumdar, "Varifocal zoom imaging with large area focal length adjustable metalenses," Optica, OPTICA **5**, 825–831 (2018).
27. E. R. Dowski and W. T. Cathey, "Extended depth of field through wave-front coding," Appl. Opt., AO **34**, 1859–1866 (1995).
28. W. T. Cathey and E. R. Dowski, "New paradigm for imaging systems," Appl. Opt., AO **41**, 6080–6092 (2002).
29. H. B. Wach, E. R. Dowski, and W. T. Cathey, "Control of chromatic focal shift through wave-front coding," Appl. Opt., AO **37**, 5359–5367 (1998).
30. "OSA | Depth from diffracted rotation," https://www.osapublishing.org/ol/abstract.cfm?uri=OL-31-2-181.
31. Y. Y. Schechner, R. Piestun, and J. Shamir, "Wave propagation with rotating intensity distributions," Phys. Rev. E **54**, R50–R53 (1996).
32. R. Piestun, Y. Y. Schechner, and J. Shamir, "Propagation-invariant wave fields with finite energy," J. Opt. Soc. Am. A, JOSAA **17**, 294–303 (2000).
33. S. Quirin and R. Piestun, "Depth estimation and image recovery using broadband, incoherent illumination with engineered point spread functions [Invited]," Appl. Opt., AO **52**, A367–A376 (2013).
34. X. Ni, S. Ishii, A. V. Kildishev, and V. M. Shalaev, "Ultra-thin, planar, Babinet-inverted plasmonic metalenses," Light: Science & Applications **2**, e72 (2013).
35. "Three-dimensional optical holography using a plasmonic metasurface | Nature Communications," https://www.nature.com/articles/ncomms3808.
36. "Generating optical orbital angular momentum at visible wavelengths using a plasmonic metasurface | Light: Science & Applications," https://www.nature.com/articles/lsa201448.

37. "Broadband High-Efficiency Half-Wave Plate: A Supercell-Based Plasmonic Metasurface Approach - ACS Nano (ACS Publications)," https://pubs.acs.org/doi/abs/10.1021/acsnano.5b00218.
38. "Broadband and Wide Field-of-view Plasmonic Metasurface-enabled Waveplates | Scientific Reports," https://www.nature.com/articles/srep07511.
39. Y. F. Yu, A. Y. Zhu, R. Paniagua-Domínguez, Y. H. Fu, B. Luk'yanchuk, and A. I. Kuznetsov, "High-transmission dielectric metasurface with 2π phase control at visible wavelengths," Laser & Photonics Reviews **9**, 412–418 (2015).
40. "Spectrally selective chiral silicon metasurfaces based on infrared Fano resonances | Nature Communications," https://www.nature.com/articles/ncomms4892.
41. P. Lalanne, S. Astilean, P. Chavel, E. Cambril, and H. Launois, "Blazed binary subwavelength gratings with efficiencies larger than those of conventional échelette gratings," Opt. Lett., OL **23**, 1081–1083 (1998).
42. S. Astilean, P. Lalanne, P. Chavel, E. Cambril, and H. Launois, "High-efficiency subwavelength diffractive element patterned in a high-refractive-index material for 633??nm," Opt. Lett., OL **23**, 552–554 (1998).
43. M. Khorasaninejad, W. T. Chen, R. C. Devlin, J. Oh, A. Y. Zhu, and F. Capasso, "Metalenses at visible wavelengths: Diffraction-limited focusing and subwavelength resolution imaging," Science **352**, 1190–1194 (2016).
44. M. Khorasaninejad, A. Y. Zhu, C. Roques-Carmes, W. T. Chen, J. Oh, I. Mishra, R. C. Devlin, and F. Capasso, "Polarization-Insensitive Metalenses at Visible Wavelengths," Nano Lett. **16**, 7229–7234 (2016).
45. M. Khorasaninejad, Z. Shi, A. Y. Zhu, W. T. Chen, V. Sanjeev, A. Zaidi, and F. Capasso, "Achromatic Metalens over 60 nm Bandwidth in the Visible and Metalens with Reverse Chromatic Dispersion," Nano Lett. **17**, 1819–1824 (2017).
46. W. T. Chen, A. Y. Zhu, V. Sanjeev, M. Khorasaninejad, Z. Shi, E. Lee, and F. Capasso, "A broadband achromatic metalens for focusing and imaging in the visible," Nature Nanotechnology 1 (2018).
47. S. Wang, P. C. Wu, V.-C. Su, Y.-C. Lai, M.-K. Chen, H. Y. Kuo, B. H. Chen, Y. H. Chen, T.-T. Huang, J.-H. Wang, R.-M. Lin, C.-H. Kuan, T. Li, Z. Wang, S. Zhu, and D. P. Tsai, "A broadband achromatic metalens in the visible," Nature Nanotechnology 1 (2018).
48. B. H. Chen, P. C. Wu, V.-C. Su, Y.-C. Lai, C. H. Chu, I. C. Lee, J.-W. Chen, Y. H. Chen, Y.-C. Lan, C.-H. Kuan, and D. P. Tsai, "GaN Metalens for Pixel-Level Full-Color Routing at Visible Light," Nano Lett. **17**, 6345–6352 (2017).
49. "Low-Contrast Dielectric Metasurface Optics - ACS Photonics (ACS Publications)," http://pubs.acs.org/doi/abs/10.1021/acsphotonics.5b00660.
50. Z.-B. Fan, Z.-K. Shao, M.-Y. Xie, X.-N. Pang, W.-S. Ruan, F.-L. Zhao, Y.-J. Chen, S.-Y. Yu, and J.-W. Dong, "Silicon Nitride Metalenses for Close-to-One Numerical Aperture and Wide-Angle Visible Imaging," Phys. Rev. Applied **10**, 014005 (2018).
51. J. Flannery, R. Al Maruf, T. Yoon, and M. Bajcsy, "Fabry-Pérot Cavity Formed with Dielectric Metasurfaces in a Hollow-Core Fiber," ACS Photonics **5**, 337–341 (2018).
52. S. Colburn, A. Zhan, E. Bayati, J. Whitehead, A. Ryou, L. Huang, and A. Majumdar, "Broadband transparent and CMOS-compatible flat optics with silicon nitride metasurfaces [Invited]," Opt. Mater. Express, OME **8**, 2330–2344 (2018).

53. S. M. Kamali, A. Arbabi, E. Arbabi, Y. Horie, and A. Faraon, "Decoupling optical function and geometrical form using conformal flexible dielectric metasurfaces," Nature Communications **7**, 11618 (2016).
54. "OSA | High-contrast gratings for integrated optoelectronics," https://www.osapublishing.org/aop/abstract.cfm?uri=aop-4-3-379.
55. J. Yang and J. A. Fan, "Analysis of material selection on dielectric metasurface performance," Opt. Express, OE **25**, 23899–23909 (2017).
56. V. Liu and S. Fan, "S4 : A free electromagnetic solver for layered periodic structures," Computer Physics Communications **183**, 2233–2244 (2012).
57. J. W. Goodman, *Introduction to Fourier Optics* (Roberts and Company Publishers, 2005).
58. K. Matsushima and T. Shimobaba, "Band-Limited Angular Spectrum Method for Numerical Simulation of Free-Space Propagation in Far and Near Fields," Opt. Express, OE **17**, 19662–19673 (2009).
59. D. Lin, M. Melli, E. Poliakov, P. S. Hilaire, S. Dhuey, C. Peroz, S. Cabrini, M. Brongersma, and M. Klug, "Optical metasurfaces for high angle steering at visible wavelengths," Scientific Reports **7**, 2286 (2017).
60. D. Fattal, Z. Peng, T. Tran, S. Vo, M. Fiorentino, J. Brug, and R. G. Beausoleil, "A multi-directional backlight for a wide-angle, glasses-free three-dimensional display," Nature **495**, 348–351 (2013).
61. P. Lalanne, S. Astilean, P. Chavel, E. Cambril, and H. Launois, "Design and fabrication of blazed binary diffractive elements with sampling periods smaller than the structural cutoff," J. Opt. Soc. Am. A, JOSAA **16**, 1143–1156 (1999).
62. Z.-B. Fan, Z.-K. Shao, M.-Y. Xie, X.-N. Pang, W.-S. Ruan, F.-L. Zhao, Y.-J. Chen, S.-Y. Yu, and J.-W. Dong, "Silicon nitride metalenses for unpolarized high-NA visible imaging," arXiv:1709.00573 [physics] (2017).
63. C. Hong, S. Colburn, and A. Majumdar, "Flat metaform near-eye visor," Appl. Opt., AO **56**, 8822–8827 (2017).
64. R. R. Reddy and Y. Nazeer Ahammed, "A study on the Moss relation," Infrared Physics & Technology **36**, 825–830 (1995).
65. Y.-W. Huang, H. W. H. Lee, R. Sokhoyan, R. A. Pala, K. Thyagarajan, S. Han, D. P. Tsai, and H. A. Atwater, "Gate-Tunable Conducting Oxide Metasurfaces," Nano Lett. **16**, 5319–5325 (2016).
66. J. K. S. Poon and W. D. Sacher, "Multilayer silicon nitride-on-silicon photonic platforms for three-dimensional integrated photonic devices and circuits," in *2017 75th Annual Device Research Conference (DRC)* (2017), pp. 1–2.
67. E. Bayati, A. Zhan, S. Colburn, and A. Majumdar, "The role of refractive index in metalens performance," arXiv:1805.04659 [physics] (2018).
68. Z. Bomzon, G. Biener, V. Kleiner, and E. Hasman, "Radially and azimuthally polarized beams generated by space-variant dielectric subwavelength gratings," Opt. Lett., OL **27**, 285–287 (2002).
69. A. Niv, G. Biener, V. Kleiner, and E. Hasman, "Propagation-invariant vectorial Bessel beams obtained by use of quantized Pancharatnam–Berry phase optical elements," Opt. Lett., OL **29**, 238–240 (2004).
70. "A Broadband, Background-Free Quarter-Wave Plate Based on Plasmonic Metasurfaces - Nano Letters (ACS Publications)," https://pubs.acs.org/doi/abs/10.1021/nl303445u.

71. A. Arbabi, Y. Horie, M. Bagheri, and A. Faraon, "Dielectric metasurfaces for complete control of phase and polarization with subwavelength spatial resolution and high transmission," Nat Nano **10**, 937–943 (2015).
72. Z. Lin, B. Groever, F. Capasso, A. W. Rodriguez, and M. Lončar, "Topology-Optimized Multilayered Metaoptics," Phys. Rev. Applied **9**, 044030 (2018).
73. A. Zhan, T. K. Fryett, S. Colburn, and A. Majumdar, "Inverse design of optical elements based on arrays of dielectric spheres," Appl. Opt., AO **57**, 1437–1446 (2018).
74. D. W. Mackowski and M. I. Mishchenko, "Calculation of the T matrix and the scattering matrix for ensembles of spheres," J. Opt. Soc. Am. A, JOSAA **13**, 2266–2278 (1996).
75. Y. Xu, "Electromagnetic scattering by an aggregate of spheres," Appl. Opt., AO **34**, 4573–4588 (1995).
76. A. Egel, L. Pattelli, G. Mazzamuto, D. S. Wiersma, and U. Lemmer, "CELES: CUDA-accelerated simulation of electromagnetic scattering by large ensembles of spheres," Journal of Quantitative Spectroscopy and Radiative Transfer **199**, 103–110 (2017).
77. E. Arbabi, A. Arbabi, S. M. Kamali, Y. Horie, and A. Faraon, "Multiwavelength polarization-insensitive lenses based on dielectric metasurfaces with meta-molecules," Optica, OPTICA **3**, 628–633 (2016).
78. "Multiwavelength achromatic metasurfaces by dispersive phase compensation | Science," http://science.sciencemag.org/content/347/6228/1342.
79. E. Arbabi, A. Arbabi, S. M. Kamali, Y. Horie, and A. Faraon, "Multiwavelength metasurfaces through spatial multiplexing," Scientific Reports **6**, srep32803 (2016).
80. O. Avayu, E. Almeida, Y. Prior, and T. Ellenbogen, "Composite functional metasurfaces for multispectral achromatic optics," Nature Communications **8**, ncomms14992 (2017).
81. B. Wang, F. Dong, Q.-T. Li, D. Yang, C. Sun, J. Chen, Z. Song, L. Xu, W. Chu, Y.-F. Xiao, Q. Gong, and Y. Li, "Visible-Frequency Dielectric Metasurfaces for Multiwavelength Achromatic and Highly Dispersive Holograms," Nano Lett. **16**, 5235–5240 (2016).
82. S. Wang, P. C. Wu, V.-C. Su, Y.-C. Lai, C. H. Chu, J.-W. Chen, S.-H. Lu, J. Chen, B. Xu, C.-H. Kuan, T. Li, S. Zhu, and D. P. Tsai, "Broadband achromatic optical metasurface devices," Nature Communications **8**, 187 (2017).
83. E. Arbabi, A. Arbabi, S. M. Kamali, Y. Horie, and A. Faraon, "Controlling the sign of chromatic dispersion in diffractive optics with dielectric metasurfaces," Optica, OPTICA **4**, 625–632 (2017).
84. S. Shrestha, A. C. Overvig, M. Lu, A. Stein, and N. Yu, "Broadband achromatic dielectric metalenses," Light: Science & Applications **7**, 85 (2018).
85. W. T. Chen, A. Y. Zhu, J. Sisler, Y.-W. Huang, K. M. A. Yousef, E. Lee, C.-W. Qiu, and F. Capasso, "Broadband Achromatic Metasurface-Refractive Optics," Nano Lett. **18**, 7801–7808 (2018).
86. A. Foi, "Practical denoising of clipped or overexposed noisy images," in *2008 16th European Signal Processing Conference* (2008), pp. 1–5.
87. M. Ohta, K. Sakita, T. Shimano, and A. Sakemoto, "Rotationally symmetric wavefront coding for extended depth of focus with annular phase mask," Jpn. J. Appl. Phys. **54**, 09ME03 (2015).
88. "Polarization-Independent Silicon Metadevices for Efficient Optical Wavefront Control - Nano Letters (ACS Publications)," https://pubs.acs.org/doi/abs/10.1021/acs.nanolett.5b01752.

89. P. Gutruf, C. Zou, W. Withayachumnankul, M. Bhaskaran, S. Sriram, and C. Fumeaux, "Mechanically Tunable Dielectric Resonator Metasurfaces at Visible Frequencies," ACS Nano **10**, 133–141 (2016).
90. H.-S. Ee and R. Agarwal, "Tunable Metasurface and Flat Optical Zoom Lens on a Stretchable Substrate," Nano Lett. **16**, 2818–2823 (2016).
91. S. M. Kamali, E. Arbabi, A. Arbabi, Y. Horie, and A. Faraon, "Highly tunable elastic dielectric metasurface lenses," Laser & Photonics Reviews **10**, 1002–1008 (2016).
92. A. She, S. Zhang, S. Shian, D. R. Clarke, and F. Capasso, "Adaptive metalenses with simultaneous electrical control of focal length, astigmatism, and shift," Science Advances **4**, eaap9957 (2018).
93. T. Roy, S. Zhang, I. W. Jung, M. Troccoli, F. Capasso, and D. Lopez, "Dynamic metasurface lens based on MEMS technology," APL Photonics **3**, 021302 (2018).
94. E. Arbabi, A. Arbabi, S. M. Kamali, Y. Horie, M. Faraji-Dana, and A. Faraon, "MEMS-tunable dielectric metasurface lens," Nature Communications **9**, 812 (2018).
95. I. Shimoyama, "Scaling in microrobots," in *Proceedings 1995 IEEE/RSJ International Conference on Intelligent Robots and Systems. Human Robot Interaction and Cooperative Robots* (1995), Vol. 2, pp. 208–211 vol.2.
96. R. S. Fearing, "Survey of sticking effects for micro parts handling," in *Proceedings 1995 IEEE/RSJ International Conference on Intelligent Robots and Systems. Human Robot Interaction and Cooperative Robots* (1995), Vol. 2, pp. 212–217 vol.2.
97. R. Legtenberg, A. W. Groeneveld, and M. Elwenspoek, "Comb-drive actuators for large displacements," J. Micromech. Microeng. **6**, 320 (1996).
98. "Two-element variable-power spherical lens," (December 3, 1964).
99. V. V. Athani, *Stepper Motors : Fundamentals, Applications And Design* (New Age International, 1997).
100. A. She, S. Zhang, S. Shian, D. R. Clarke, and F. Capasso, "Large area metalenses: design, characterization, and mass manufacturing," Opt. Express, OE **26**, 1573–1585 (2018).
101. S. S. Wang and R. Magnusson, "Theory and applications of guided-mode resonance filters," Appl. Opt., AO **32**, 2606–2613 (1993).
102. S. Fan and J. D. Joannopoulos, "Analysis of guided resonances in photonic crystal slabs," Phys. Rev. B **65**, 235112 (2002).
103. Z. Shi, M. Khorasaninejad, Y.-W. Huang, C. Roques-Carmes, A. Y. Zhu, W. T. Chen, V. Sanjeev, Z.-W. Ding, M. Tamagnone, K. Chaudhary, R. C. Devlin, C.-W. Qiu, and F. Capasso, "Single-Layer Metasurface with Controllable Multiwavelength Functions," Nano Lett. **18**, 2420–2427 (2018).
104. J. Schwiegerling and C. Paleta-Toxqui, "Minimal movement zoom lens," Appl. Opt., AO **48**, 1932–1935 (2009).
105. S. Colburn and A. Majumdar, "Simultaneous Achromatic and Varifocal Imaging with Quartic Metasurfaces in the Visible," ACS Photonics **7**, 120–127 (2020).
106. M. D. Aiello, A. S. Backer, A. J. Sapon, J. Smits, J. D. Perreault, P. Llull, and V. M. Acosta, "Achromatic varifocal metalens for the visible spectrum," (2019).
107. J. Ojeda-Castañeda, J. E. A. Landgrave, and C. M. Gómez-Sarabia, "Conjugate phase plate use in analysis of the frequency response of imaging systems designed for extended depth of field," Appl. Opt., AO **47**, E99–E105 (2008).
108. J. O. Castaneda, E. A. GOMEZ, H. P. Mora, M. T. CISNEROS, E. R. L. OROZCO, A. L. Martinez, J. S. P. SANTAMARIA, J. G. M. CASTRO, and R. C. S. SEGOVIANO,

"Optical system with variable field depth," United States patent US8159753B2 (April 17, 2012).
109. J. Ojeda-Castañeda and C. M. Gómez-Sarabia, "Tuning field depth at high resolution by pupil engineering," Adv. Opt. Photon., AOP **7**, 814–880 (2015).
110. G. Osnabrugge, R. Horstmeyer, I. N. Papadopoulos, B. Judkewitz, and I. M. Vellekoop, "Generalized optical memory effect," Optica, OPTICA **4**, 886–892 (2017).
111. D. Tang, S. K. Sahoo, V. Tran, and C. Dang, "Single-shot large field of view imaging with scattering media by spatial demultiplexing," Appl. Opt., AO **57**, 7533–7538 (2018).
112. P. Getreuer, "Total Variation Deconvolution using Split Bregman," Image Processing On Line **2**, 158–174 (2012).
113. S. Colburn and A. Majumdar, "Metasurface Generation of Paired Accelerating and Rotating Optical Beams for Passive Ranging and Scene Reconstruction," ACS Photonics (2020).
114. B. Cyganek and J. P. Siebert, *An Introduction to 3D Computer Vision Techniques and Algorithms* (John Wiley & Sons, 2011).
115. J. Geng, "Structured-light 3D surface imaging: a tutorial," Adv. Opt. Photon., AOP **3**, 128–160 (2011).
116. Y. Y. Schechner and N. Kiryati, "Depth from Defocus vs. Stereo: How Different Really Are They?," International Journal of Computer Vision **39**, 141–162 (2000).
117. S. Chaudhuri and A. N. Rajagopalan, *Depth From Defocus: A Real Aperture Imaging Approach* (Springer Science & Business Media, 2012).
118. Y. Xiong and S. A. Shafer, "Depth from focusing and defocusing," in *Proceedings of IEEE Conference on Computer Vision and Pattern Recognition* (1993), pp. 68–73.
119. T. Darrell and K. Wohn, "Pyramid based depth from focus," in *Proceedings CVPR '88: The Computer Society Conference on Computer Vision and Pattern Recognition* (1988), pp. 504–509.
120. Y. Shechtman, S. J. Sahl, A. S. Backer, and W. E. Moerner, "Optimal Point Spread Function Design for 3D Imaging," Phys. Rev. Lett. **113**, 133902 (2014).
121. A. Greengard, Y. Y. Schechner, and R. Piestun, "Depth from diffracted rotation," Opt. Lett., OL **31**, 181–183 (2006).
122. S. R. P. Pavani, M. A. Thompson, J. S. Biteen, S. J. Lord, N. Liu, R. J. Twieg, R. Piestun, and W. E. Moerner, "Three-dimensional, single-molecule fluorescence imaging beyond the diffraction limit by using a double-helix point spread function," PNAS **106**, 2995–2999 (2009).
123. S. R. P. Pavani and R. Piestun, "Three dimensional tracking of fluorescent microparticles using a photon-limited double-helix response system," Opt. Express, OE **16**, 22048–22057 (2008).
124. M. Badieirostami, M. D. Lew, M. A. Thompson, and W. E. Moerner, "Three-dimensional localization precision of the double-helix point spread function versus astigmatism and biplane," Appl. Phys. Lett. **97**, 161103 (2010).
125. M. A. Thompson, M. D. Lew, M. Badieirostami, and W. E. Moerner, "Localizing and Tracking Single Nanoscale Emitters in Three Dimensions with High Spatiotemporal Resolution Using a Double-Helix Point Spread Function," Nano Lett. **10**, 211–218 (2010).
126. "OSA | Single shot three-dimensional imaging using an engineered point spread function," https://www.osapublishing.org/oe/abstract.cfm?uri=oe-24-6-5946.
127. R. J. Lin, V.-C. Su, S. Wang, M. K. Chen, T. L. Chung, Y. H. Chen, H. Y. Kuo, J.-W. Chen, J. Chen, Y.-T. Huang, J.-H. Wang, C. H. Chu, P. C. Wu, T. Li, Z. Wang, S. Zhu, and

D. P. Tsai, "Achromatic metalens array for full-colour light-field imaging," Nature Nanotechnology **14**, 227 (2019).
128. Q. Guo, Z. Shi, Y.-W. Huang, E. Alexander, C.-W. Qiu, F. Capasso, and T. Zickler, "Compact single-shot metalens depth sensors inspired by eyes of jumping spiders," PNAS (2019).
129. C. Jin, J. Zhang, and C. Guo, "Metasurface integrated with double-helix point spread function and metalens for three-dimensional imaging," Nanophotonics **8**, 451–458 (2019).
130. C. Jin, M. Afsharnia, R. Berlich, S. Fasold, C. Zou, D. Arslan, I. Staude, T. Pertsch, and F. Setzpfandt, "Dielectric metasurfaces for distance measurements and three-dimensional imaging," AP **1**, 036001 (2019).
131. N. K. Efremidis, Z. Chen, M. Segev, and D. N. Christodoulides, "Airy beams and accelerating waves: an overview of recent advances," Optica, OPTICA **6**, 686–701 (2019).
132. S. R. P. Pavani and R. Piestun, "High-efficiency rotating point spread functions," Opt. Express, OE **16**, 3484–3489 (2008).
133. R. Piestun, B. Spektor, and J. Shamir, "Wave fields in three dimensions: analysis and synthesis," J. Opt. Soc. Am. A, JOSAA **13**, 1837–1848 (1996).
134. R. Piestun and J. Shamir, "Control of wave-front propagation with diffractive elements," Opt. Lett., OL **19**, 771–773 (1994).
135. W. T. Chen, A. Y. Zhu, J. Sisler, Z. Bharwani, and F. Capasso, "A broadband achromatic polarization-insensitive metalens consisting of anisotropic nanostructures," Nature Communications **10**, 355 (2019).
136. A. Arbabi, E. Arbabi, S. M. Kamali, Y. Horie, S. Han, and A. Faraon, "Miniature optical planar camera based on a wide-angle metasurface doublet corrected for monochromatic aberrations," Nature Communications **7**, ncomms13682 (2016).
137. L. Kipp, M. Skibowski, R. L. Johnson, R. Berndt, R. Adelung, S. Harm, and R. Seemann, "Sharper images by focusing soft X-rays with photon sieves," Nature **414**, 184–188 (2001).
138. M. Faraji-Dana, E. Arbabi, A. Arbabi, S. M. Kamali, H. Kwon, and A. Faraon, "Compact folded metasurface spectrometer," Nature Communications **9**, 4196 (2018).
139. E. J. Tremblay, R. A. Stack, R. L. Morrison, and J. E. Ford, "Ultrathin cameras using annular folded optics," Appl. Opt., AO **46**, 463–471 (2007).
140. E. J. Tremblay, J. Rutkowski, I. Tamayo, P. E. X. Silveira, R. A. Stack, R. L. Morrison, M. A. Neifeld, Y. Fainman, and J. E. Ford, "Relaxing the alignment and fabrication tolerances of thin annular folded imaging systems using wavefront coding," Appl. Opt., AO **46**, 6751–6758 (2007).
141. V. Sitzmann, S. Diamond, Y. Peng, X. Dun, S. Boyd, W. Heidrich, F. Heide, and G. Wetzstein, "End-to-end optimization of optics and image processing for achromatic extended depth of field and super-resolution imaging," ACM Trans. Graph. **37**, 114:1–114:13 (2018).